All-Semiconductor Photonic Crystal Surface Emitting Lasers at 980 nm through Epitaxial Regrowth

David Mervyl Williams

University of Sheffield

Department of Electronic and Electrical Engineering

Thesis submitted to the University of Sheffield for the degree of Doctor of Philosophy

March 17, 2014

Abstract

The purpose of this thesis is to outline the novel method of epitaxial regrowth for fabrication of photonic crystal surface emitting lasers (PCSELs). Waveguide modelling is conducted to demonstrate that strong coupling to the photonic crystal occurs, and that a decent mode overlap with the active region is simultaneously achieved in an optimised structure. Details of the regrowth process and the various fabrication techniques involved are discussed. Characterisation of devices indicates that emission from these all-semiconductor structures is comparable to void based PCSELs in terms of: wavelength dependence on period, coupling constants as measured from band structures, far-field profiles and beam divergences. The detuning of emission wavelength as a function of temperature is examined, as well as the temperature dependence of threshold currents, and the effects of external feedback from an output coupler.

Acknowledgments

I would like to thank all my family, friends and colleagues who supported me throughout this endeavour. Each of them has been invaluable in their own way during the course of my PhD and many of them have helped make it an enjoyable and memorable experience.

Special thanks goes to those of the PCSEL group; Luke Shepherd, Richard Taylor, Ben Stevens, David Childs, Kris Groom and Richard Hogg, for their help and support on a regular basis.

I would also like to thank my colleagues from around the globe, both at NIMS in Japan, and CEIT in Spain, who have helped overcome various technical difficulties and given me a fabulous opportunity to use their facilities. Thanks especially to Txaber for introducing me to pintxos in San Sebastian, and for putting up with my poor attempts at speaking Spanish!

In particular, I would like to acknowledge the enormous effort my supervisor Professor Richard Hogg has put into helping me achieve both my publications and this thesis. Without his support and guidance I would not have achieved so much.

And finally, I gratefully acknowledge the funding received from the EPSRC and the Royal Society, without which this work wouldn't have been possible.

Author's publication list

1. "Epitaxially regrown GaAs based photonic crystal surface emitting laser" D. M. Williams, K. M. Groom, B. J. Stevens, D. T. D. Childs, R. J. E. Taylor, S. Khamas, R. A. Hogg, N. Ikeda and Y. Sugimoto. Photon. Tech. Lett., **24**, No. 11, 966 (2012)

2. "Optimisation of coupling between photonic crystal and active elements in an epitaxially regrown GaAs based photonic crystal surface emitting laser" D. M. Williams, K. M. Groom, B. J. Stevens, D. T. D. Childs, R. J. E. Taylor, S. Khamas, R. A. Hogg, N. Ikeda, and Y. Sugimoto. Jap. J. Appl. Phys., **51**, 02BG05 (2012)

3. "All-semiconductor photonic crystal surface emitting lasers based on epitaxial regrowth" R. J. E. Taylor, D. M. Williams, D. T. D. Childs, B. J. Stevens, L. R. Shepherd, S. Khamas, K. M. Groom, R. A. Hogg, N. Ikeda and Y. Sugimoto. IEEE J. Sel. Topics Quant. Electron., **19**, No. 4, (2013)

4. "Band structure and waveguide modelling of epitaxially regrown photonic crystal surface emitting lasers" R. J. E. Taylor, D. M. Williams, J. R. Orchard, D. T. D. Childs, S. Khamas and R. A. Hogg. J. Phys. D: Appl. Phys., **46**, 264005 (2013)

5. "Design rules and characterisation of electrically pumped vertical external cavity surface emitting lasers" J. R. Orchard, D. T. D. Childs, L. C. Lin, B. J. Stevens, D. M. Williams, R. A. Hogg. Jap. J. Appl. Phys., **50**, 04DG0S (2011)

6. "Trade-offs in the realisation of electrically pumped vertical external cavity surface emitting lasers" J. R. Orchard, D. T. D. Childs, L. C. Lin, B. J. Stevens, D. M. Williams, R. A. Hogg. J. Sel. Top. Quant. Electron., **17**, No. 6, 1745 (2011)

Conference presentations

1. "Gain characterisation of edge and surface emission from electrically pumped vertical external cavity surface emitting laser structure" D. M. Williams, J. R. Orchard, D. T. D. Childs, B. J. Stevens, L. C. Lin and R. A. Hogg. Contributed oral presentation, UK Semiconductors 2011 (Sheffield)

2. "Epitaxially regrown GaAs based photonic crystal surface emitting laser" D. M. Williams, K. M. Groom, B. J. Stevens, Q. Jiang, D. T. D. Childs, R. J. E. Taylor, S. Khamas, R. A. Hogg, N. Ikeda and Y. Sugimoto. Contributed poster presentation, UK Semiconductors 2011 (Sheffield)

3. "An epitaxially regrown GaAs based photonic crystal surface emitting laser" D. M. Williams, K. M. Groom, B. J. Stevens, D. T. D. Childs, R. J. E. Taylor, S. Khamas, R. A. Hogg, N. Ikeda and Y. Sugimoto. Contributed oral presentation, Solid State Devices and Materials 2011 (Tokyo).

4. "Realization of a photonic crystal surface emitting laser through GaAs based regrowth" D. M. Williams, K. M. Groom, D. T. D. Childs, B. J. Stevens, S. Khamas, T. S. Roberts, R. J. E. Taylor, N. Ikeda, Y. Sugimoto and R.A. Hogg. Contributed oral presentation, Photonics West 2012 (San Francisco).

Contents

1 Introduction **5**

1.1 Historical perspective 5

1.2 Relevant photonic crystal theory 9

1.2.1 Key definitions 10

1.2.2 Two-dimensional feedback and coupling coefficients . . 15

1.2.3 Photonic band structure and band gaps 18

1.2.4 Leaky and non-leaky modes 23

1.3 Summary of previous work 25

1.3.1 Band structures and modelling methods 25

1.3.2 Atom shapes and lattice designs 29

1.3.3 Defect cavity lasers 33

1.3.4 PCSEL structures and fabrication methods 35

1.3.5 PCSEL characterisation 37

1.4 Gaps in the knowledge 42

1.4.1 All-semiconductor photonic crystals 42

1.4.2 Regrown GaAs PCSELs 43

1.4.3 Low temperature characterisation 43

1.5 Thesis outline 44

2 Waveguide Modelling **56**

2.1 Introduction 56

2.2 Background 57

2.3 Theory 58

2.4 Waveguide structure 64

2.5 Structural optimisation - all-semiconductor photonic crystal . 67

2.6 Introduction of a photonic crystal with voids 78

2.7 Conclusions 83

3 Fabrication and Processing **89**

3.1 Introduction 89

3.2 Background 90

3.3 Successful regrowth process 96

3.3.1 Initial growth 97

3.3.2 Photonic crystal definition 98

3.3.3 Regrowth step 100

3.3.4 Device processing 101

3.4 Design discussions and modifications 103

3.4.1 Regrowth development 104

3.4.2 Patterning alternatives 106

3.4.3 Etch optimisation 112

3.5 Conclusions 114

3.6 Future work 115

4 Low Temperature Characterisation 123

4.1 Introduction 123

4.2 Background 123

4.3 Basic characteristics 128

4.3.1 VI, LI curves and EL spectra 128

4.3.2 Lasing peak shift and linewidths 135

4.3.3 Detuning as a function of temperature 138

4.4 Low temperature far-field patterns and divergences 141

4.5 Threshold current temperature dependence 149

4.6 Conclusions 152

5 Room Temperature Characterisation 160

5.1 Introduction 160

5.2 Background 160

5.3 Basic characteristics 162

5.3.1 Spectra and LI 162

5.3.2 Polarisation 167

5.3.3 Far-field pattern 170

5.4 Band structure characterisation 174

5.5 External feedback characterisation 181

5.6 Conclusions and future work 190

6 Summary and Future Work **197**

6.1 Alternative materials in the photonic crystal 198

6.2 Device improvement 200

6.3 Additional characterisation possibilities 202

1 Introduction

1.1 Historical perspective

The ability to modify and inhibit spontaneous emission from atoms has long been known to be possible using fluctuations of the refractive index in the material through which the light propagates [1,2]. Early work on photonic crystals considered the inhibition of photons from occupying certain electromagnetic modes within a three dimensional structure [1], and predicting the behaviour of localised photons [2]. Both these and other early photonic crystal studies built on the success and knowledge of distributed feedback lasers (DFBs), which rely on back-scattered light from one-dimensional periodic variations in material composition, and hence refractive index, being coherent with the initial emission [3]. DFBs use the periodicity of these fluctuations to produce a single dominant mode within a classical Fabry-Perot cavity [3–5], and laser emission typically occcurs from the edge of the device (figure 1.1).

As applications such as data storage, broadband communication links, and biomedical imaging developed, demand for semiconductor lasers increased. Also, the need for an efficient surface-emitting laser became evident. The first vertical cavity surface emitting laser (VCSEL) was proposed in 1977, and these devices now typically use highly reflective distributed Bragg reflectors

(DBRs) to create a cavity with gain occuring in the vertical direction [6, 7]. Development of low threshold devices operating under continuous wave (CW) conditions at 77K, and under pulsed conditions at room temperature [8], soon followed in 1987. This resulted in a huge surge of research into improvements of device characteristics.

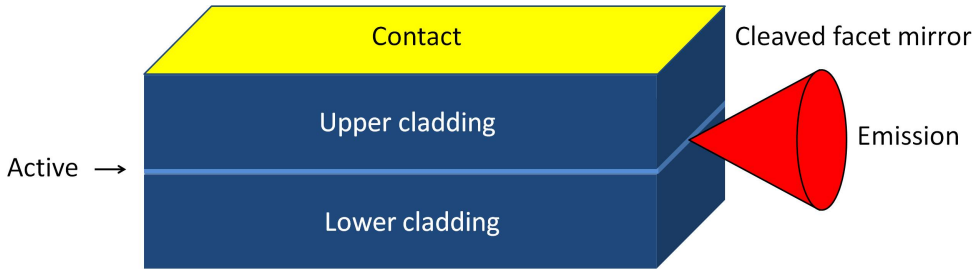

Figure 1.1: Schematic of a simple ridge laser showing emission from the edge.

Whilst the work of Yablonovitch and John discussed the manipulation of light in 1987, they also highlighted that the real problem was fabricating a structure to give this control. Any such structure had to have periodic fluctuations on the scale of the desired wavelength in the material. Theoretical studies showed that a three-dimensional, face-centred cubic crystal structure had potential to exhibit a strong influence on the properties of electromagnetic radiation in the material [9]. This structure was created by drilling into metal at specific angles (figure 1.2), showing the first clear evidence for photonic crystals inhibiting electromagnetic propagation, in this case for microwave

wavelengths [10]. The challenge became to reduce the structure size using nanotechnology to target infra-red and optical wavelengths.

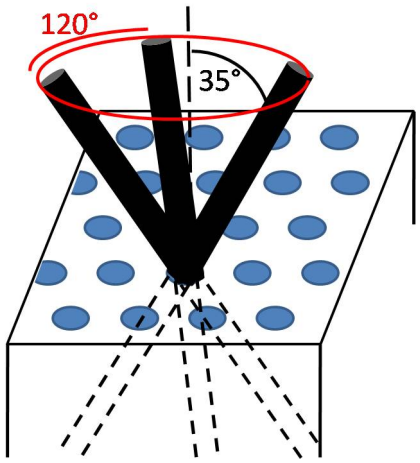

Figure 1.2: Schematic of how Yablonovitch *et al.* created a three dimensional face-centred cubic structure by drilling each hole three times from 120° apart on the azimuth and at 35° to the normal.

Over the next few years, little progress was evident on developing three-dimensional structures due to the complexity of fabrication. However, predictions that two dimensional (2D) photonic crystals could partially control the electromagnetic propagation through the structure, especially if a defect was introduced, were realised [11–13]. These defects created micro-cavities within the photonic crystal on the order of the wavelength. Surrounding the cavity, the rest of the photonic crystal acted as highly reflective mirrors and laser oscillation was achieved. Defect based structures such as linear waveguides [14, 15] or guiding light around sharp corners [16] suddenly became of

interest within the photonic crystal field as they increased the possibility of realising photonic integrated circuits.

In 1998-1999, early two-dimensional photonic crystal surface emitting lasers (PCSELs), fabricated from organic polymers, revealed that light propagating through these structures experienced strong manipulation by the photonic crystal and that this caused lasing to occur in the vertical direction [17, 18]. These structures did not rely on a defect micro-cavity and caused a resurgence in research on 2D photonic crystal design and PCSEL fabrication. The first electrically pumped PCSEL was demonstrated in 1999 [19], and room temperature CW operation reported by 2004 [20].

In the first few years of the new millenium, research was conducted into precisely how laser emission was influenced by the photonic crystal. Lasing was shown to occur at photonic band edges, giving PCSELs potential to achieve output powers that scale with device area [21]. Large scale devices ($\geq 500\ \mu$m) were also shown to be coherent [22], giving PCSELs potential in high power, large area, single-mode, coherent applications. Of particular note, the far-field patterns of PCSELs were shown to have extremely low beam divergence angles ($\leq 1^{\circ}$) and that beam shape could be influenced by photonic crystal design [23]. These unique properties give PCSELs significant possible advantages over other surface emitting lasers such as VCSELs.

1.2 Relevant photonic crystal theory

Photonic crystal surface emitting lasers utilise a two-dimensional photonic crystal as an epitaxial layer within a semiconductor structure to achieve lasing out of the plane of the device. The photonic crystal layer in a PCSEL creates two significant properties; firstly, the photonic crystal creates a feedback effect at a single wavelength, thus enforcing single mode laser oscillation. Secondly, when this wavelength satisfies the Bragg condition there is diffraction in the vertical direction, resulting in out-of-plane lasing. For light incident on a grating, scattering occurs such as in figure 1.3.

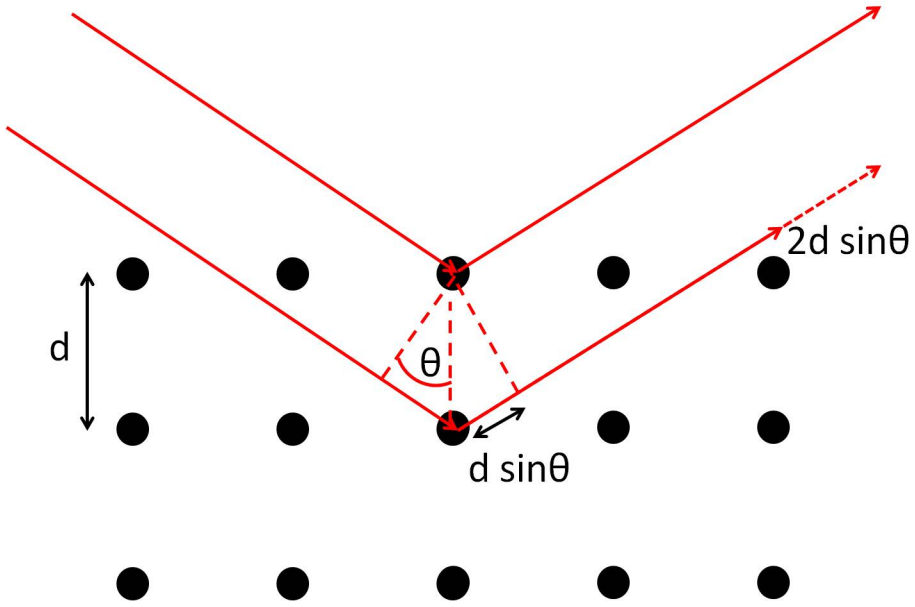

Figure 1.3: Diffraction of two plane waves (red lines) by a two-dimensional grating (black dots).

The resulting diffraction pattern is created from the constructive interference of the scattered waves that satisfy the Bragg condition (1.2.1).

$$m\lambda = 2dsin\theta \tag{1.2.1}$$

where m is an integer value.

Key definitions and the fundamental theory behind photonic crystals required to understand and characterise device performance are outlined in sections 1.2.1-1.2.4.

1.2.1 Key definitions

A photonic crystal is a structure where the refractive index is varied in a periodic fashion by interchanging the constituent materials. This periodic variation can occur in one, two or three dimensions and results in different effects in each case. Figure 1.4 shows what a photonic crystal looks like in one, two or three dimensions. A one-dimensional periodic crystal (figure 1.4a)) is used in distributed feedback (DFB) lasers [3–5], whilst this thesis looks at using a two-dimensional photonic crystal (figure 1.4b)) to form a surface emitting laser, similar to [19, 20, 22]. Three-dimensional photonic crystals (figure 1.4c)) have additional characteristics that can be exploited but currently present a challenge in terms of ease and reliability of fabrication [10, 24, 25].

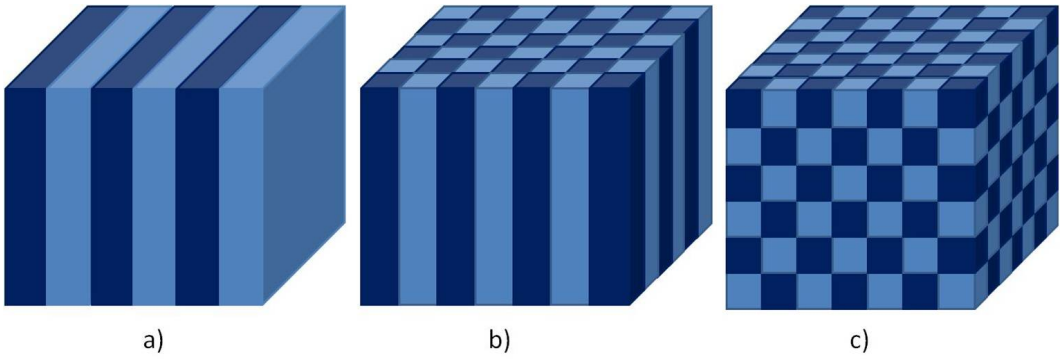

Figure 1.4: Photonic crystals with periodic changes in a) one-dimension, b) two-dimensions, c) three-dimensions. *Adapted from* [26].

The design of the two-dimensional photonic crystal is key in determining how light propagates through a structure such as a PCSEL. Important factors to consider in photonic crystal design include: lattice structure, lattice period, unit cell or 'atom' shape, fill factor and refractive indices of constituent materials. Each of these is defined below, before explaining how they are all relevant to PCSEL design.

The lattice of a photonic crystal refers to the layout of the periodic structure, with the name typically describing the appearance when the photonic crystal plane is viewed from above. Previously, photonic crystals have commonly been formed in square lattices [20] and triangular lattices [11], whilst honeycomb [27] and Kagome lattices [28] (figure 1.5) have also been proposed.

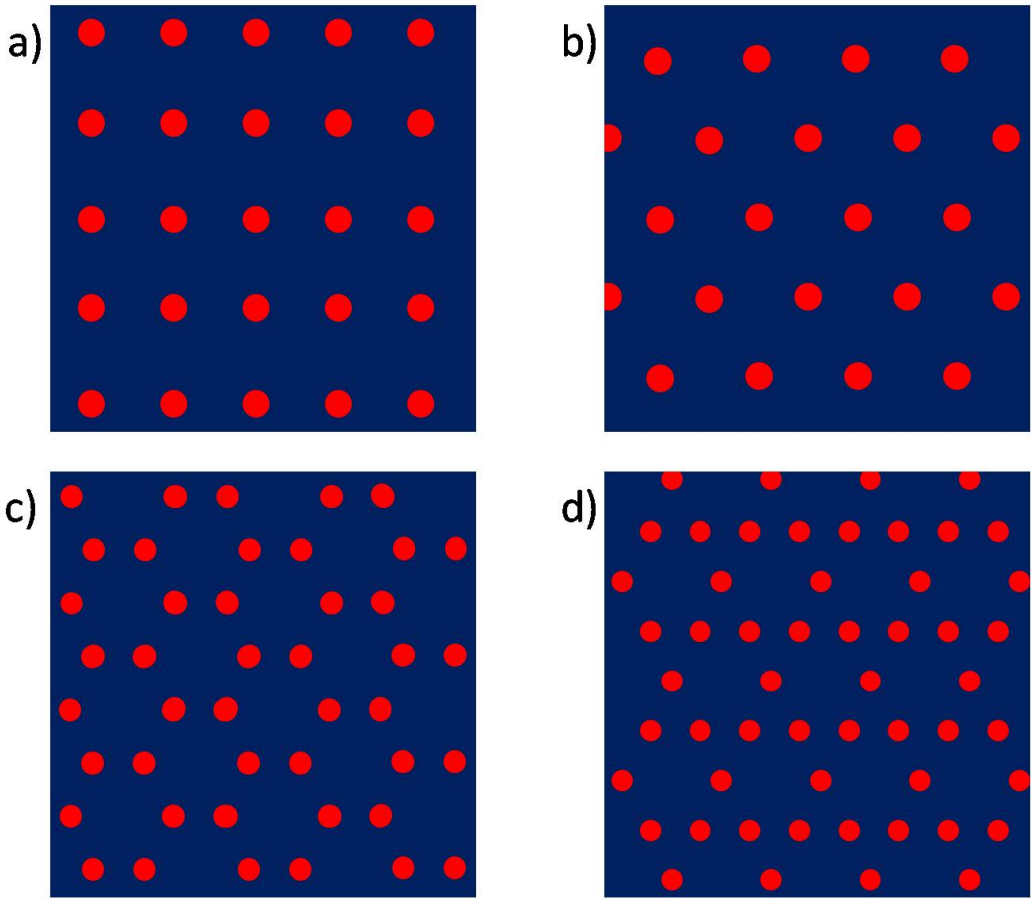

Figure 1.5: Example lattice structures for a: a) Square lattice b) Triangular lattice c) Honeycomb lattice d) Kagome lattice.

The period, a, is measured as the distance between two points in the structure after which the pattern repeats itself. Figure 1.6 indicates how the period of a photonic crystal is measured in a two-dimensional square lattice photonic crystal. The unit cell (smallest repeatable unit) can be used to define the entire photonic crystal in conjunction with the number of repeats.

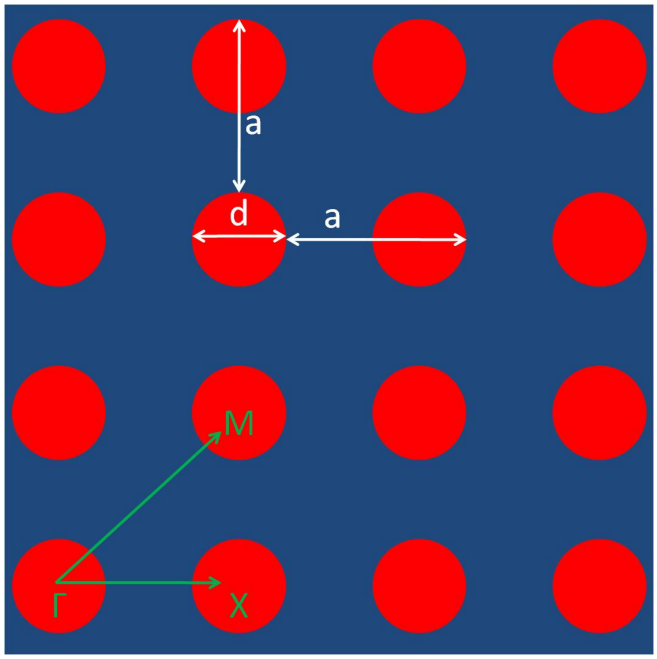

Figure 1.6: Square lattice photonic crystal with period a, and circular atom shape of diameter d. Crystallographic directions Γ-X and Γ-M shown in green.

Within the unit cell the different materials form distinct shapes and from this the 'atom' shape of the photonic crystal can be defined. For example, in figure 1.5 each of the different lattices has the same circular atom shape (in red). The first PCSELs focused on using circular atoms, such as in figures 1.5 and 1.6, as these are generated easily using electron beam lithography [19]. However, various other atom shapes such as triangular [29] or chevron have been investigated in search of an optimal design [30] and these are discussed in section 1.3.2.

The ratio of one material to the other in the photonic crystal is defined as

the fill factor. The fill factor can be expressed as a ratio of the materials along a one-dimensional cross-section through the centre of the atom shape (1.2.2), or as a ratio by area within the unit cell. In both case the fill factor is usually expressed as a fraction of the period. From the definitions in figure 1.6 the fill factor (ff) for a square lattice with a circular atom shape can be expressed as:

$$ff = \frac{d}{a} \tag{1.2.2}$$

if considering a cross-section taken through the centre of the circular atom, or:

$$ff = \frac{\pi(\frac{d}{2})^2}{a^2} \tag{1.2.3}$$

if considering the ratio of area occupied by each material in the unit cell.

The definition of the fill factor is clearly dependent on the choice of lattice and atom shape in the photonic crystal design. In this thesis the fill factor definition in 1.2.2 is used as a simple square lattice and circular hole is used.

In a PCSEL the photonic crystal is made from two materials and in most of the previous work (see section 1.3.3) this has consisted of semiconductor and voids. These voids are assumed to have a refractive index of 1 (air). However, in an all-semiconductor PCSEL the additional semiconductor material adds a

degree of freedom to the device design. Photonic crystals with atom shapes of lower refractive index than the surroundings are defined as type I (figure 1.7a)), and photonic crystals with atom shapes of higher refractive index than the surroundings are defined as type II (figure 1.7b)).

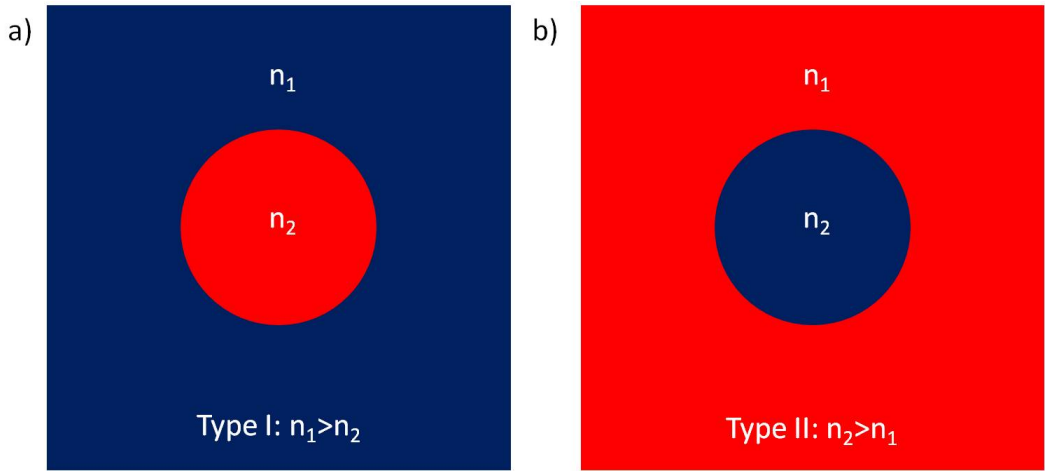

Figure 1.7: Unit cell of a square lattice with circular atom shape for: a) type I photonic crystal ($n_1 > n_2$) b) type II photonic crystal ($n_2 > n_1$).

1.2.2 Two-dimensional feedback and coupling coefficients

The parameters outlined above are key to photonic crystal design as each influences the propagation of light throughout the structure. Although the crystal symmetries result in identical propagation characteristics in a few specific directions, it is the lattice shape that governs these symmetric directions. Feedback is achieved when the period matches the wavelength of light within the material, and in the directions where this criteria is met standing waves

form. Various lattice designs will therefore allow different propagation and feedback characteristics. The lattice period and fill factor affect the wavelength of light that achieves feedback within the crystal, whilst atom shape and material refractive indices influence characteristics such as far-field profile and coupling strength.

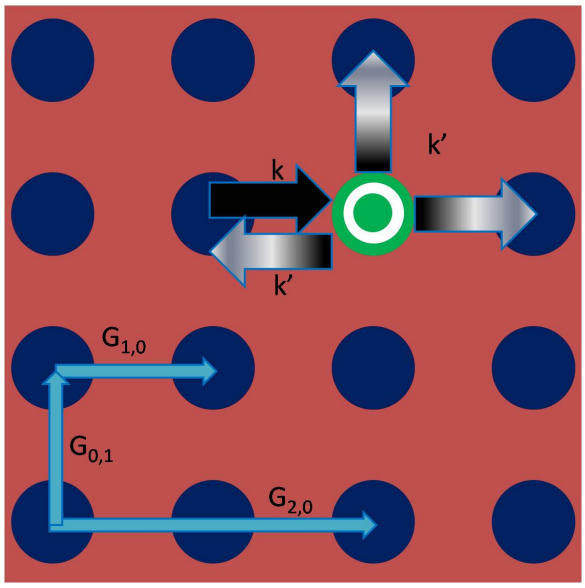

Figure 1.8: Reciprocal square lattice with reciprocal vectors $G_{0,1}$, $G_{1,0}$ and $G_{2,0}$ indicated by blue arrows. Incident wave (black arrow), scattered in-plane waves (grey arrows) and diffracted out-of-plane waves (green and white circles) indicate light propagation through the crystal.

The coupling strength of a photonic crystal such as in figure 1.6, is quantified by optical coupling coefficients κ_1, κ_2, and κ_3 using two-dimensional coupled wave theory [31]. This considers the coupling of an initial wave (wavevector k) travelling from one atom shape to the nearest neighbours that surround

it. As a first approximation the four closest atom shapes were used to define the coupling coefficients [32], however, this was found to be inadequate when comparing theoretical and experimental coupling values. Analysis of the interaction with the nearest eight neighbours in a square lattice gives a more accurate description of the feedback within the photonic crystal. The theoretical coupling coefficients, κ_1, κ_2, and κ_3, are calculated using 1.2.4 for the relevant reciprocal lattice vectors (see 1.2.5-1.2.7) [31].

$$\kappa(G) = \frac{\pi\Delta\epsilon}{an_{eff}^2} f \frac{2J_1(|G|2\sqrt{\pi f})}{|G|2\sqrt{\pi f}} \tag{1.2.4}$$

where $\Delta\epsilon$ is the dielectric constant difference, a is the period, n_{eff} is the effective refractive index, f is the fill factor and $J_1(x)$ is the Bessel function of the first order ($x = |G|2\sqrt{\pi f}$ in 1.2.4). Using the reciprocal lattice vector, $\beta_0 = \frac{2\pi}{a}$, gives:

$$\kappa_1 = \kappa(G)|_{|G|=\beta_0} \tag{1.2.5}$$

$$\kappa_2 = \kappa(G)|_{|G|=\sqrt{2}\beta_0} \tag{1.2.6}$$

$$\kappa_3 = \kappa(G)|_{|G|=2\beta_0} \tag{1.2.7}$$

Figure 1.8 plots the reciprocal space for a square lattice and indicates the reciprocal lattice vectors $G_{0,1}$, $G_{1,0}$ and $G_{2,0}$. The initial wave (black arrows) can be scattered into other directions with wavevector k'. In-plane feedback occurs (grey arrows) when the wavelength is equal to the period, thereby satisfying the Bragg condition (see section 1.2.1). Out-of-plane scattering (green circles) is possible by second order Bragg diffraction from the grating. Out-of-plane scattering is linked to κ_1 and in-plane feedback is determined by the value of κ_3. κ_2 describes the coupling of orthogonal waves within the crystal and these have an overlap integral of zero so disappear in 2-d coupled wave analysis [31].

1.2.3 Photonic band structure and band gaps

Typically the photonic band structure is calculated from the lattice shape, atom shape and refractive indices of the unit cell using either the plane wave expansion method (PWEM) [33] or the finite difference time domain (FDTD) method [34]. Both of these methods use Maxwell's electromagnetic equations (1.2.8-1.2.11) to model the propagation of light in the photonic crystal in small iterative steps. The solutions are used to plot the allowed frequencies of photonic states as a function of wavevector, creating a photonic band structure (figure 1.9a)). The dispersion relation of photons in the band structure is

determined by the shape and composition of the photonic crystal. To aid in understanding this, the analogy can be made to the electronic band structure and the effect of a crystal lattice on the electrons.

Equations 1.2.8-1.2.11 list the macroscopic versions of Maxwell's equations having used the following assumptions:

- Propagation occurs within a mixed dielectric medium as a function of position r.
- There is no variation in the structure over time.
- There are no free charges or currents within the structure.
- Any frequency dependence of the dielectric constant is ignored, and the relative permittivity (ϵ(r)) is assumed to be real and positive (i.e. for transparent materials).

$$\nabla \cdot \mathbf{H}(\mathbf{r}, t) = 0 \tag{1.2.8}$$

$$\nabla \cdot [\epsilon(\mathbf{r})\mathbf{E}(\mathbf{r}, t)] = 0 \tag{1.2.9}$$

$$\nabla \times \mathbf{E}(\mathbf{r}, t) + \mu_0 \frac{\partial \mathbf{H}(\mathbf{r}, t)}{\partial t} = 0 \tag{1.2.10}$$

$$\nabla \times \mathbf{H}(\mathbf{r},t) - \epsilon_0 \epsilon(\mathbf{r}) \frac{\partial \mathbf{E}(\mathbf{r},t)}{\partial t} = 0 \tag{1.2.11}$$

where $\mathbf{H}(\mathbf{r},t)$ is the magnetic field, $\mathbf{E}(\mathbf{r},t)$ is the electric field, μ_0 is the permeability of free space and ϵ_0 is the permittivity of free space.

Electromagnetic modes propagating through a given medium can be found by combining 1.2.10 and 1.2.11 to remove one of the variables. For example, by taking 1.2.11, dividing by $\epsilon(\mathbf{r})$, and then taking the curl, an equation dependent only on the H-field is produced (1.2.12). From the solutions of the H-field, the E-field solutions can be recovered by substituting back into 1.2.10.

$$\nabla \times \left(\frac{1}{\epsilon(\mathbf{r})} \nabla \times \mathbf{H}(\mathbf{r}) \right) = \left(\frac{\omega}{c} \right)^2 \mathbf{H}(\mathbf{r}) \tag{1.2.12}$$

The photonic band structure can be calculated for both transverse electric (TE) and transverse magnetic (TM) modes, however, typically TE modes are considered for PCSELs. Due to the high degree of symmetry in photonic crystals the TE and TM band structures are often very similar on a large scale. However, closer examination of the band structure can reveal differences such as a partial band gap between TE bands 3 and 4 at the gamma point for the square lattice modelled in figure 1.9b). Band gaps indicate there are certain frequencies at which light will not propagate through the photonic crystal.

The band edges near the band gap are of particular interest as these regions of the band structure have zero gradient, which corresponds to zero dispersion. Hence, photons in these states will have zero group velocity. When the group velocity is zero the photons form standing waves within the crystal and enhance feedback effects. Figure 1.9b) shows that there are four bands of interest close to the band gap, two of which have local maxima or minima and two of which have relatively flat bands extending in the Γ-X direction.

Band structures are plotted with frequencies in units of c/a to be scale invariant, allowing experimental frequencies/wavelengths to be targeted by varying the period of the photonic crystal lattice. For emission at 980 nm from the lattice modelled in figure 1.9, a period of approximately 300 nm is required (calculated from 1.2.14). Depending on which band edge lasing occurs from, either band 2, 3, 4 or 5 - those close to the gap at the Γ point in figure 1.9b), the frequency value in 1.2.13 needs to be adjusted accordingly.

For the partial band gap at f = 0.3(c/a) in figure 1.9:

$$f = \frac{c}{\lambda_0} = 0.3\frac{c}{a} \tag{1.2.13}$$

Rearranging for a in terms of λ_0 gives:

$$a = 0.3\lambda_0 \tag{1.2.14}$$

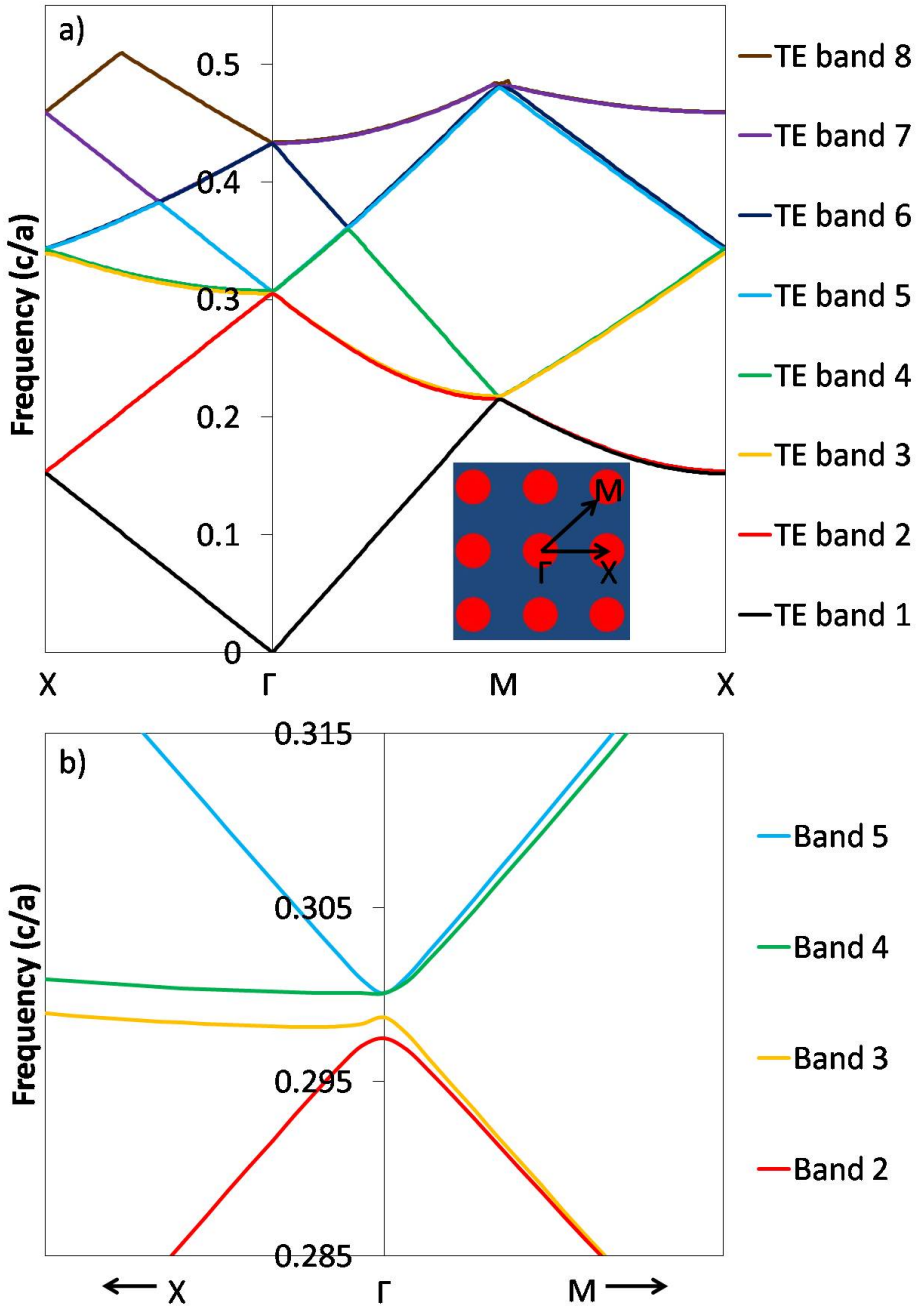

Figure 1.9: a) Modelled photonic bandstructure for the first 8 TE bands in a square lattice using PWEM. *Inset:* Square lattice indicating Γ, X, and M points. b) Partial photonic band gap for frequencies close to 0.3(c/a) at the Γ point.

1.2.4 Leaky and non-leaky modes

Two types of mode at the band edge are possible in a photonic crystal, described as either leaky or non-leaky. The symmetry of the in-plane electric field with respect to the unit cell centre determines whether the mode at each photonic band edge is leaky or not. Non-leaky modes occur when the electric fields are asymmetric with respect to the unit cell centre, with the phase of the diffracted light such that destructive interference occurs and no light is emitted in the vertical direction. If the in-plane electric field distribution is symmetric this destructive interference does not occur and the mode is considered leaky. A certain amount of leakage can be introduced to non-leaky modes by altering the vertical optical confinement through changes to the atom shape [30].

Band structure modelling using the PWEM or FDTD method also yields information on the magnetic field vectors throughout the photonic crystal. Figure 1.10 plots the magnetic field vectors (high intensity in red, low intensity in blue) over the lattice structure (black circles) for the bands close to the partial band gap in figure 1.9b). In figures 1.10a) and 1.10b) these are symmetric about either the x or y axes and so the lower frequency non-degenerate bands are leaky. Whilst the higher frequency degenerate bands (figures 1.10c) and 1.10d)) demonstrate the asymmetry typical for non-leaky modes.

The magnetic field vectors in figure 1.10 also enable prediction of the emission polarisation from each of the bands. From figure 1.10a) and 1.10b), emission from TE bands 2 and 3 will have a linear polarisation along either the x, or y, axis of the photonic crystal. The modelling predicts, however, that for TE bands 4 and 5 the polarisation will be more complex (figure 1.10c) and 1.10d)), as there is a two dimensional variation in regions of high and low magnetic field vectors.

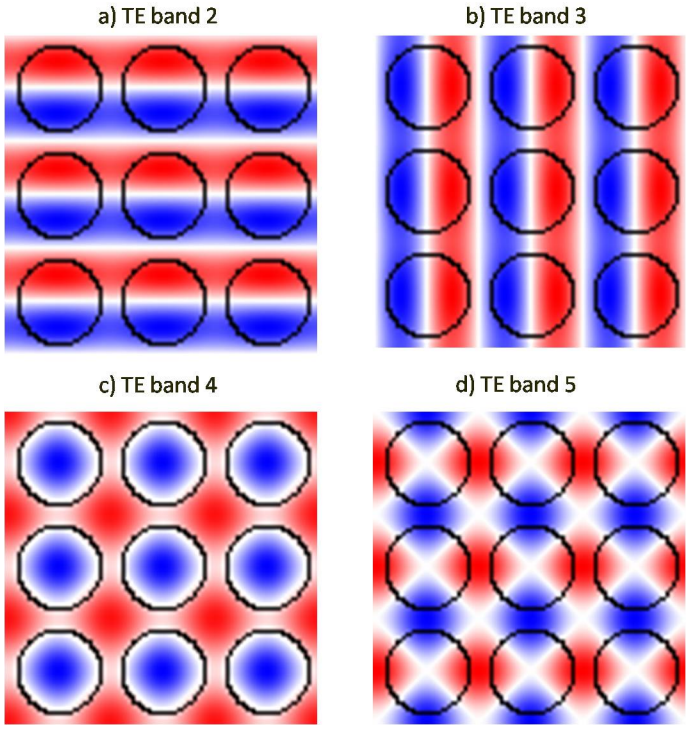

Figure 1.10: Variations in the magnetic field vectors for the square lattice photonic crystal modelled above for: a) TE band 2, b) TE band 3, c) TE band 4 and d) TE band 5. Regions of high intensity shown in red, low intensity in blue and zero intensity in white. Black circles indicate atom shape location. *Courtesy of R. J. E. Taylor of the University of Sheffield.*

1.3 Summary of previous work

This section reviews the current state of design, fabrication and characteristics of photonic crystal based devices reported in the literature. Firstly, band structure modelling methods are discussed; then the effects of atom and lattice shapes on emission; followed by a quick introduction to what a defect cavity laser is; the reported fabrication methods and PCSEL structures are reviewed; and finally a summary of device characteristics is included.

1.3.1 Band structures and modelling methods

There is a significant amount of work on photonic band structures and the various modelling methods reported in the literature [33–37]. Band structures are of great use in creating photonic crystal based devices as they are scale invariant, and thus only the period of the crystal has to be changed to alter the desired emission wavelength. Here the two most commonly used two-dimensional models in the literature are briefly outlined: the finite difference time domain (FDTD) method, and the plane wave expansion method (PWEM).

According to [35] the FDTD method essentially calculates solutions to the Maxwell curl equations (1.2.10,1.2.11) that are accurate to a second order approximation. The solutions are calculated for sample space intervals which

are small compared with the wavelengths considered. These samples are taken at all space points in small successive increments of time. The method gets its name from the small or 'finite' difference in both time and space used to calculate the derivatives. Sources can be generated within the modelled space by defining specific values for the electric and magnetic fields at specific points in time and space. For modelling two-dimesional (2D) photonic crystals the material is assumed to be constant in the z direction so that any derivatives of this are zero. The solutions are generated across the whole crystal in a leapfrog fashion, with the electric field and magnetic field solutions being calculated in alternating steps at each point in space. Figure 1.11 plots the photonic band structure for the TE modes of a square lattice as calculated using the FDTD method in [34]. A complete band gap is highlighted by the grey region.

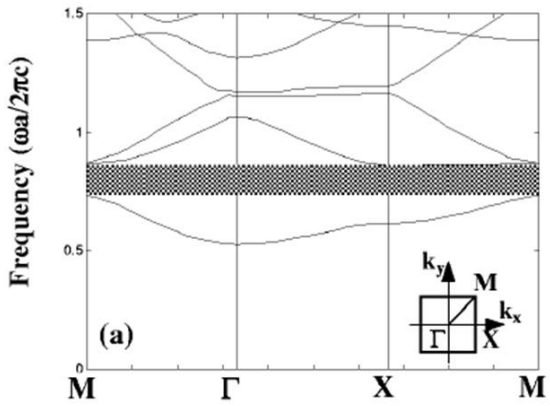

Figure 1.11: Photonic band structure for the TE modes of a square lattice as calculated using the FDTD in [34]. *Inset:* Reciprocal square lattice with crystal directions and lattice vectors shown.

The plane wave expansion method calculates the solutions to Maxwell's equations in frequency space using the Fourier coefficients of the lattice and Bloch waves. These Bloch waves are essentially plane waves with amplitudes that are modulated by periodic functions, hence the name plane wave expansion method. The resulting solutions to Maxwell's equations can be expressed in matrix form with eiqenvalue solutions expressed in frequency space. This method is slow due to the large number of calculations, and eigenvalues are often determined in an iterative procedure that improves the initial approximate solutions. Due to the symmetry of a photonic crystal reciprocal lattice, the eigenvalues can be calculated for the smallest symmetrical space, i.e. the irreducible Brilluoin zone (see figure 1.12), and then expanded out to encompass the whole crystal.

The first Brilluoin zone is a primitive cell in reciprocal space that is defined by the region within planes that bisect adjacent lattice points. Higher zones are formed by finding bisecting planes for the next nearest neighbours and are categorised by the number of plane boundaries that must be crossed to reach the central point. Figure 1.12 plots the reciprocal square lattice and the first Brilluoin zone (red square). The points X' and M' on the Brilluoin zone are symmetrically equivalent to X and M allowing computational models to save time by considering only the irreducible Brilluoin zone (blue triangle).

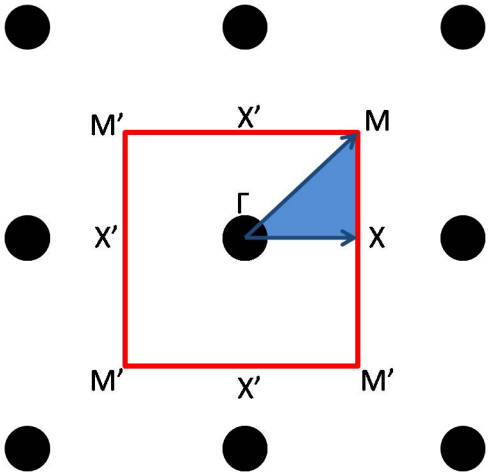

Figure 1.12: Reciprocal square lattice (black dots) with first Brilluoin zone (red square) and irreducible Brilluoin zone (blue triangle). Lattice vectors from Γ to X and Γ to M shown by blue arrows.

Figure 1.13 shows the TE and TM band structure for a square lattice as calculated using the PWEM in [33]. A complete band gap is highlighted in grey and this lies at similar frequencies to that in figure 1.11.

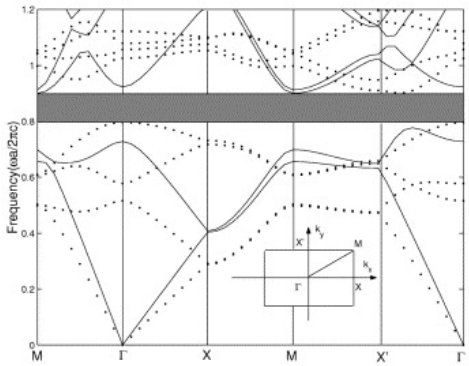

Figure 1.13: Photonic band structure for the TM modes (solid lines) and TE modes (dotted lines) of a square lattice as calculated using the PWEM in [33]. *Inset:* Reciprocal square lattice with crystal directions and lattice vectors shown.

The end result of both these models is an approximation of the photonic band structure for the chosen crystal. Slight variations to experimental results from a PCSEL are to be expected from both of these models as each of them consider the crystal to be an infinitely thick layer. However, both models predict similar results for the same crystal lattices. The FDTD method has advantages in terms of computational time for large scale irregular structures, such as defect cavities, as the requirements scale linearly with the crystal size and the physical properties of each lattice point can easily be altered. The PWEM is relatively quick for calculating band structures of two-dimensional photonic crystals, however, this method has limitations for modelling three-dimensional crystals as the number of plane waves (N) that must be used for accuracy is high, and the computational time scales as N^3.

1.3.2 Atom shapes and lattice designs

Various atom shapes and lattice designs have been considered, and these are modelled extensively in the literature [27,28,30,33–37]. Initial designs focussed on circular atom shapes as they are easier to model and require less computer run-time due to the symmetrical nature of the shape. Devices typically incorporate these circles for this reason and because the main fabrication method (electron beam lithography) can generate them easily [19–21, 23, 38].

Square and triangular lattices (see figure 1.5a) and b)) are most commonly used in PCSELs and other photonic crystal based devices [18, 20, 21, 23, 38, 40, 41]. These lattices are chosen for their relatively simple band structures with partial band gaps, allowing a choice of wavelengths to be targeted through manipulation of the period (using 1.2.14). Plus, if the most common three-dimensional photonic crystal designs (see figure 1.14a) and 1.14b) for the wood-pile and face-centred cubic structures respectively [9,24]) are broken down into a combination of two-dimensional planes, each plane has a two dimensional crystal with either a square or triangular lattice.

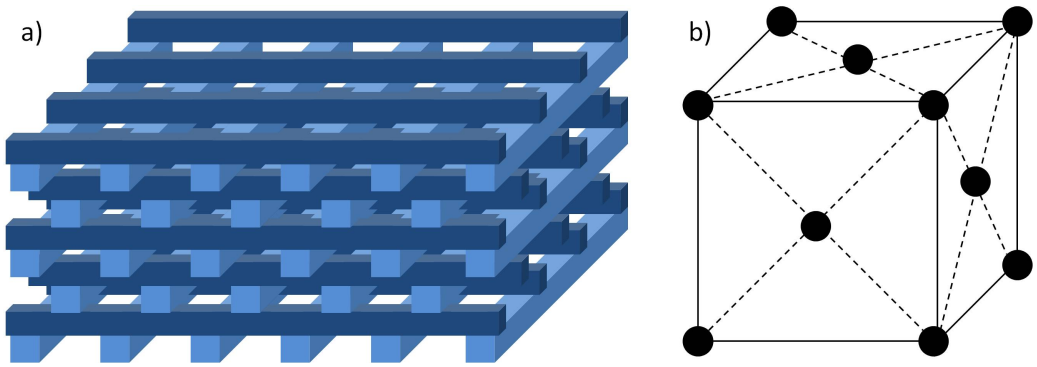

Figure 1.14: a) The woodpile structure created by micro-machining silicon wafers into strips and stacking them. Each layer is stacked perpendicular to the previous (different shades of blue) and adjacent parallel layers are offset by half a period. b) The face-centred cubic crystal structure employed by Yablonovitch *et al.*

Atom design helps break the 2D symmetry of the crystal and can cause disruptions in the electric and magnetic fields. This can then vary the opti-

cal confinement in the vertical direction, with increases (or decreases) in the confinement decreasing (or increasing) the amount of emitted light depending on the precise atom shape. Output efficiency was first found to increase by changing atom shape from circular to triangular [29]. Later models showed that high degrees of asymmetry along one axis of the atom shape result in enhanced emission [30].

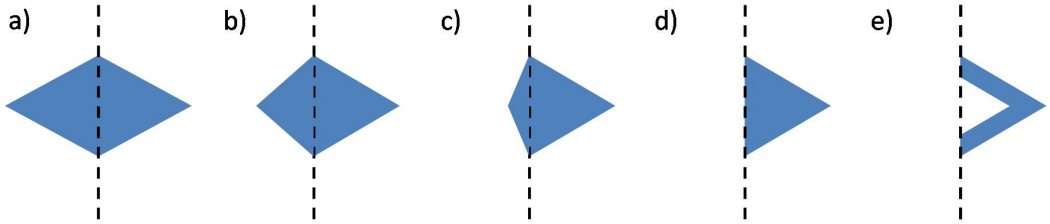

Figure 1.15: a) Symmetric diamond atom shape b) Asymmetric diamond shape c) Increased asymmetry of diamond shape d) Flattened left-hand side leaving triangular atom shape e) Chevron atom shape.

Figure 1.15 indicates the atom shapes considered by Kurosaka *et al.*, starting with the symmetric diamond in 1.15a). The extent of the atom shape on one side of the y-axis line of symmetry is reduced (1.15b)), and progressively this part of the shape is removed (1.15c) and d)) until the asymmetric chevron in 1.15e) is formed. In [30], allowed modes could be either leaky or non-leaky depending on the symmetry of the in-plane electric field distribution, and for non-leaky modes the vertical optical confinement is high enough to prevent emission. As the shape of the atom changes to something more asymmetric,

the confinement reduces and modes become more leaky.

Using these chevron atom shapes, additional attempts to reduce the symmetry of the crystal have been made by changing the unit cell of the photonic crystal. Figure 1.16 indicates the three types of chevron arrangement attempted in [42]. In figure 1.16b) and c), a square lattice is used and the chevrons are rotated relative to each other. The photonic crystal in figure 1.16b) has a unit cell (unit A) which is offset by half a period to increase asymmetry within the lattice. The type 3 arrangement (figure 1.16c)) has two different units cells side-by-side to break the symmetry. Unit A is the same as in figure 1.16b) and unit B is equivalent to unit A rotated by 180°.

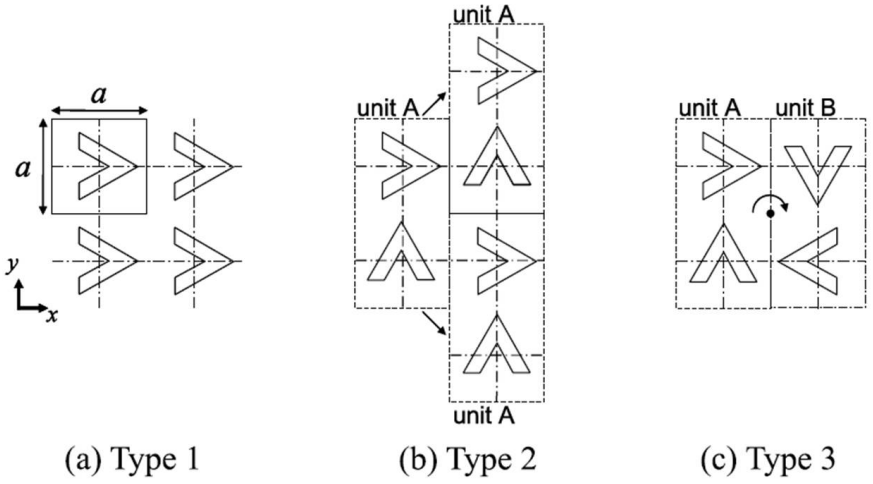

Figure 1.16: a) Square lattice with chevron atom shapes b) Chevrons in a square array but with unit A offset by half a period c) Square lattice with unit cell formed from a combination of unit A and unit B. *Adapted from* [42].

These different lattice and atom shapes result in more complex band structures (see figure 1.17), as the reduced symmetry increases the amount of lattice points within the first Brilluoin zone (figure 1.12) and this creates an increased amount of allowed modes.

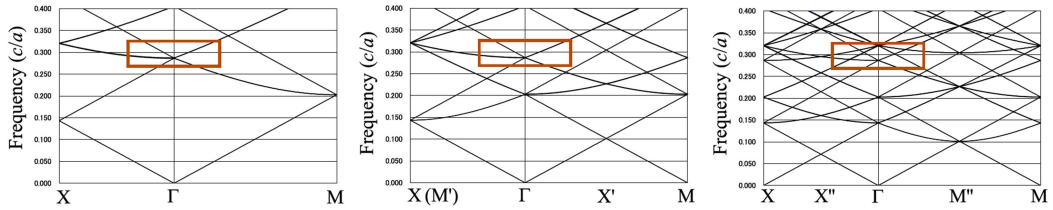

Figure 1.17: Photonic band structures for: a) Type 1 b) Type 2 c) Type 3 photonic crystals in figure 1.16. *Adapted from* [42].

1.3.3 Defect cavity lasers

A large amount of research has been conducted into the second main type of laser that includes a photonic crystal - the defect cavity laser. Defect cavity or photonic crystal micro-cavity (PCμC) lasers, [43] utilise a defect within the photonic crystal to create a nano-scale cavity. These devices have a large Q-factor due to the small size of the cavity and display low threshold current operation [44]. Single-mode operation is achieved by design of the photonic band structure, creating a photonic band gap into which a cavity defect can then introduce a donor or acceptor mode [45]. Light of this wavelength is then able to treat the defect as a small cavity with the surrounding photonic crystal

acting as effective mirrors on all sides. Increasing the size of the surrounding crystal has been found to create an exponential growth of the device Q-factor [46]. Defects can be formed by either removing a lattice point (figure 1.18a)) or enlarging one (figure 1.18b)). To optimise the cavity the position of the nearest neighbour lattice points are often adjusted as well.

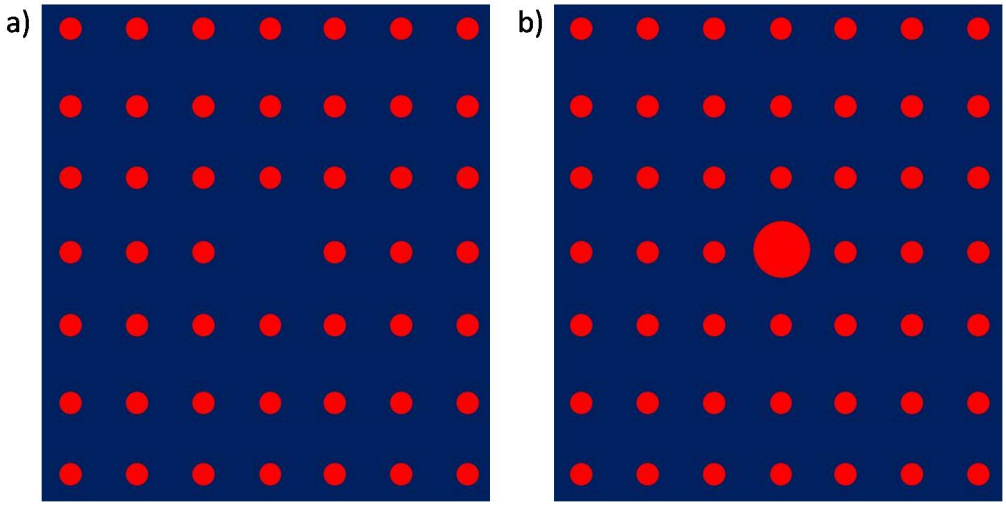

Figure 1.18: Square lattice photonic crystal with a defect cavity formed by a) removing an atom at the centre and b) enlarging an atom at the centre.

As the photonic crystal forms such effective mirrors on the edge of the defect cavity, complex device design is not essential, with fabrication as slab waveguides [47] or on air bridges within other structures [48] being typical. However, these type of devices only have the potential to achieve relatively low powers due to the small size of the resonant cavity, and tend to have poor beam emission properties.

1.3.4 PCSEL structures and fabrication methods

Semiconductor based PCSEL structures have typically aimed for target wavelengths in the approximate range of 1 μm to 1.55 μm using either existing InP or GaAs based technologies [20, 40]. In doing so they have the potential to be incorporated into larger, more complex devices or photonic integrated circuits. The photonic crystals within devices reported in the literature consist of part semiconductor and part void. These voids are assumed to consist of air, thus providing a high refractive index contrast with the semiconductor. In early PCSELs they were created as a result of the wafer fusion fabrication method outlined below. As PCSEL and semiconductor technologies have matured, research into gallium-nitride based devices (at shorter wavelengths) and airhole-retained overgrowth methods have also been undertaken [38].

The wafer fusion technique can be explained in the most basic terms as simply taking two wafers, one of which includes a patterned photonic crystal, and fusing them together to form a new structure. This process is actually more complicated than it sounds and involves designing two separate wafers that come together to form a waveguide for the PCSEL. Figure 1.19 is a schematic demonstrating this process as reported in [21, 22, 40]. Both wafer A and wafer B usually have multiple epitaxial layers, including an active layer, which form the final PCSEL structure. The fusing process involves heating

both wafers in a liquid phase epitaxy furnace system to a temperature of 620° for 30 minutes within a hydrogen atmosphere [40].

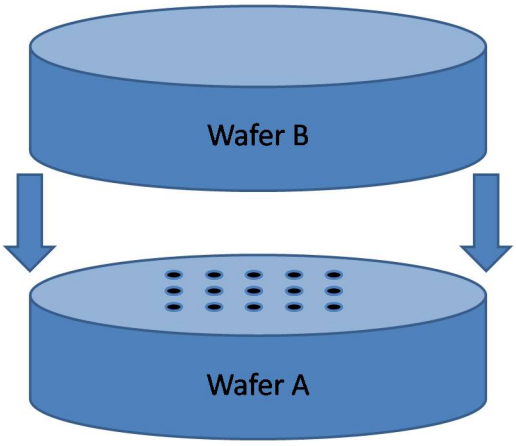

Figure 1.19: Basic schematic of the wafer fusion technique reported in [21, 22, 40].

The airhole-retained overgrowth (AROG) method involves a second epitaxial step [38]. This forms a planar layer above the patterned photonic crystal, allowing growth of the rest of the structure. In this method, metal-organic vapour phase epitaxy is used for overgrowth and the growth proceeds in a lateral direction using this technique. A small amount of SiO_2 is deposited at the bottom of each etched hole in the photonic crystal to help prevent GaN growth and thus leave a void in each. Until recently, a two-step growth method had only been reported in these GaN based structures or for the GaAs structures included in this thesis. However, presentations at the 10th conference on lasers and electro-optics Pacific rim (CLEO-PR) in 2013 reported a two step growth

process using an AlGaAs structure is also possible [49].

The third method of PCSEL fabrication reported in the literature corresponds to those using an organic gain medium [17,18]. These typically involve patterning and etching a SiO_2 layer with a photonic crystal, before spin-coating the solid-state organic material on top [18]. This forms a waveguide with outer layers of SiO_2 and air, and the organic medium forming the core (figure 1.20).

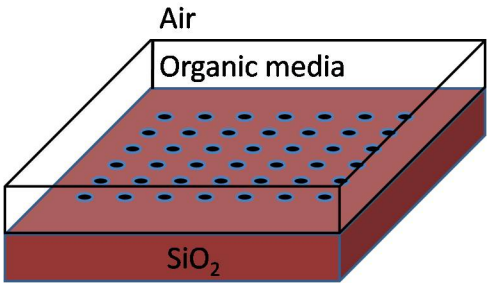

Figure 1.20: Schematic of a PCSEL waveguide utilising an organic gain medium as in [18].

In all of these fabrication methods patterning is typically done by electron beam lithography and reactive ion etching [50–52]. Alternative techniques such as focused ion beam milling [53, 54] or nano-imprinting [55, 56] are used less often due to either time limitations or financial restraints.

1.3.5 PCSEL characterisation

Characteristics of the first PCSELs demonstrated the huge potential of these devices. Early results were recorded at room temperature operating under

pulsed conditions, and these were quickly followed by CW results [20]. Figure 1.21 plots room temperature CW light-output versus current injection (LI) and spectral characteristics reported in [20]. A single lasing peak is observed in the spectra close to $\lambda = 960$ nm (figure 1.21a)).

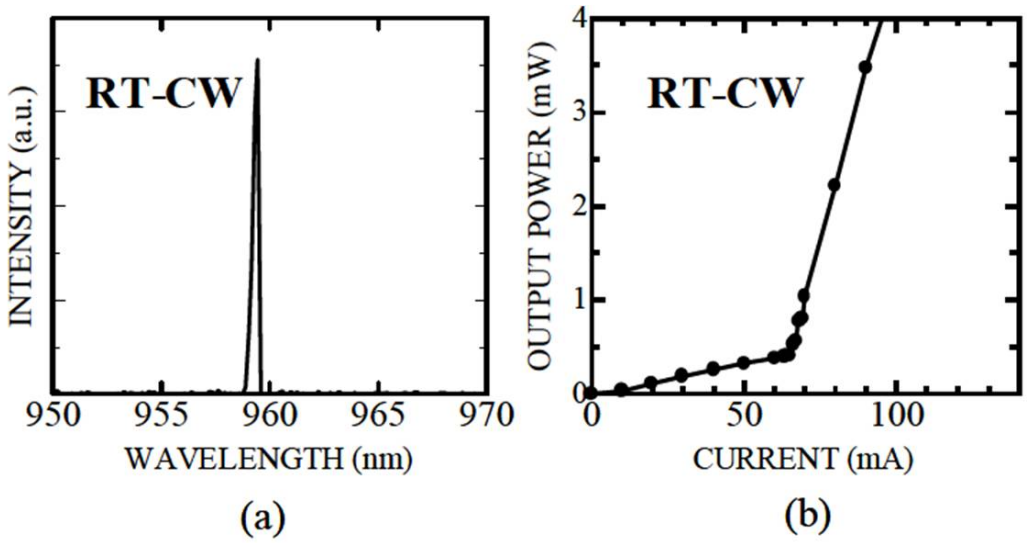

Figure 1.21: Early room temperature a) LI and b) spectral results under CW operation. *Adapted from* [20].

Basic LI curves and electroluminescence spectra reported in the literature demonstrate these devices achieve reasonably high single-mode powers and relatively low threshold currents (approximately 60 mA in figure 1.21b)). Spectra also indicate that suitable waveguide and period design allowed operation at various emission wavelengths including 406 nm, 960 nm, 1.285 μm and 1.55 μm [20, 22, 38, 40]. Figure 1.22 shows laser oscillation of the same wavelength

measured at separate points that are a distance of over 500 μm apart [22] suggesting that emission is coherent over large areas.

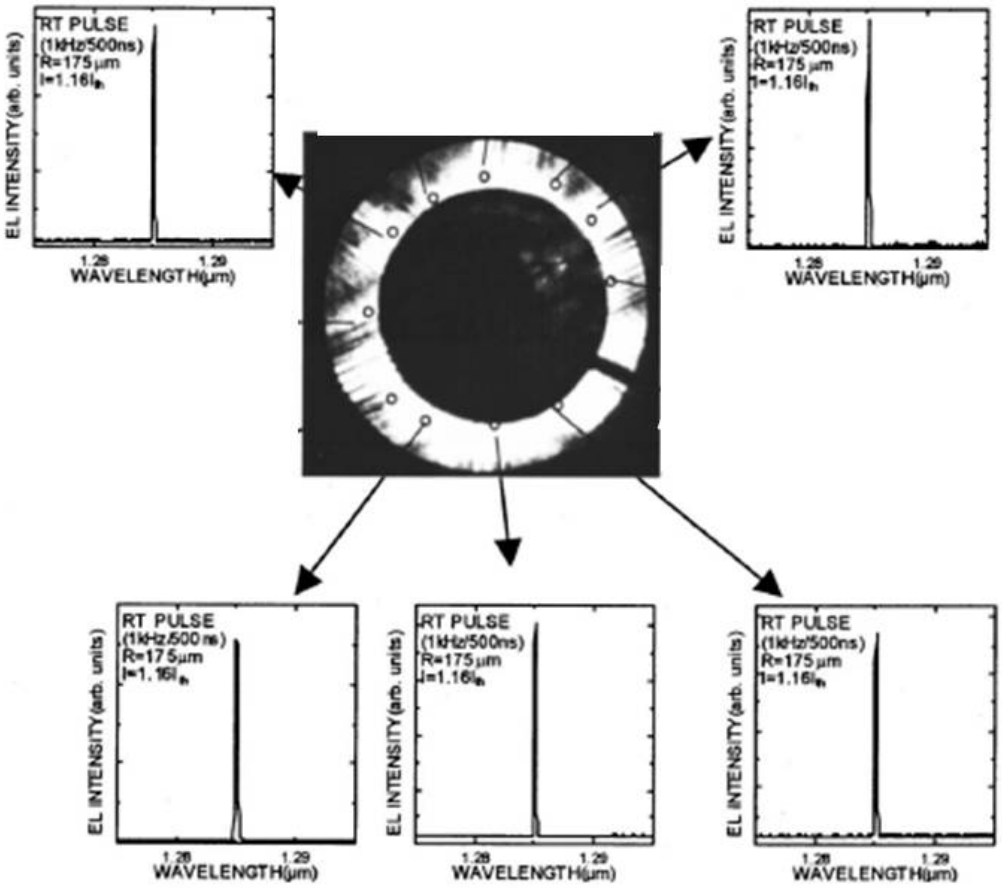

Figure 1.22: Coherent spectral emission from various points around the electrode. *Adapted from* [22].

From measurements of the emission spectra at a variety of angles relative to the photonic crystal the band structure has been mapped, and lasing has been shown to occur at the photonic band edges [21].

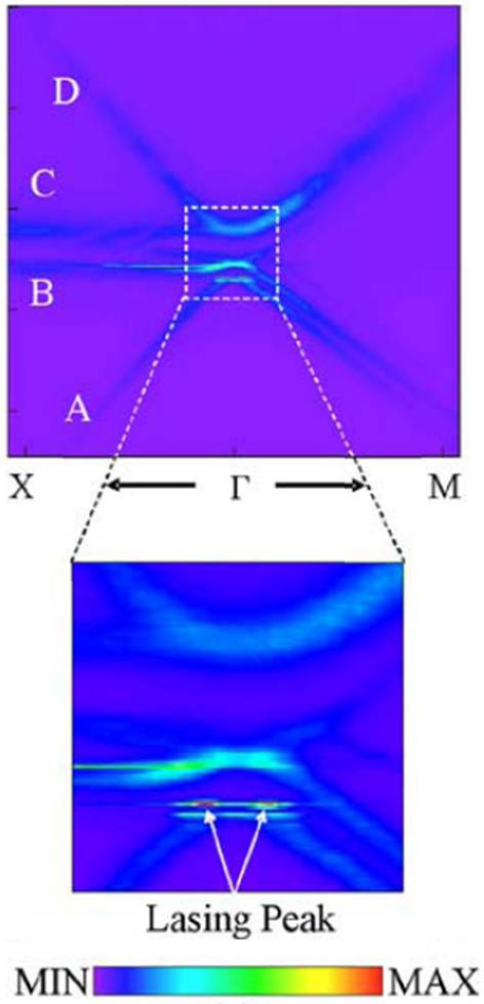

Figure 1.23: Experimentally mapped band structure indicating laser action occurring at the band edge near the Γ point. *Adapted from* [21].

Figure 1.23 plots the band structure close to a partial TE mode band gap at the Γ point, with the lasing peak indentified when magnifying this region. In order to determine the coupling strength of the photonic crystal, Sakai *et al.* calculated theoretical coupling coefficients of $\kappa_1 = 1700\ \mathrm{cm}^{-1}$ and $\kappa_3 = 800$

cm^{-1} using 1.2.4-1.2.7 (for a square lattice photonic crystal). They also used emission wavelengths at the different band edges to determine experimental coupling coefficients of $\kappa_1 = 4300\ cm^{-1}$ and $\kappa_3 = 740\ cm^{-1}$ (see 5.4.1-5.4.3 in section 5.4).

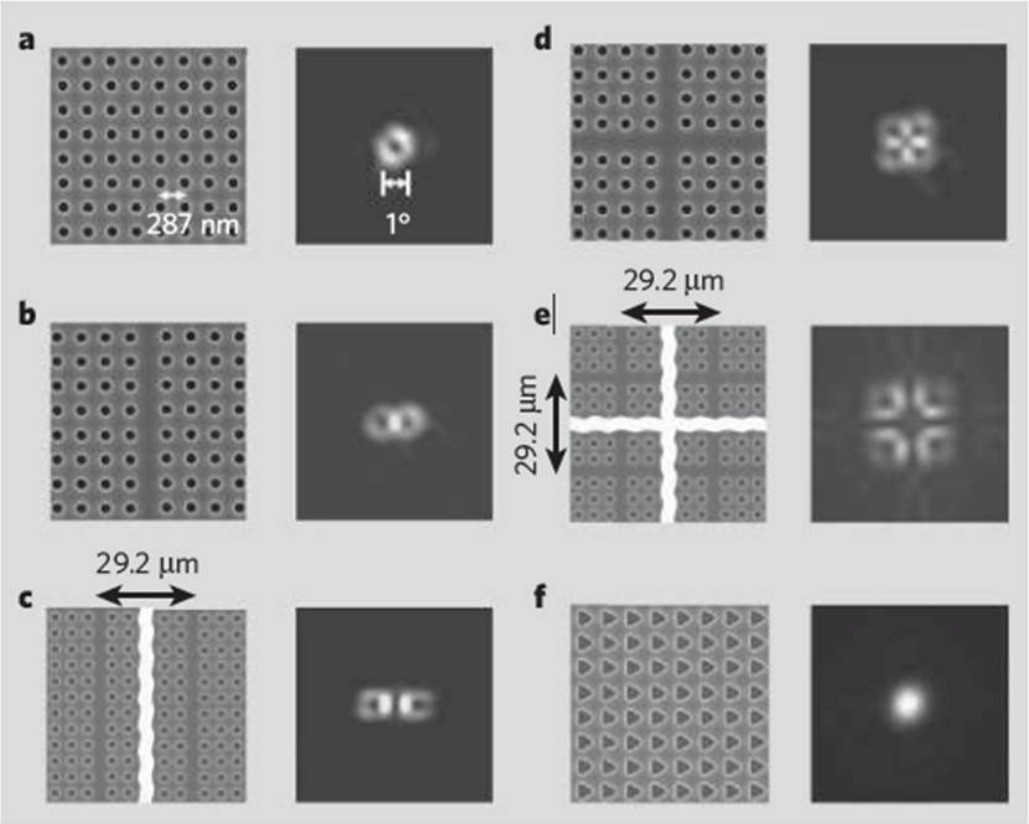

Figure 1.24: Lattice shapes and corresponding far-field patterns for a) a square lattice with circular atoms b) a square lattice with a line defect and circular atoms c) a square lattice with two line defects separated by 29.2 μm d) square lattice with two line defects crossing at the centre e) Four crossed line defects in a square lattice separated by 29.2 μm f) a square lattice with triangular atoms [23].

Far-field patterns that are directly linked to the shape of the photonic crystal lattice (see figure 1.24), and beam divergences as low as 1° [23] are also reported in the literature. Of particular note is figure 1.24f), where triangular atoms in a square lattice create a circular, single-lobed, far-field pattern.

1.4 Gaps in the knowledge

1.4.1 All-semiconductor photonic crystals

Early 3D photonic crystal models found complete photonic band gaps using high refractive index contrast materials such as aluminium and air (a refractive index contrast of 3.6:1, with n = 3.6 for aluminium at microwave frequencies and air (n = 1) [10]). The similar refractive indices of semiconductors such as GaAs and InP to aluminium suggested obvious possiblities for optical wavelengths, however, the period required in these 3D photonic crystals makes fabrication complicated. This led to a significant amount of research into finding a two-dimensional solution, naturally incorporating voids within the structure to keep this high refractive index contrast. The chosen lattice designs of PCSELs incorporating 2D photonic crystals create a partial band gap, and this appears to be sufficient to achieve lasing. Photonic crystals or PCSELs using materials of smaller index contrast, such as between two semiconductors, and their device characteristics, do not appear to be reported in the literature.

1.4.2 Regrown GaAs PCSELs

PCSELs with buried photonic crystals (or gratings) are typically created by wafer fusion (discussed in section 1.3.4), however, the AROG method demonstrates a second epitaxial step can be used to create a two dimensional buried grating for GaN based devices. Previous work carried out at the University of Sheffield also showed that a one-dimensional buried grating with emission at 1 μm can be formed through epitaxial regrowth [57]. There appears to be no report in the literature of a 2D epitaxially regrown PCSEL using GaAs/AlGaAs based materials to emit at wavelengths close to 1 μm, apart from work reported in this thesis. To the best of my knowledge regrowth that infills a two-dimensional photonic crystal to remove voids is not reported elsewhere.

1.4.3 Low temperature characterisation

The characteristics of PCSELs reported in the literature focus primarily on achieving lasing at room temperature under CW operation and the unique properties created by the photonic crystal. The operating characteristics and far-field patterns at low temperatures do not appear to be reported. Other types of devices (e.g. vertical cavity surface emitting lasers) have tunable wavelength selection through temperature variations. Such detuning characteristics for PCSELs do not appear to be reported in the literature.

1.5 Thesis outline

This thesis covers the waveguide modelling and fabrication of an all-semiconductor PCSEL by epitaxial regrowth to demonstrate that the relatively small refractive index contrast between two semiconductor materials is sufficient for lasing to occur. Basic characteristics at low temperature are investigated, as well as detuning of lasing wavelength with temperature. Characterisation of the coupling strength of the photonic crystal and external feedback effects at room temperature is also undertaken.

Waveguide modelling of a semiconductor structure incorporating a photonic crystal is discussed in chapter 2. Mode confinement within a waveguide structure is introduced and a PCSEL design based on a $\lambda = 980$ nm distributed feedback laser is outlined. The design considerations discussed in this chapter, such as layer thicknesses and material compositions, are varied in an attempt to maximise coupling to the photonic crystal whilst still maintaining decent mode overlap with the active region.

The effect of design parameters is also considered for a replacement void-semiconductor photonic crystal within the waveguide, drawing a surprising conclusion on the coupling of high-index contrast photonic crystals in a semiconductor waveguide.

The fabrication of an all-semiconductor PCSEL by epitaxial regrowth is

outlined in chapter 3. The proof-of-concept process is outlined first, and then design considerations such as alternative patterning techniques and regrowth development steps are discussed.

Chapter 4 is a review of the basic device characteristics operating at low temperatures. In this section of the thesis, laser oscillation is demonstrated and characteristics that indicate the photonic crystal is responsible are highlighted. The dependence of the lasing wavelength on temperature and photonic crystal period is discussed, and also the effect of detuning between the gain peak and lasing wavelength on threshold current.

Room temperature characterisation is outlined in chapter 5, starting with basic characteristics. Photonic band structure measurements follow and these demonstrate the photonic crystal is influencing the device emission and quantify the coupling strength. The effects of external feedback on threshold current and output power are also discussed.

A brief summary of the thesis and details of suggested further work on this topic for the future are covered in chapter 6.

References

[1] "Inhibited spontaneous emission in solid-state physics and electronics" E. Yablonovitch. Phys. Rev. Lett., **58**, No. 20, 2059 (1987)

[2] "Strong localization of photons in certain disordered dielectric superlattices" S. John. Phys. Rev. Lett., **58**, No. 23, 2486 (1987)

[3] "Coupled wave theory of distributed feedback lasers" H. Kogelnik and C. V. Shank. J. Appl. Phys., **43**, No. 5, 2327 (1972)

[4] "Room-temperature operation of low-threshold separate-confinement heterostructure injection laser with distributed feedback" H. C. Casey Jr. S. Somekh and M. Ilegems. Appl. Phys. Lett., **27**, No. 3, 142 (1975)

[5] "Single-heterostructure distributed-feedback GaAs-diode lasers" R. D. Burnham, D. R. Scrifres and W. Streifer. IEEE J. Quant. Electron., **11** No. 7, 440 (1975)

[6] "Surface-emitting laser-its birth and generation of new optoelectronics field" K. Iga. IEEE J. Sel. Top. Quantum Electron., **6**, No. 6, 1201 (2000)

[7] "GaInAsP/InP Surface Emitting Injection Lasers" H. Soda, K-I. Iga, C. Kitahara and Y. Suematsu. Jpn. J. Appl. Phys., **18**, No. 12, 2329 (1979)

[8] "Microcavity GaAlAs/GaAs surface-emitting laser with Ith = 6 mA" K. Iga, S. Kinoshita and F. Koyama. Electron. Lett., **23**, No. 3, 135 (1987)

[9] "Photonic band structure: The face-centred-cubic case" E. Yablonovitch and T. J. Gmitter. Phys. Rev. Lett., **63**, No. 18, (1989)

[10] "Photonic band structure: The face-centred-cubic case employing non-spherical atoms" E. Yablonovitch, T. J. Gmitter and K. M. Leung. Phys. Rev. Lett., **67** No. 17 (1991)

[11] "Photonic band structure of two-dimensional systems: The triangular lattice" M. Plihal and A. A. Maradudin. Phys. Rev. B, **44**, No. 16, 8565 (1991)

[12] "Two-dimensional photonic band structures" M. Plihal, A. Shambrook, A. A. Maradudin and P. Sheng. Optics Commun., **80**, Iss. 3-4, 199 (1991)

[13] "Photonic crystals: Putting a new twist on light" J. D. Joannopoulos, P. R. Villeneuve and S. Fan. Nature, **386**, 143 (1997)

[14] "Modal analysis of optical guides with two dimensional photonic bandgap boundaries" H. Benisty. J. Appl. Phys., **79**, No. 10, 7843 (1996)

[15] "Linear waveguides in photonic-crystal slabs" S. G. Johnson, P. R. Villeneuve, S. Fan and J. D. Joannopoulos. Phys. Rev. B, **62**, No. 12, 8212 (2000)

[16] "High transmission through sharp bends in photonic crystal waveguides" A. Mekis, J. C. Chen, I. Kurland, S. Fan, P. R. Villeneuve and J. D. Joannopoulos. Phys. Rev. Lett., **77**, No. 18, 3787 (1996)

[17] "Organic lasers based on lithographically defined photonic-bandgap resonators" M. Berggren, A. Dodabalapur, R. E. Slusher, Z. Bao, A. Timko and O. Nalamasu. Electron. Lett., **34**, No. 1, 90 (1998)

[18] "Laser action from two-dimensional distributed feedback in photonic crystals" M. Meier, A. Mekis, A. Dodabalapur, A. Timko, R. E. Slusher, J. D. Joannopoulos and O. Nalamasu. Appl. Phys. Lett., **74**, No. 1, 7 (1999)

[19] "Coherent two-dimensional lasing action in surface-emitting laser with triangular-lattice photonic crystal structure" M. Imada, S. Noda, A. Chutinan, T. Tokuda, M. Murata and G. Sasaki. Appl. Phys. Lett., **75**, No. 3, 316 (1999)

[20] "Room temperature continuous wave operation of a surface emitting two dimensional photonic crystal laser" D. Ohnishi, T. Okano, M. Imada and S. Noda. Optics Express, **12**, No. 8, 1562 (2004)

[21] "Lasing band-edge identification for a surface-emitting photonic crystal laser" K. Sakai, E. Miyai, T. Sakaguchi, D. Ohnishi, T. Okano and S. Noda. IEEE J. Sel. Areas Commun., **23**, No. 7, 1335 (2005)

[22] "Multidirectionally distributed feedback photonic crystal lasers" M. Imada, A. Chutinan, S. Noda and M. Mochizuki. Phys. Rev. B, **65**, No. 19, 195306-1 (2002)

[23] "Lasers producing tailored beams" E. Miyai, K. Sakai, T. Okano, W. Kunishi, D. Ohnishi and S. Noda. Nature, **441**, No. 7096, 946 (2006)

[24] "Optical properties of three-dimensional photonic crystals bassed on III-V semiconductors at infrared to near-infrared wavelengths" S. Noda, N. Yamamoto, H. Kobayashi, M. Okano and K. Tomoda. Appl. Phys. Lett., **75**, No. 7, 905 (1999)

[25] "A three-dimensional photonic crystal operating at infrared wavelengths" S. Y. Lin, J. G. Fleming, D. L. Hetherington, B. K. Smith, R. Biswas, K. M. Ho, M. M. Sigalas, W. Zubrzycki, S. R. Kurtz and J. Bur. Nature, **394**, 251 (1998)

[26] "Photonic Crystals Molding the Flow of Light" Princeton University Press, 2nd edition (2008) J. D. Joannopoulos, S. G. Johnson, J. N. Winn and R. D. Meade.

[27] "High extraction efficiency of spontaneous emission from slabs of photonic crystals" S. Fan, P. R. Villeneuve, J. D. Joannopoulos and E. F. Schubert. Phys. Rev. Lett., **78**, No. 17, 3294 (1997)

[28] "Two-dimensional Kagome structure, fundamental hexagonal photonic crystal configuration" J. B. Nielsen, T. Sondergaard, S. E. Barkou, A. Bjarklev, J. Broeng and M. B. Nielsen. Electron. Lett., **35**, No. 20, 1736 (1999)

[29] "High-power single-lobed surface-emitting photonic-crystal laser" W. Kunishi, D. Ohnishi, E. Miyai, K. Sakai and S. Noda. Conference proceedings (CMKK1) Lasers and Electro-optics and Quantum Electronics and Laser Science (CLEO/QELS) conference (2006)

[30] "Controlling vertical optical confinement in two-dimensional surface-emitting photonic crystal lasers by shape of air holes" Y. Kurosaka, K. Sakai, E. Miyai and S. Noda. Optics Express, **16**, No. 22, 18485 (2008)

[31] "Coupled-wave model for square-lattice two-dimensional photonic crystal with transverse-electric-like mode" K. Sakai, E. Miyai and S. Noda. Appl. Phys. Lett., **89**, 021101 (2006)

[32] "Design optimization for high-brightness surface-emitting photonic crystal distributed feedback lasers" I. Vurgaftman and J. R. Meyer. IEEE J. Quantum Electron., **39**, No. 6, 689 (2003)

[33] "A plane-wave expansion method based on the effective medium theory for calculating the band structure of a two-dimensional photonic crystal" S. Xiao, L. Shen and S. He. Phys. Lett. A, **313**, 132 (2003)

[34] "A nonorthogonal finite-difference time-domain method for computing the band structure of a two-dimensional photonic crystal with dielectric and metallic inclusions" M. Qiu and S. He. J. Appl. Phys., **87**, No. 12, 8268 (2000)

[35] "Photonic crystals Theory, Applications, and Fabrication" Wiley (2009), D. W. Prather, S. Shi, A. Sharkawy, J. Murakowski and G. J. Schneider, p108

[36] "Existence of a photonic band gap in two dimensions" R. D. Meade, K. D. Brommer, A. M. Rappe and J. D. Joannopoulos. Appl. Phys. Lett., **61**, No. 4, 495 (1992)

[37] "Photon band structures: The plane-wave method" K. M. Leung and Y. F. Liu. Phys. Rev. B, **41**, No. 14, 10188 (1990)

[38] "GaN photonic-crystal surface-emitting laser at blue-violet wavelengths" H. Matsubara, S. Yoshimoto, H. Saito, Y. Jianglin, Y. Tanaka and S. Noda. Science, **319**, 445 (2008)

[39] "Photonic crystal band edge laser array with a holographically generated square-lattice pattern" C-O. Cho, J. Jeong, J. Lee, H. Jeon, I. Kim, D. H. Jang, Y. S. Park and J. C. Woo. Appl. Phys. Lett., **87**, 161102 (2005)

[40] "Semiconductor lasers with one- and two-dimensional air/semiconductor gratings embedded by wafer fusion technique" M. Imada, S. Noda, A. Chutinan, M. Murata and G. Sasaki. IEEE J. Sel. Top. Quantum Electron., **5**, No. 3, 658 (1999)

[41] "Room-temperature triangular-lattice two-dimensional photonic band gap lasers operating at 1.54 μm" J-K. Hwang, H-Y. Ryu, D-S. Song, I-Y. Han, H-W. Song, H-K. Park, Y-H. Lee and D-H. Jang. Appl. Phys. Lett., **76**, No. 21, 2982 (2000)

[42] "Band structure observation of 2D photonic crystal with various V-shaped air-hole arrangements" Y. Kurosaka, S. Iwahashi, K. Sakai, E. Miyai, W. Kunishi, D. Ohnishi and S. Noda. IEICE Electron. Exp., **6**, No. 13, 966 (2009)

[43] "Two-dimensional photonic band-gap defect mode laser" O. Painter, R. K. Lee, A. Scherer, A. Yariv, J. D. O'Brien, P. D. Dapkus and I. Kim. Science, **284**, 1819 (1999)

[44] "High-Q photonic nanocavity in a two-dimensional photonic crystal" Y. Akahane, T. Asano, B-S. Song and S. Noda. Nature, **425**, 944 (2003)

[45] "Donor and acceptor modes in photonic band structure" E. Yablonovitch, T. J. Gmitter, R. D. Meade, A. M. Rappe, K. D. Brommer and J. D. Joannopoulos. Phys. Rev. Lett., **67**, No. 24, 3380 (1991)

[46] "Microcavities in photonic crystals: Mode symmetry, tunability, and coupling efficiency" P. R. Villeneuve, S. Fan and J. D. Joannopoulos. Phys. Rev. B, **54**, No. 11, 7837 (1996)

[47] "High quality two-dimensional photonic crystal slab cavities" T. Yoshie, J. Vuckovic, A. Scherer, H. Chen and D. Deppe. Appl. Phys. Lett., **79**, No. 26, 4289 (2001)

[48] "Air-bridge microcavities" P. R. Villenueve, S. Fan, J. D. Joannopoulos, K-Y. Lim, G. S. Petrich, L. A. Kolodziejski and R. Reif. Appl. Phys. Lett., **67**, No. 2, 167 (1995)

[49] "High power photonic-crystal surface-emitting lasers" K. Hirose, Y. Kurosaka, A. Watanabe, T. Sugiyama, Y. Liang and S. Noda. Oral presentation ThI1-4 at the Conference on Lasers and Electro-Optics Pacific Rim (CLEO-PR) (2013)

[50] "Fabrication of photonic bandgap crystals" C. C. Cheng and A. Scherer. J. Vac. Sci. Technol. B, **13**, 2696 (1995)

[51] "III-nitride blue and ultraviolet photonic crystal light emitting diodes" T. N. Oder, K. H. Kim, J. Y. Lin and H. X. Jiang. Appl. Phys. Lett., **84**, No. 4, 466 (2004)

[52] "Fabrication of low loss two-dimensional InP photonic crystals by inductively coupled plasma etching" F. Pommereau, L. Legouezigou, S. Hubert, S. Sainson, J-P. Chandouineau, S. Fabre, G-H. Duan, B. Lombardet, R. Ferrini and R. Houdre. J. Appl. Phys., **95**, No. 5, 2242 (2004)

[53] "Near-infrared Yablonovite-like photonic crystals by focused ion beam etching of macroporous silicon" A. Chelnokov, K. Wang, S. Rowson, P. Garoche and J-M. Lourtioz. Appl. Phys. Lett., **77**, No. 19, 2943 (2000)

[54] "a $SiO_x < Er >$ active photonic crystal resonator membrane fabricated by focused Ga^+ ion beam" D. S. L. Figueira, L. A. M. Barea, F. Vallini,

P.F. Jarschel, R. Lang and N. C. Frateschi. Opt. Express, **20**, No. 17, 18774 (2012)

[55] "Spontaneous emission control of colloidal nanocrystals using nanoimprinted photonic crystals" V. Reboud, N. Kehagias, C. M. Sotomayor Torres, M. Zelsmann, M. Striccoli, M. L. Curri, A. Agostiano, M. Tamborra, M. Fink, F. Reuther and G. Gruetzner. Appl. Phys. Lett., **90**, 011115 (2007)

[56] "Fabrication of semiconductor and polymer based photonic crystals using nanoimprint lithography" E. M. Arakcheeva, E. M. Tanklevskaya, S. I. Nesterov, M. V. Maksimov, S. A. Gurevich, J. Seekamp and C. M Sotomayor Torres. Tech. Physics, **50**, Iss. 8, 1043 (2005)

[57] "Distributed feedback laser employing buried GaAs/InGaP index-coupled grating" B. J. Stevens, K. M. Groom, J. S. Roberts, P. W. Fry, D. T. D. Childs and R. A. Hogg. Electron. Lett., **46**, No. 15 (2010)

2 Waveguide Modelling

2.1 Introduction

The periodic refractive index contrast within a photonic crystal causes feedback at a specific wavelength as discussed in section 1.2.2. By fabricating a photonic crystal within a planar waveguide a PCSEL can be created. However, for a PCSEL to achieve sufficient feedback for lasing the waveguide requires optimisation of mode overlap with the photonic crystal and gain regions. This chapter describes single and multi-mode waveguiding; introduces a possible waveguide structure for an all-semiconductor PCSEL; and looks at optimising this structure in terms of achieving maximum coupling to the photonic crystal, whilst still maintaining significant mode overlap with the active region. Comparison of the waveguided mode for a structure containing either an all-semiconductor, or a void-semiconductor photonic crystal, also demonstrates how the effective refractive index of the photonic crystal layer is significant for optimal mode overlap, indicating an advantage of using epitaxial regrowth to eliminate voids.

2.2 Background

Previous PCSELs which incorporate voids have often used InP waveguides to target wavelengths of 1.3 - 1.5 μm [1–4]. These devices have applications within the telecommunications industry, whilst other wavelengths worthy of consideration for biomedical and data storage applications include those of 850 nm and 980 nm. The ability of a device structure to guide light of these wavelengths is dependent on many parameters. In particular, these parameters include epitaxial material choices, as the band gap and absorption properties of semiconductor materials are wavelength dependent. For wavelengths around 1 μm, previous waveguides have typically utilised an epitaxial structure consisting of GaAs and AlGaAs layers [5, 6]. For shorter wavelengths the band gap of GaAs presents a problem. However, this thesis focuses on achieving a 980 nm PCSEL, for which an AlGaAs-GaAs waveguide is suitable. In order to achieve feedback and to tune the emission wavelength of a PCSEL, photonic crystal design is key. However, optimal confinement of an optical mode within the structure is also essential, as this ensures that there is a sufficient source of light, at the relevant wavelength, being injected into the photonic crystal. Therefore, this chapter focuses on waveguide design for a $\lambda = 980$ nm PCSEL, and considers the effects of varying structural parameters on mode confinement and profiles.

2.3 Theory

The propagation of light can be fully described by the wave equation (2.3.1) and the modes of a dielectric waveguide at a (radian) frequency ω are solutions of this.

$$\nabla^2 E(r) + k_0^2 n^2(r) E(r) = 0 \tag{2.3.1}$$

where $k_0^2 = \omega^2 \mu \epsilon_0 = (2\pi/\lambda)^2$ and n is the index of refraction [7].

Therefore, to determine the modes of a waveguide the wave equation needs to be solved for the relevant parameters of that structure. However, semiconductor waveguides often employ complex epitaxial structures with many layers, which makes the mathematics more complicated. For a mode to exist across the whole structure it must satisfy the wave equation in each of the layers. The form of the solution can be different in each layer, but must still be continuous at the interface boundaries. To achieve this the solutions must be continuous in terms of the tangential components of E and H at the interfaces.

The form of the solution to the electric field, E(r), in 2.3.1 is taken as:

$$E(r,t) = E(x,y)e^{i(\omega t - \beta z)} \tag{2.3.2}$$

so that 2.3.1 becomes:

$$\left(\frac{\delta^2}{\delta x^2} + \frac{\delta^2}{\delta y^2}\right) E(x,y) + [k_0^2 n^2(r) - \beta^2] E(x,y) = 0 \qquad (2.3.3)$$

From this, the behaviour of light within a waveguide can be determined by assuming it is a dielectric slab with variation in refractive index in only one of the dimensions. For the waveguide modelling conducted in this thesis, the software package Fimmwave [8] was used to determine solutions for a slab waveguide.

This calculates mode propogation through each of the layers in the structure with boundary conditions set by each of the adjacent layers. Figure 2.1 illustrates a simple 3-layer slab waveguide with light confined in the central region. Each layer of the waveguide is numbered region I-III and has the respective refractive indices n_1, n_2 and n_3 indicated. In this case the structural composition is simple and the number of boundary conditions is low, with light confined to region II when $n_2 > n_1$ and $n_2 > n_3$.

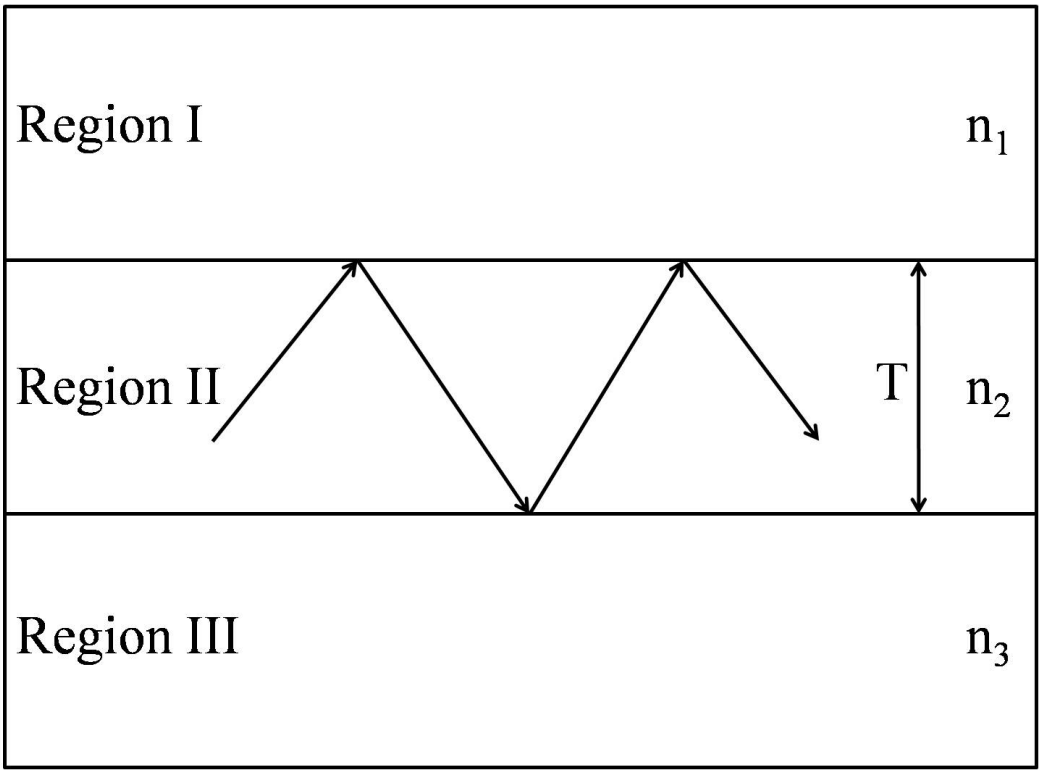

Figure 2.1: Waveguided light in a simple slab waveguide structure consisting of 3 regions with refractive indices n_1, n_2 and n_3.

For each layer in figure 2.1, 2.3.1 can be solved as a function of the propagation constant β, at a fixed frequency ω. An outline of the mode can be found by examining the function of the solution (2.3.2), whilst ensuring that the electric field, E, and $\frac{\delta^2 E}{\delta x^2}$, agree at the layer interfaces using 2.3.3. Assuming that $n_2 > n_3 > n_1$, figure 2.2 plots five different mode possibilities for different values of the propagation constant β, whilst still ensuring boundary conditions are met.

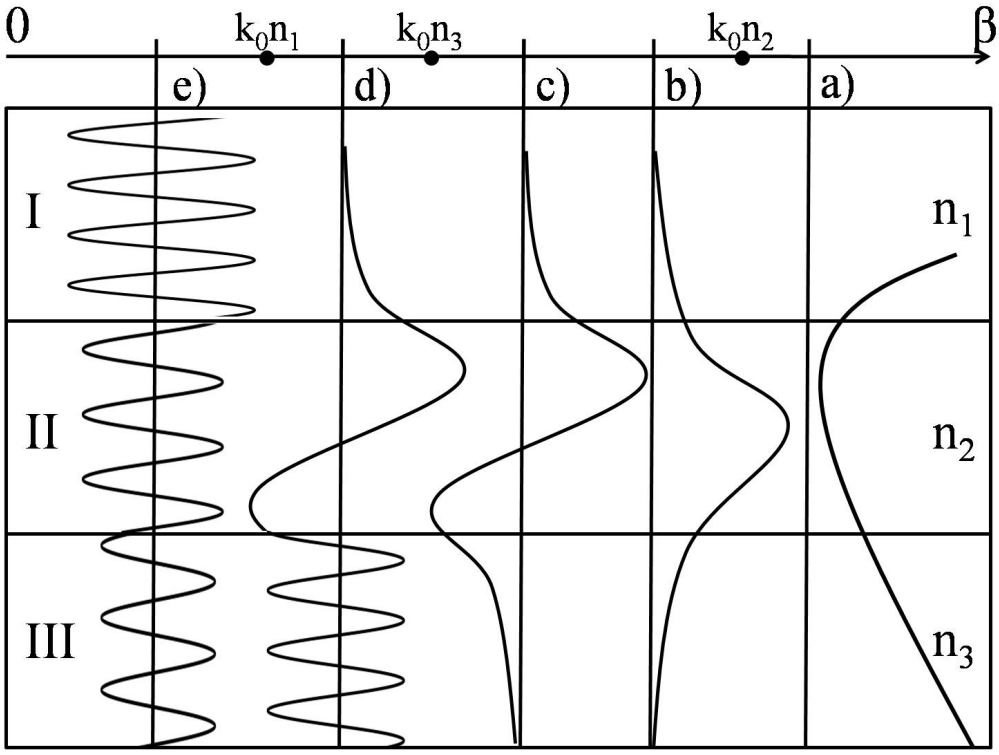

Figure 2.2: Possible mode profiles at varying values of propagation constant β for a simple 3 layer slab waveguide. *Adapated from* [7].

In figure 2.2, mode a) corresponds to a propagation constant, $\beta > k_0 n_2$, modes b) and c) satisfy $k_0 n_3 < \beta < k_0 n_2$, mode d) corresponds to $k_0 n_1 < \beta < k_0 n_3$, and for mode e) $0 < \beta < k_0 n_1$. The electric field in mode a) increases away from the centre of the waveguide so that the solution is not bound and thus does not correspond to a real wave. Modelling situations that yield solutions of this form shall subsequently be referred to as unbound modes. For modes b) and c) a solution exists such that the field is confined

or bound to the central layer of the simple structure in figure 2.1. For more complicated structures, modes confined to the central layers with decaying exponential solutions in the outermost layers shall be considered a bound mode (provided they still satisfy the boundary conditions at each interface). Figure 2.2 also plots mode d), which has an exponential solution in region I and sinusoidal solutions in regions II and III. Modes of this type are often referred to as substrate radiation modes. Sinusoidal modes in all three regions, such as mode e), are known as waveguide radiation modes. For solutions in the regime $k_0 n_3 < \beta < k_0 n_2$, such as modes b) and c) in figure 2.2, only discrete values of β will satisfy the boundary conditions. As the thickness of region II (T in figure 2.1) is increased, the fundamental transverse electric (TE) mode becomes bound (mode b). Further increases in the thickness of region II will then allow additional bound modes to exist. The number of bound modes within the waveguide in figure 2.1 is therefore dependent on the thickness of region II, the frequency ω and the indices of refraction, n_1, n_2, n_3.

The fraction of the mode within each layer of the waveguide, normalised against the sum of the mode in every waveguide layer, is defined as the confinement factor for the purposes of this thesis. Software modelling packages such as Fimmwave [8] can calculate this value to a high degree of precision for complicated waveguides, provided layer thicknesses and refractive indices are

accurately known. Fimmwave uses a fully-vectorial solver and the Film Mode Matching Method [9, 10] to model a waveguide consisting of various layers in the vertical direction. Each of these layers is constant in the horizontal direction and a two-dimensional mode is constructed from the one-dimensional TE and TM modes ensuring boundary conditions are met throughout the structure.

Previous work has shown that this confinement factor, Γ, can be used to determine the coupling coefficient, κ, for a distributed feedback (DFB) grating [11, 12] using 2.3.4.

$$\kappa = \frac{2\Delta n \Gamma}{\lambda} \tag{2.3.4}$$

where $\Delta n = n_2 - n_1$ is the refractive index difference of the grating materials.

This process of modelling the DFB waveguide involved averaging the refractive index of the grating layer based on the ratio of each material present when taking a cross-section through the structure. This method also provides an insight into the coupling to a photonic crystal layer with an averaged refractive index. Assumptions on the fill factor of the photonic crystal are made, and as the crystal is two-dimensional, lattice structure should be taken into consideration when calculating the average index. Test patterns formed by electron

beam lithography provided an insight into the likely ratio between the two materials forming the crystal and give $n = 3.28$ as an averaged value. For the purposes of modelling void-incorporating photonic crystals in this chapter, the refractive index of the void is taken to be that of air ($n = 1$).

2.4 Waveguide structure

Figure 2.3 lists the epitaxial structure and plots schematically the refractive index of a possible waveguide for an all-semiconductor PCSEL based on that of a buried grating DFB laser previously fabricated at the University of Sheffield [16]. A buried one-dimensional grating layer was generated through a second epitaxial growth process on top of a shallow InGaP layer with an etched grating. Here, an InGaP grating and an InGaP etch stop layer are also used to avoid damage to the active region and oxidation of aluminium containing layers when the photonic crystal features are etched. The development of this regrowth process for deeper two-dimensional features is outlined in section 3.4.1.

Material	Thickness (μm)	n
$Al_{0.4}Ga_{0.6}As$	3	3.310
GaAs	0.080	3.521
InGaP/GaAs	0.150	3.275
GaAs	0.020	3.521
InGaP	0.030	3.143
GaAs	0.030	3.521
$In_{0.2}Ga_{0.8}As$	0.008	3.736
GaAs	0.020	3.521
$In_{0.2}Ga_{0.8}As$	0.008	3.736
GaAs	0.020	3.521
$In_{0.2}Ga_{0.8}As$	0.008	3.736
GaAs	0.030	3.521
$Al_xGa_{(1-x)}As$	3	2.965-3.475
GaAs substrate		

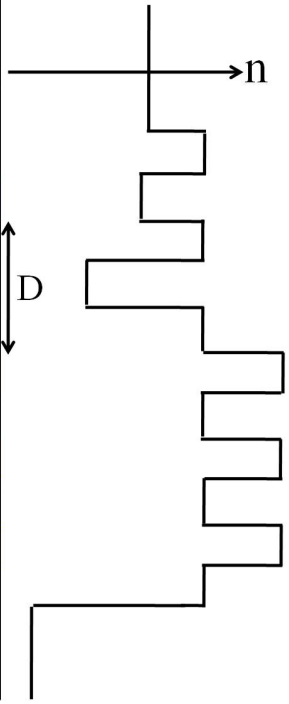

Figure 2.3: Modelled waveguide structure including epitaxial layer thicknesses, refractive indices, distance D between active (blue layers) and photonic crystal (red layer), and a schematic indicating index profile.

The refractive index (determined from material compositions and refractive index tables [17]), and the thickness of the layers in the structure is shown in figure 2.3. These parameters affect the ability of the waveguide to sustain a bound mode, and govern the proportion of the bound mode that resides in each layer (confinement factor). In addition, figure 2.3 indicates the variable D, which corresponds to the minimum distance between the top active element and the photonic crystal layer. The effect of D on photonic crystal

coupling is investigated in this chapter. The schematic indicates the refractive index (n) profile of the core of the structure. As the refractive index changes with the composition of aluminium in the top and bottom cladding layers, variable refractive indices are possible. The position of the line indicating the $Al_xGa_{(1-x)}As$ lower cladding refractive index in figure 2.3 corresponds to the lowest value of n considered. The potential refractive indices for the considered values of x in the $Al_xGa_{(1-x)}As$ lower cladding are plotted in figure 2.4.

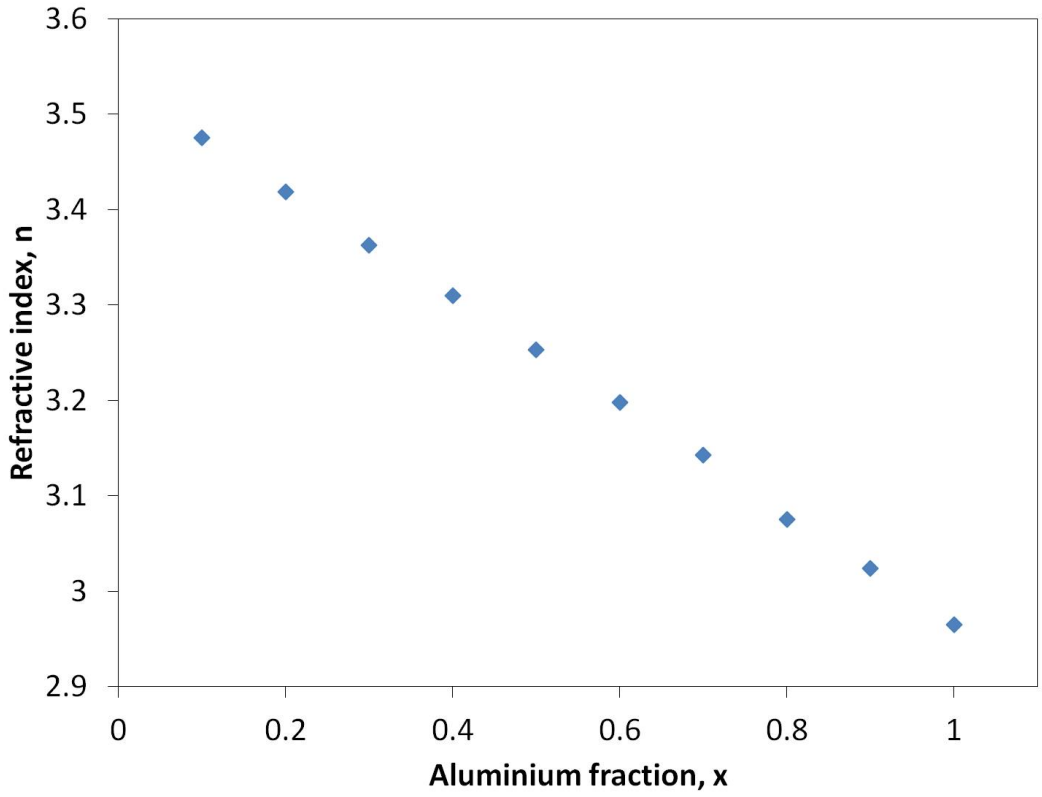

Figure 2.4: Variation of refractive index at $\lambda = 980$ nm with aluminium fraction, x in the $Al_xGa_{(1-x)}As$ lower cladding [17].

As the photonic crystal is situated above the active elements (see figure 2.3), variations in the composition of the lower cladding are investigated in the attempt to push the mode up into the top part of the waveguide structure. Whilst variations in the upper cladding aluminium composition should also distort the mode in favour of certain layers, the effects of this are not included in this chapter. This is due to the complexity of the regrowth process and the relatively easy growth of $Al_{0.4}Ga_{0.6}As$ as the upper cladding, however, further work may consider variations in this.

2.5 Structural optimisation - all-semiconductor photonic crystal

As the coupling to the photonic crystal is directly proportional to the confinement of the mode in this layer (2.3.4), an increase in the thickness of the photonic crystal layer should yield larger coupling values. However, figure 2.5 reveals that this relationship is not so simple as the increase in photonic crystal thickness also changes the parameters of the waveguide. Initially, coupling values are increased as the photonic crystal is made thicker, but at approximately 300 nm the coupling levels off, before slowly decreasing.

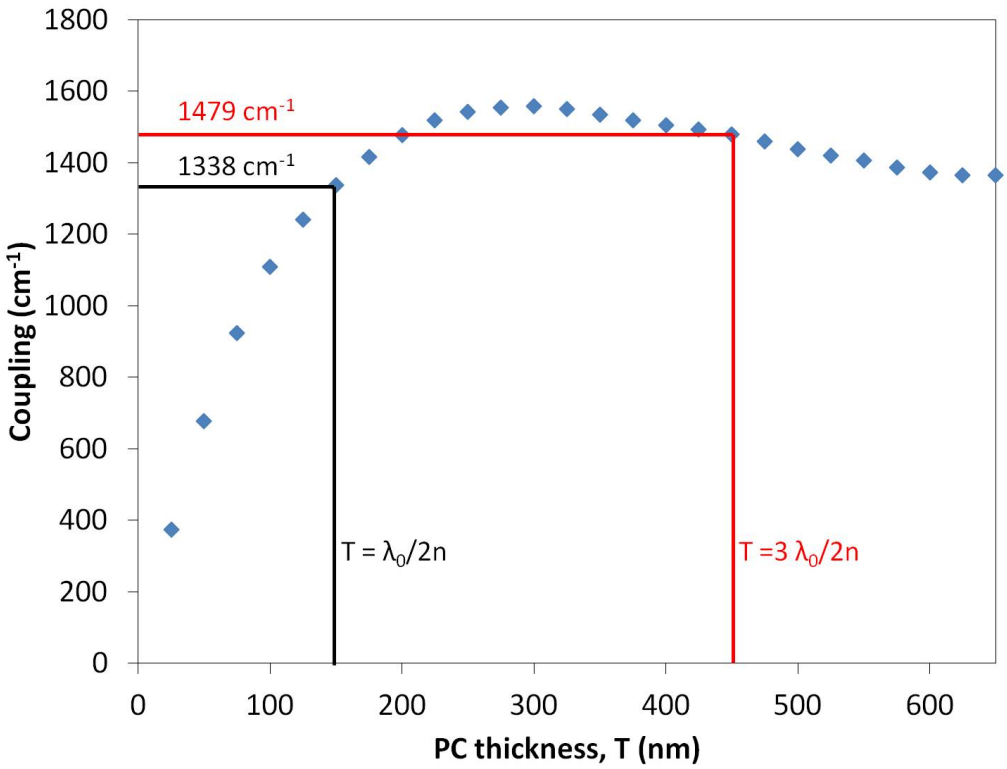

Figure 2.5: Coupling coefficient against thickness, T, of photonic crystal layer in the waveguide. Coupling values for T = $\frac{\lambda_0}{2n}$ (black) and T = $\frac{3\lambda_0}{2n}$ (red) indicated, where λ_0 is the vacuum wavelength of light and n is the refractive index.

For optimal Bragg diffraction of light out of the photonic crystal plane, this layer should have a thickness, T, so that:

$$T = \frac{(2m-1)}{2}\frac{\lambda_0}{n} \tag{2.5.1}$$

where λ_0 is the wavelength of light in a vacuum, n is the refractive index and m is a positive and real integer.

Figure 2.5 indicates that there is a 141 cm^{-1} increase in coupling between a thickness of T = 150 nm ($m = 1$), and T = 450 nm ($m = 2$). However, this small increase is mitigated by the significantly increased difficulty of regrowth on deeper features (see figure 3.11).

The optimisation of the waveguide outlined in figure 2.3 occurred in several stages. First, the profile of the mode propagating through the structure was examined to understand the effect of variations in refractive index in various layers. Figure 2.6 indicates the mode profile within the model structure with the location of the photonic crystal and the active elements (quantum wells) shown. Each of the different modes (shown in blue) in figure 2.6 correspond to a different waveguide structure using the respective refractive index of the $Al_xGa_{(1-x)}As$ lower cladding layer (as plotted in figure 2.4).

The upper cladding composition is kept constant at $Al_{0.4}Ga_{0.6}As$ as good epitaxial growth of this is known to be possible from an already established recipe [16]. For lower cladding aluminium compositions less than x = 0.3, no bound mode was found in this structure. In figures 2.6 and 2.7, the relative mode intensities are normalised against the highest intensity for that mode, for comparison between the different waveguides created by changing the cladding composition. Figure 2.6 shows the majority of the mode is confined near the centre of the structure where the photonic crystal and active elements are.

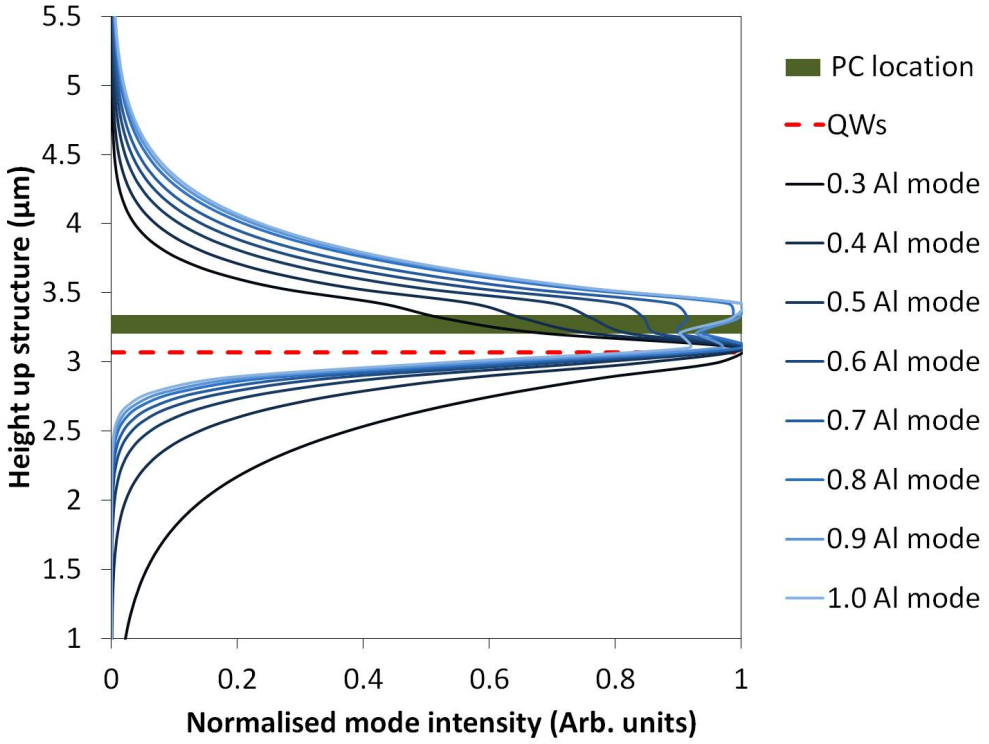

Figure 2.6: Mode profiles for varying aluminium compositions of the lower $Al_xGa_{(1-x)}As$ cladding layer with the location of photonic crystal (green) and quantum wells (red) indicated.

Closer examination of these regions indicates that there is a clear increase in mode intensity (within the photonic crystal) as the lower cladding aluminium composition is increased (see figure 2.7). Maximal mode intensity in the photonic crystal layer occurs at an aluminium composition of x = 0.8, however, there appears to be a trade-off in the mode intensity within the quantum wells at these high aluminium compositions. Layers with high aluminium compositions will also cause an undesirable increase in the resistance of the device

due to low electron mobility [18, 19]. Hence, a compromise of the parameters discussed in this chapter is required to ensure optimum device performance.

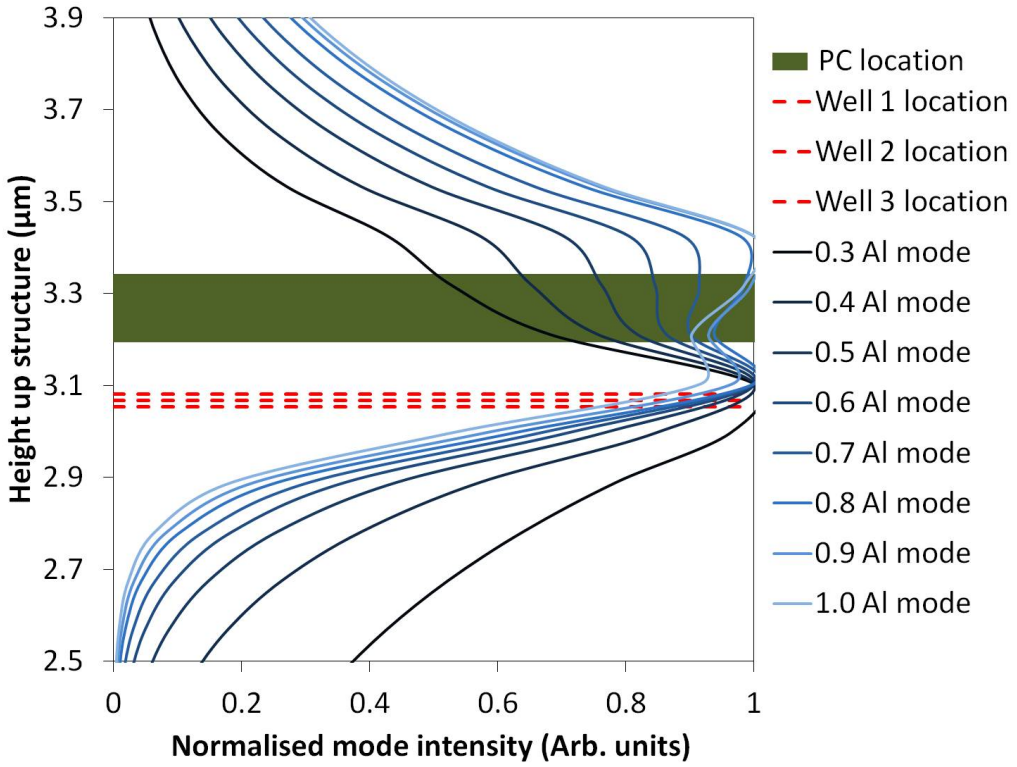

Figure 2.7: Mode profiles for varying aluminium compositions of the lower $Al_xGa_{(1-x)}As$ cladding layer in the regions surrounding the photonic crystal (green) and quantum wells (red).

Figures 2.6 and 2.7 clearly show that the variation in aluminium composition (and hence refractive index) of the lower cladding is distorting the profile of the mode in the structure. It is this redistribution of the mode that allows for optimisation of the mode present in the active and photonic crystal layers.

Figure 2.7 also provides evidence that the mode profiles are distorted by

the relatively high refractive index of the GaAs layer immediately above the photonic crystal. In an optimal design the thickness of this layer would be minimised to avoid mode distortion, however, to ensure successful infill during regrowth an epitaxial layer of the order of 100 nm is required (see chapter 3). An 80 nm GaAs layer has been modelled immediately above the photonic crystal as a minimum thickness that should still result in complete infill of the photonic crystal features. Fine control of the thickness of epitaxial layers in a semiconductor structure is possible through modern growth techniques such as metal organic vapour phase epitaxy (MOVPE) [20,21]. However, the regrowth process on features as deep as a 150 nm thick photonic crystal [22] makes control of the layer above the photonic crystal difficult as some of the material has been used to fill the features. Careful control of growth parameters can ensure that these features are successfully filled, but growth occurs both in the holes and on top of the crystal layer at the same time. As such, the overall thickness of this regrown layer is hard to judge during the process and the final result will influence the actual mode profile and the confinement factor in the photonic crystal.

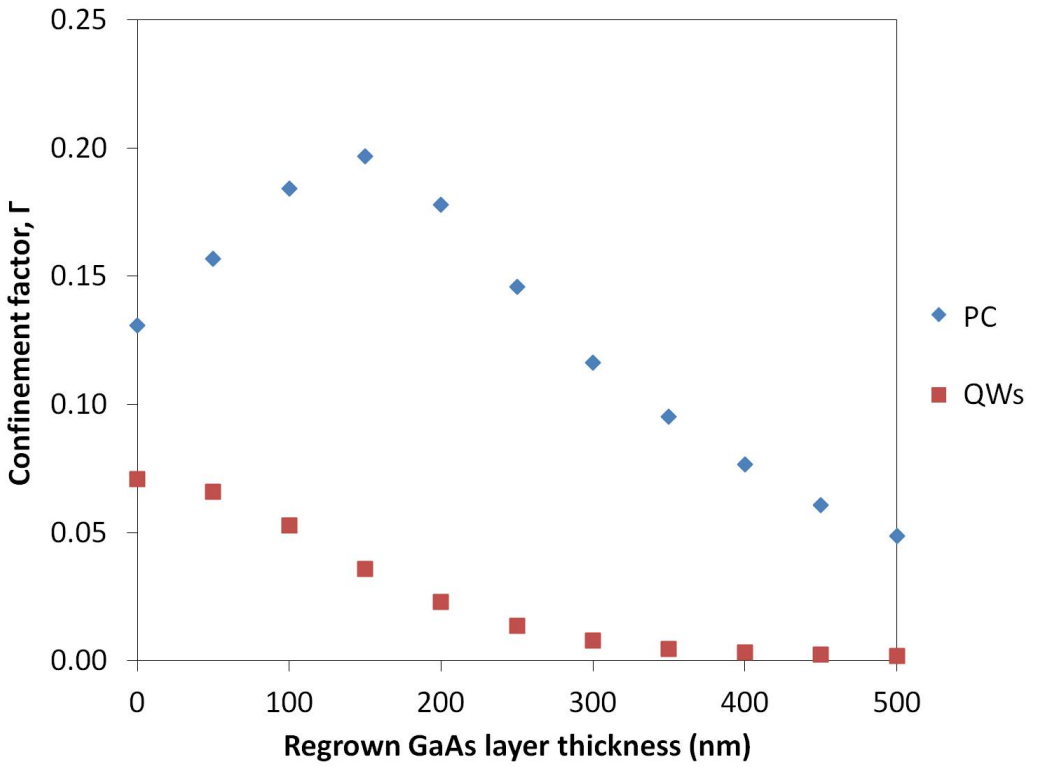

Figure 2.8: Confinement factor in photonic crystal (PC) and quantum wells (QW) as a function of GaAs regrowth layer thickness.

Figure 2.8 plots the change in confinement factor within the photonic crystal (PC) and quantum well (QW) layers, as the GaAs layer above the photonic crystal is increased in thickness. The results for a fixed lower cladding aluminium composition (x = 0.4 chosen as growth of this composition known to be possible [16]) are plotted to clarify just the effects of the GaAs layer thickness. There is a definite increase in mode confinement within the photonic crystal up to a GaAs thickness of 150 nm, after which it decreases signifi-

cantly. Perhaps more significantly, the confinement factor within the quantum wells rapidly decreases towards zero, indicating that the increased GaAs layer thickness is drawing the mode profile up into the photonic crystal and away from the quantum wells. The combination of these two effects indicates there is an optimum thickness for this layer depending on the precise structure and composition of the rest of the waveguide. However, it is the optimisation of the regrowth process that will define the optimum thickness of this layer so that complete infill of the photonic crystal features occurs.

Early research showed that a coupling coefficient of 1000 cm^{-1} is sufficient for a photonic crystal to achieve lasing [13]. Using 2.3.4 the mode confinement within the photonic crystal layer is converted into a coupling measurement, enabling comparison between possible waveguide structures and determining whether lasing will occur at the same time. The refractive indices of GaAs, n = 3.521 [14], and InGaP, n = 3.143 [15] (at $\lambda = 980$ nm), are used in equation 2.3.4 as the constituent materials of the photonic crystal.

Figure 2.9 is a plot of the coupling to the photonic crystal for various aluminium compositions in the lower cladding as a function of the distance, D, defined in figure 2.3.

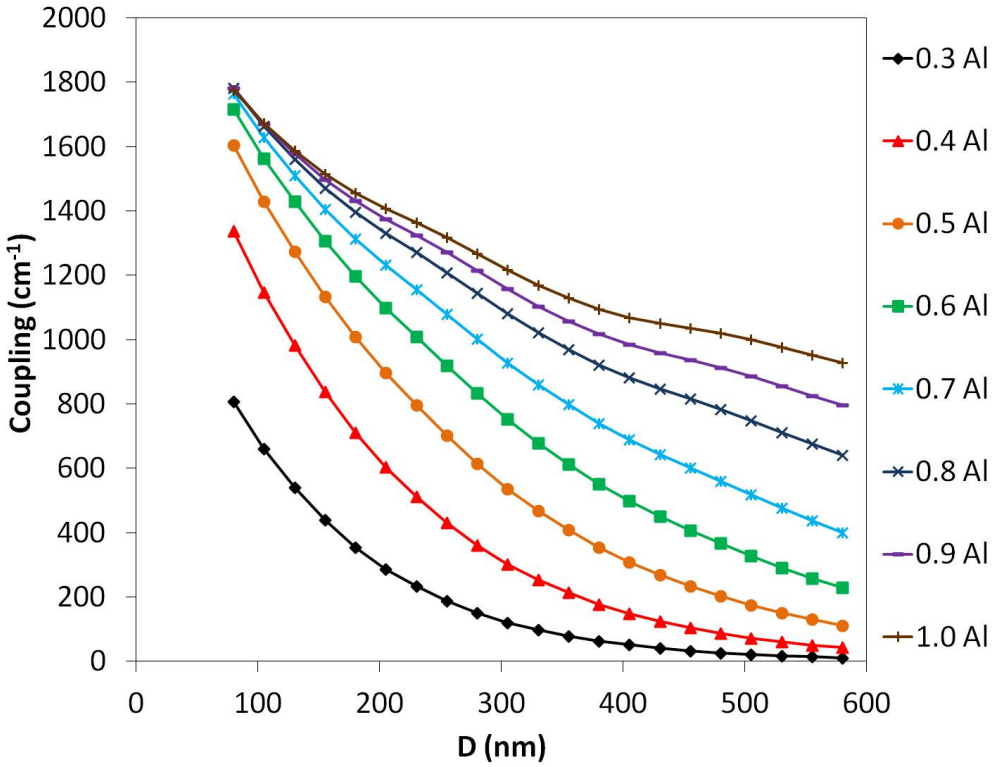

Figure 2.9: Modelled coupling as a function of D for various fractions of aluminium in the $Al_xGa_{(1-x)}As$ lower cladding.

Starting from the minimal distance of D = 80 nm (for the inclusion of etch stop and buffer layers) the coupling has been plotted out to D = 580 nm, where low aluminium composition modes have low coupling values. At this distance modes for higher aluminium composition still have relatively high coupling, but as figure 2.10 shows, the confinement in the quantum wells is significantly reduced. This means there is a trade-off between high photonic crystal coupling values and quantum well confinement factors at both high and

low values of D. At D = 80 nm, all modes apart from that with an aluminium composition of 0.3 achieve a coupling greater than 1000 cm^{-1}, which the literature indicates is sufficient. Whilst the coupling remains sufficiently high at high values of D and for high aluminium fractions in figure 2.9, increasing D sufficiently causes the coupling to drop to zero for all bound modes (but is not plotted to ensure clarity). A minimal value for D appears critical for the final waveguide to achieve high levels of coupling.

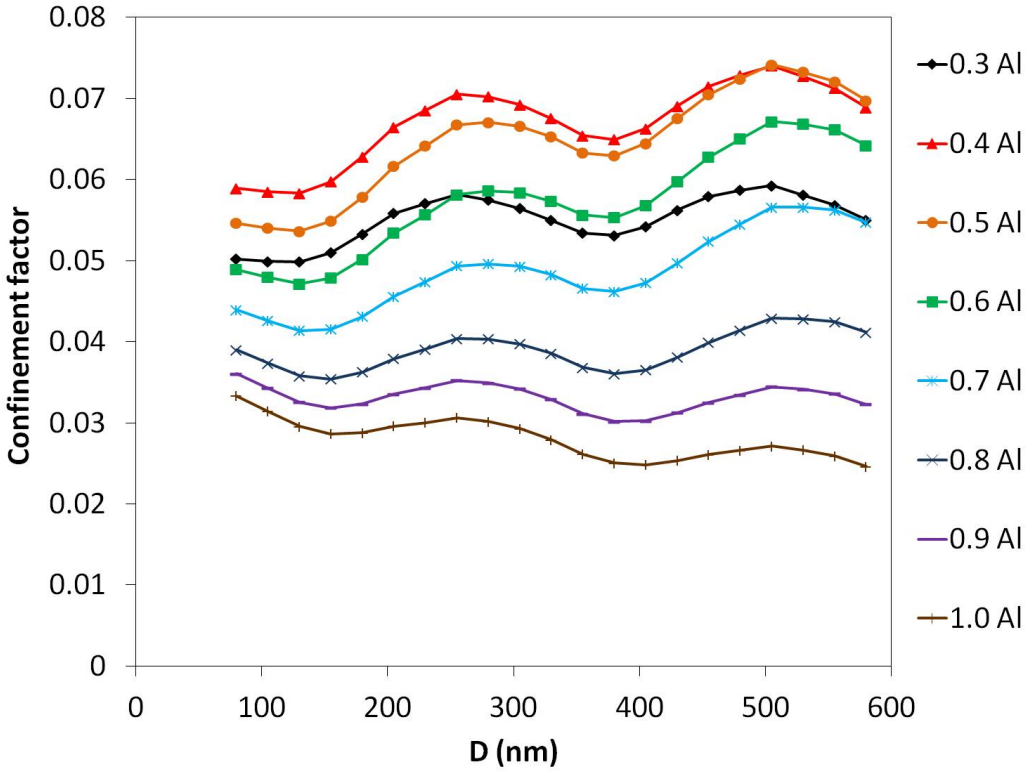

Figure 2.10: Confinement factor of the quantum wells as a function of D for various fractions of aluminium in the $Al_xGa_{(1-x)}As$ lower cladding.

Figure 2.10 is a plot of the mode confinement within the quantum well layers as a function of D for varying lower cladding aluminium compositions. A lower cladding aluminium composition of x = 0.4, for low and intermediate D values, or x = 0.5 for high D values, yields the highest confinement factor. As figure 2.9 indicates, for these aluminium compositions the coupling is highest at low D. Therefore, the optimum balance between photonic crystal coupling and quantum well confinement factor is achieved at minimal D and an aluminium composition of x = 0.4. The variation in confinement factor as D increases appears to fluctuate around a general trend; with low and intermediate aluminium fractions resulting in an overall increase; a composition of 0.8 oscillating around a constant value, and compositions higher than 0.8 resulting in an overall decrease. These fluctuations vary for each fraction of aluminium in the lower cladding, and are created as each mode is distorted by moving the photonic crystal away from the active. As the value of D is increased, the change to the refractive index of the layer structure causes the central peak of the bound mode to pass successively through each of the quantum wells. High points in the confinement factor occur when the mode peak is aligned with a quantum well, and low points occur when the mode peak is mis-aligned with a quantum well.

2.6 Introduction of a photonic crystal with voids

Waveguide modelling in this chapter has attempted to maximise the coupling to an all-semiconductor photonic crystal and provide mode overlap with the active region. However, an all-semiconductor photonic crystal has a smaller refractive index contrast than a void-semiconductor one so reduced feedback is expected, making it harder to achieve lasing. To show that an all-semiconductor photonic crystal is worth considering, this section considers the effects of replacing the infilled GaAs with voids (a lower cladding composition of 40% aluminium is used in the following modelled structures).

Figure 2.11 plots the coupling coefficient for a void-InGaP photonic crystal layer within the waveguide as a function of D. The averaged refractive index here is significantly lower than the surrounding semiconductor layers ($n = 2.39$), leading to significant mode distortion away from the photonic crystal layer. In comparison to the coupling coefficients in figure 2.9, the coupling of the void containing photonic crystal is much lower for all aluminium compositions and at all distances. This is due to the reduction in confinement factor as the low refractive index distorts the mode away from the photonic crystal layer. Figure 2.11 indicates the coupling for all bound modes, which for higher aluminium compositions only occurs at high D, with the arrows indicating when a mode becomes bound for that aluminium composition.

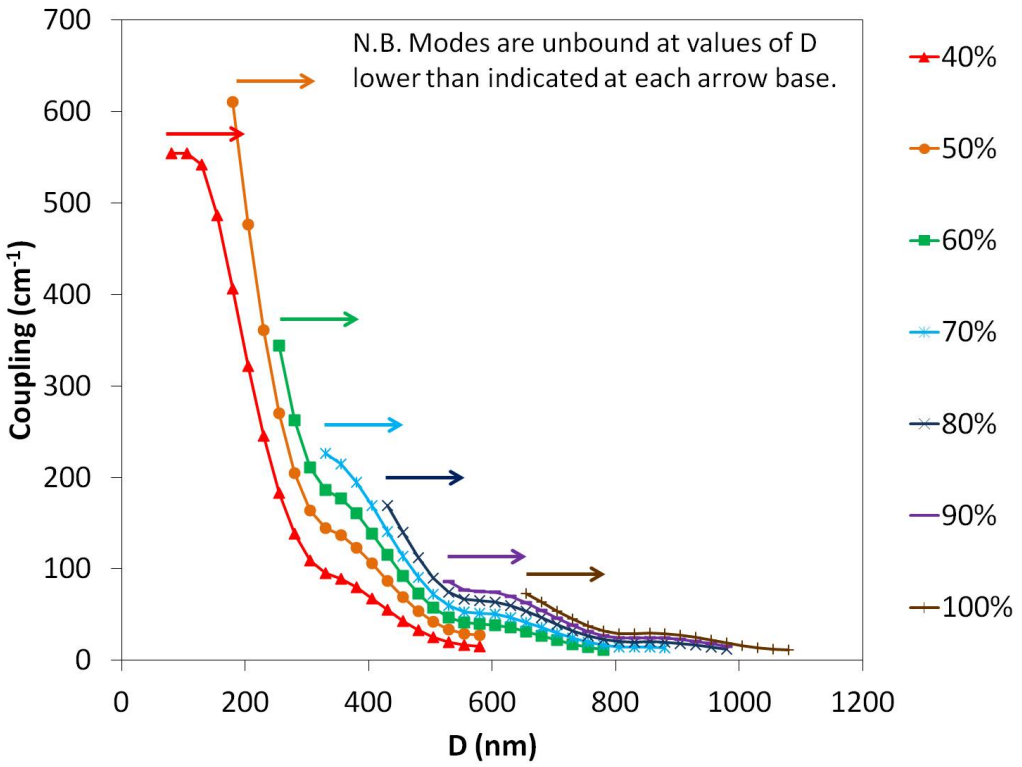

Figure 2.11: Photonic crystal coupling coefficient as a function of D for a void-incorporating photonic crystal, with varying aluminium compositions in the lower cladding. Arrows indicate the values of D for which modes become bound in each modelled structure.

As with an all-semiconductor photonic crystal the coupling drops towards zero with increasing D, however, this occurs much more rapidly for the structures modelled in figure 2.11. The difference between the mode profile of a void-InGaP PC layer and a GaAs-InGaP PC layer for this waveguide structure is shown in figures 2.12 and 2.13.

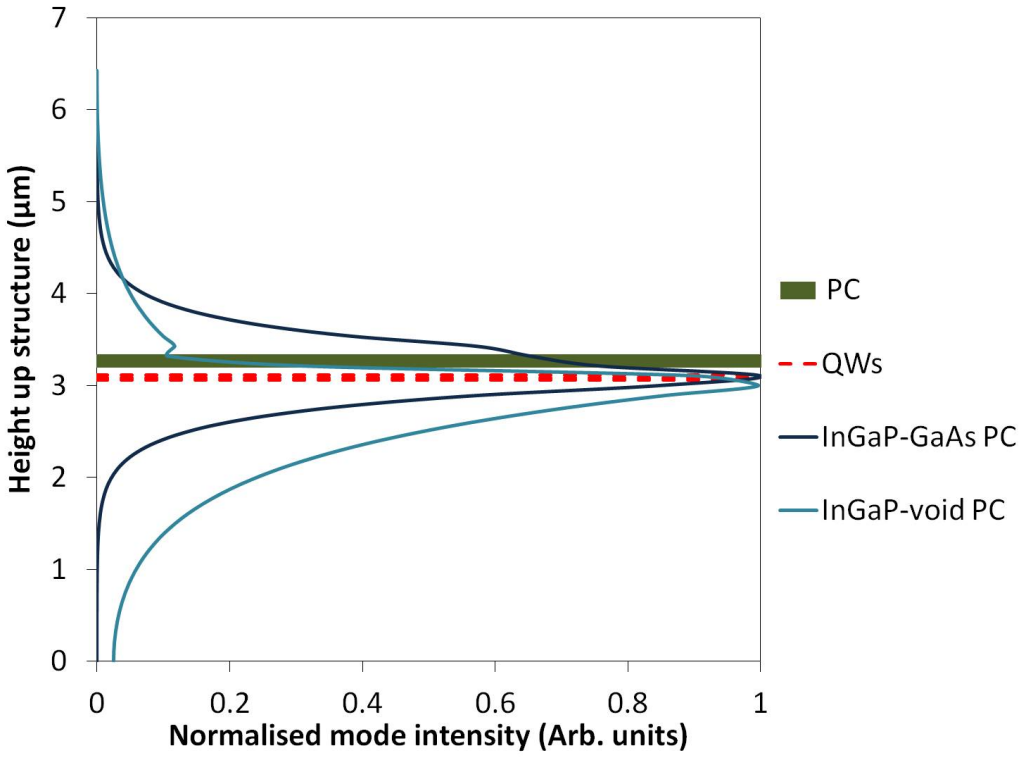

Figure 2.12: Mode profile comparison for a fixed waveguide structure including a void-incorporating photonic crystal (light blue) and an all-semiconductor photonic crystal (dark blue).

Figure 2.12 illustrates the difference between the overall mode profiles of an all-semiconductor photonic crystal layer and a void-semiconductor layer. The intensity of the mode profiles in the photonic crystal layer is significantly different for the same lower cladding aluminium composition and D.

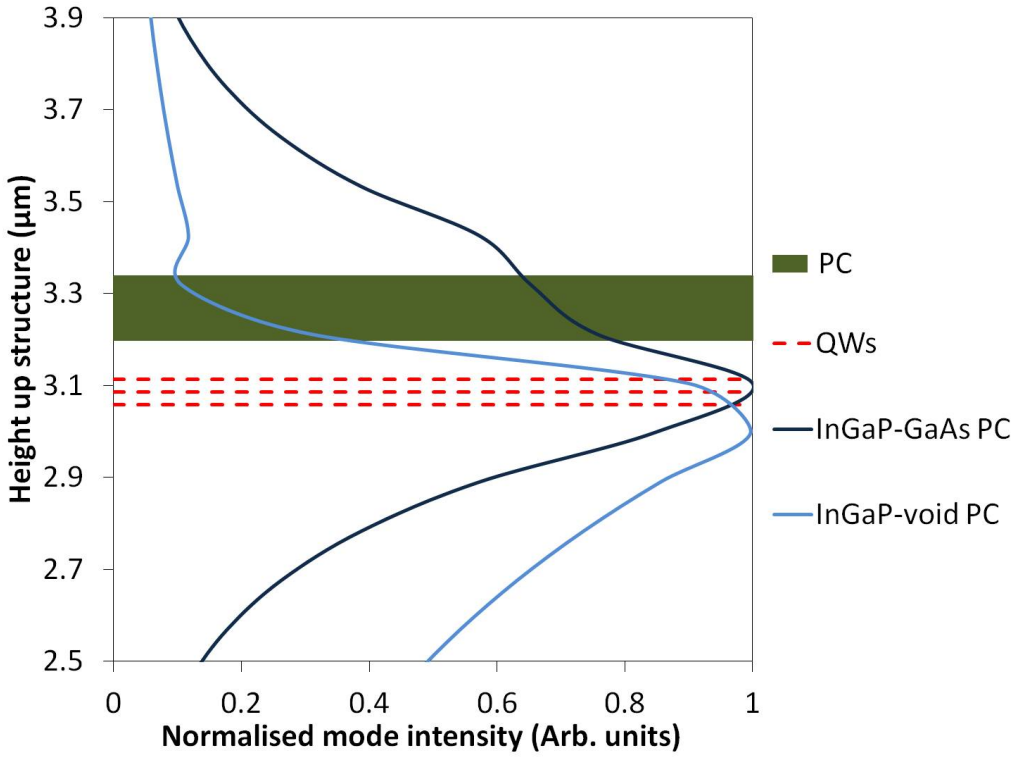

Figure 2.13: Mode profile comparison for a fixed waveguide structure including a void-incorporating photonic crystal (light blue) and all-semiconductor photonic crystal (dark blue) focussing on regions close to the quantum well (QW) and photonic crystal (PC) layers.

Close examination of the region surrounding the photonic crystal and quantum well layers indicates that the mode profile of the void-InGaP photonic crystal has been distorted (figure 2.13). In this case the peak of the mode profile has shifted into the lower cladding, and although there is still reasonable overlap with the quantum wells, the mode overlap with the photonic crystal is poor.

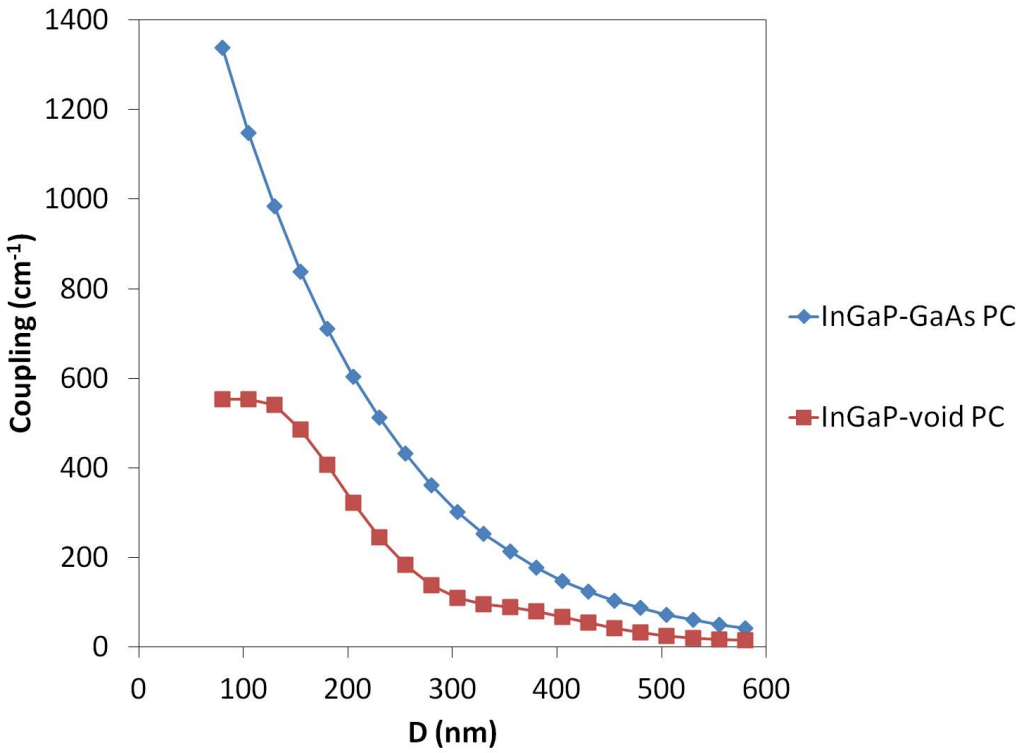

Figure 2.14: Comparison of coupling to photonic crystal achieved by an all-semiconductor (blue) and void-semiconductor (red) photonic crystal layer within the same waveguide structure.

A comparison of the coupling of the two types of photonic crystal layers considered is outlined in figure 2.14. The all-semiconductor photonic crystal achieves greater coupling at all D in this waveguide structure. Insufficient coupling is achieved, at all D, for the void-semiconductor photonic crystal to reach the limit of 1000 cm^{-1} suggested in [13]. Whilst the all-semiconductor photonic crystal clearly surpasses this value at low D (for this structure).

2.7 Conclusions

A waveguide containing an all-semiconductor photonic crystal layer will achieve greater coupling than a void-incorporating layer due to the lower effective index, created by the voids, distorting the mode away from the photonic crystal layer (assuming the voids have a refractive index of 1). Considering the extent of the research conducted into incorporating a void-semiconductor photonic crystal into a waveguide this result is initially surprising. However, in the literature this lower coupling is offset by the high feedback levels created by the high refractive index contrast between the voids and the semiconductor material of the photonic crystal. Once an all-semiconductor PCSEL is demonstrated, additional work may lead to an optimal solution between the waveguiding effects and the high refractive contrast of the void incorporating photonic crystals.

This chapter also outlined the design of a waveguide for an all-semiconductor photonic crystal, in addition to the variables that can influence coupling of the mode to the photonic crystal layer. The effects of these variables are considered for two possible photonic crystal layers, either all-semiconductor or void-semiconductor. At first glance the increase in photonic crystal thickness produced an increase in coupling due to the increased proportion of the mode in that layer. However, increasing the thickness further resulted in the coupling

to the photonic crystal reaching a maximum and then decreasing. Adjustment of the composition of the lower cladding results in distortion of the mode, pushing the mode further up towards the photonic crystal and increasing the confinement factor. High aluminium compositions reach a trade-off point between confinement in the quantum wells and the photonic crystal, however, lower aluminium compositions are likely to yield lower resistance devices due to electron mobility. Hence, an optimal structure is achieved at minimal D and an aluminium composition of x = 0.4. The thickness of the GaAs layer above the photonic crystal produces optimal coupling at 150 nm, however, reduction in the overlap with the active region indicates a compromise is required. Ultimately the optimal thickness of this layer will depend on the optimisation of the regrowth process. Increasing the distance of the photonic crystal from the active region results in reducing the coupling as the active region is near the peak of the bound mode. At higher D the mode is decaying exponentially, so less of the mode resides within the photonic crystal layer.

References

[1] "Coherent two-dimensional lasing action in surface-emitting laser with triangular-lattice photonic crystal structure" M. Imada, S. Noda, A. Chutinan, T. Tokuda, M. Murata and G. Sasaki. Appl. Phys. Lett., **75**, No. 3, 316 (1999)

[2] "Multidirectionally distributed feedback photonic crystal lasers" M. Imada, A. Chutinan, S. Noda and M. Mochizuki. Phys. Rev. B, **65**, 195306 (2002)

[3] "Polrization mode control of two-dimensional photonic crystal laser by unit cell structure design" S. Noda, M. Yokoyama, M. Imada, A. Chutinan and M. Mochizuki. Science, **293**, 1123 (2001)

[4] "Semiconductor lasers with one- and two-dimensional air/semiconductor gratings embedded by wafer fusion technique" M. Imada, S. Noda, A. Chutinan, M. Murata and G. Sasaki. IEEE J. Sel. Topics Quant. Electron., **5**, No. 3, 658 (1999)

[5] "Laser diode incorporating buried etched-void photonic pattern" D. Gazula, S. Quadery and D. G. Deppe. Electron. Lett., **41**, No. 22 (2005)

[6] "Lasing band-edge identification for a surface-emitting photonic crystal laser" K. Sakai, E. Miyai, T. Sakaguchi, D. Ohnishi, T. Okano and S. Noda. J. Sel. Areas Commun., **23**, No. 7, 1335 (2005)

[7] "Optical Electronics in Modern Communications" p492, Fifth Edition, Oxford University Press (1997) Amnon Yariv

[8] Fimmwave by Photon Design, wwww.photond.com

[9] "Problems in vector mode calculations for dielectric waveguides" A. Sudbo. Proc. SPIE 2212, Linear and Nonlinear Integrated Optics, 26 (1994)

[10] "Film mode matching: a versatile numerical method for vector mode field calculations in dielectric waveguides" A. Sudbo. Pure Appl. Opt. **2** 211 (1993)

[11] "Advanced Gallium Arsenide Based Lasers" PhD Thesis by B. J. Stevens, University of Sheffield (2009)

[12] "Optical Semiconductor Devices" Wiley (1999) Mitsuo Fukuda

[13] "Room temperature continuous wave operation of a surface emitting two dimensional photonic crystal laser" D. Ohnishi, T. Okano, M. Imada and S. Noda. Optics Express, **12**, No. 8, 1562 (2004)

[14] http://www.batop.com/information/n_GaAs.html

[15] http://refractiveindex.info/?group=CRYSTALS&material=AlGaInP

[16] "Distributed feedback laser employing buried GaAs/InGaP index-coupled grating" B. J. Stevens, K. M. Groom, J. S. Roberts, P. W. Fry, D. T. D. Childs and R. A. Hogg. Electron. Lett., **46**, No. 15 (2010)

[17] http://www.batop.com/information/n_AlGaAs.html

[18] "Properties of Aluminium Gallium Arsenide" p167, IEE emis datareviews series No. 7, INSPEC (1993) S. Adachi

[19] "MOCVD regrowth over GaAs/AlGaAs gratings for high power long-lived InGaAs/AlGaAs lasers" P. K. York, J. C. Connolly, N. A. Hughes, T. J. Zamerowski, J. H. Abeles, J. B. Kirk, J. T. Kirk, J. T. McGinn and K. B Murphy. Journal of Crystal Growth, **124**, 709 (1992)

[20] "MOVPE for InP-based optoelectronic device application" I. Gyuro. III-Vs Review, **9**, Iss. 2, 30 (1996)

[21] "Large scale manufacturing of compound semiconductors by MOVPE" A. G. Thompson, R. A. Stall, W. Kroll, E. Armour, C. Beckham, P. Zawadzki, L. Aina, and K. Siepel. Journal of Crystal Growth, **170**, 92 (1996)

[22] "Epitaxially regrown GaAs based photonic crystal surface emitting laser" D. M. Williams, K. M. Groom, B. J. Stevens, D. T. D. Childs, R. J. E. Taylor, S. Khamas, R. A. Hogg, N. Ikeda and Y. Sugimoto. Photon. Tech. Lett., **24**, No. 11, 966 (2012)

3 Fabrication and Processing

3.1 Introduction

In this chapter the development of growth and fabrication of an all semiconductor photonic crystal surface emitting laser (PCSEL) is discussed. The growth and fabrication of a PCSEL can be split into several stages: initial growth, photonic crystal patterning, photonic crystal etching, epitaxial regrowth, and device processing. First, relevant fabrication processes are explained, secondly, the recipe for successfully generating an electrically pumped, all semiconductor PCSEL is outlined [1], and finally, additional details considered in the development of various processing stages are discussed. In particular, laser interference lithography as a patterning technique is considered. This is important in reducing the cost of each device, as the long write times and high cost of ownership of electron beam lithography contribute significantly to overall cost.

The structure grown in this chapter is based on conclusions from the modelling in chapter 2. The value of D is kept to a minimal value, and a lower cladding of $Al_{0.4}Ga_{0.6}As$ is used to achieve a balance between coupling and mode overlap with the quantum wells. For a one-dimensional grating device such as a DFB, the product of the coupling, κ, and the device length, L is

of importance. For non-phase shifted gratings $\kappa L = 1$, or for phase shifted gratings $\kappa L = 2$. From the coupling value for the structure in chapter 2 (1338 cm^{-1}), this would suggest a device length of only 7.5 μm or 15μm is required.

However, this is a small mesa to fabricate and as these devices are intended to be surface emitters an aperture is also required. For this reason the proof of concept devices described in this chapter are slightly larger, with a 50 μm diameter mesa and an aperture of 25 μm. To ensure that there is still sufficient feedback in the photonic crystal and to avoid any unwanted boundary effects the patterned area will be significantly larger than the mesa at 150 μm^2.

Specific acknowledegments to those who contributed to the successful fabrication techniques in this part of the thesis include: Naoki Ikeda and Yoshimasa Sugimoto of the National Institute for Materials Science (NIMS) in Japan for the photonic crystal definition by electron beam lithography; Kris Groom of the University of Sheffield for HF acid etching; Ben Stevens of the University of Sheffield for the MOVPE and regrowth development; and Qi Jiang of the University of Sheffield for device processing.

3.2 Background

The regrowth process using metal organic vapour phase epitaxy (MOVPE) is the critical step in the fabrication of this all-semiconductor photonic crystal

surface emitting laser. A second epitaxial process which occurs after the photonic crystal patterning, regrowth utilises the fine control of V-III ratio and growth rate in MOVPE to infill the high aspect ratio photonic crystal features. MOVPE is then also used to complete the epitaxial structure. Key to the design of the $\lambda = 980$ nm structure outlined in this thesis is the use of AlGaAs in the waveguide cladding layers. However, the exposure of these layers to air will result in aluminium oxide layers that prevent good epitaxial growth and introduce crystal defects which propagate throughout the structure. The regrowth process ensures that only selective layers are exposed during patterning and etching, thereby limiting oxide formation.

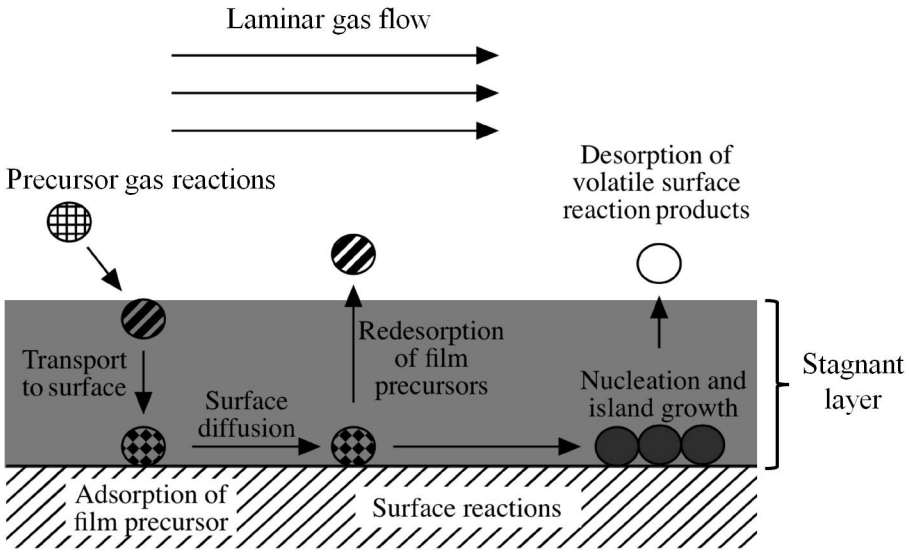

Figure 3.1: Schematic of key steps in chemical vapour deposition for epitaxial growth. *Adapted from* [11].

Figure 3.1 outlines the processes involved in chemical vapour deposition - the key to how a MOVPE reactor is used to grow complex, mulitlayered semiconductor structures, just one example of which is PCSELs. Precursor gases of high purity levels are injected into the heated reactor chamber in a laminar gas flow, where initial reactions occur. The precursors then diffuse through a stagnant layer close to the substrate and form the desired atoms on the substrate surface. Surface diffusion occurs so that deposited material nucleates and forms regions of island growths where group III and V atoms associate. Waste by-products are released from the surface as these growth sites form. Figure 3.2 is an example of how InP is grown using MOVPE. Precursor gas 1 is tri-methyl indium and precursor gas 2 is phosphine, resulting in InP deposition and the waste by-product methane. For growth of other III-V semiconductors different precursor gases are used which results in various by-products.

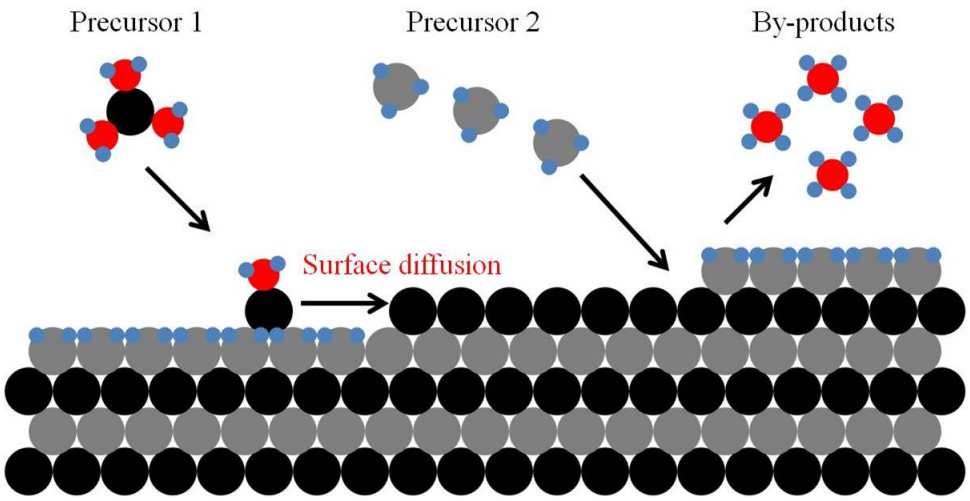

Figure 3.2: Schematic indicating key ingredients and features of MOVPE growth of InP.

Figure 3.3 is a picture of the type of close-coupled shower head MOVPE reactor chamber used for growth and regrowth processes described in this thesis. It outlines the main features of the reactor chamber, in particular, where the precursor gases enter the chamber and the location of the silicon carbide substrate holder. The 3-zone heater is used in combination with the water cooling system surrounding the chamber, giving fine control of the growth temperature.

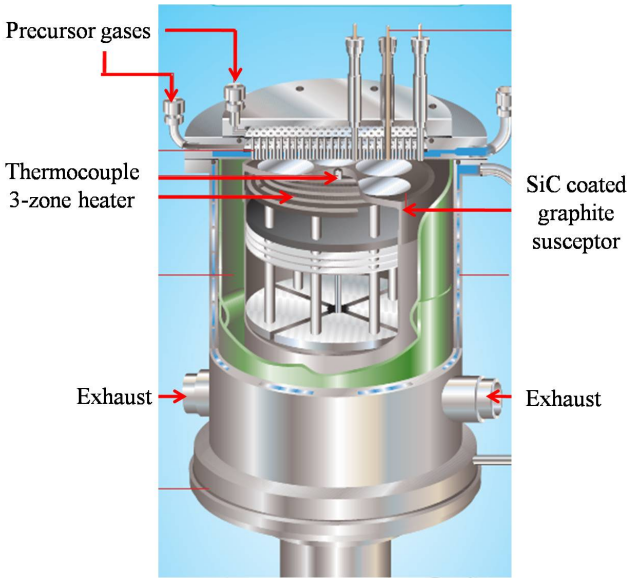

Figure 3.3: Close-coupled shower head MOVPE reactor chamber. *Adapted from* [12].

Other important steps in the fabrication process of PCSELs includes plasma enhanced chemical vapour deposition (PECVD), electron beam lithography (EBL), reactive ion etching (RIE), and inductively coupled plasma (ICP) etching. PECVD is used for depositing silicon oxide and silicon nitride layers for carrier confinement within semiconductor structures such as in this thesis.

EBL is an advanced lithography technique which uses electrons that are focussed into a high-energy beam to expose specific resists such as poly(methyl methacrylate) (PMMA). The ability of EBL to produce features with a resolution smaller than the wavelength of light means it is often used to generate patterns in resist on the nanometre scale [16,17]. Reactive ion etching is a type

of etching typically used to generate features within semiconductor, oxide or nitride layers. An electric potential is created across the chamber which contains a plasma (consisting of various substances) that is then ionised. These ions are chosen such that they are highly reactive with certain substances on the structure surface, enabling them to etch away exposed areas. Reflectivity measurements of an incident laser beam provides *in-situ* characterisation of the etch depth through comparison with computer modelling (figure 3.4).

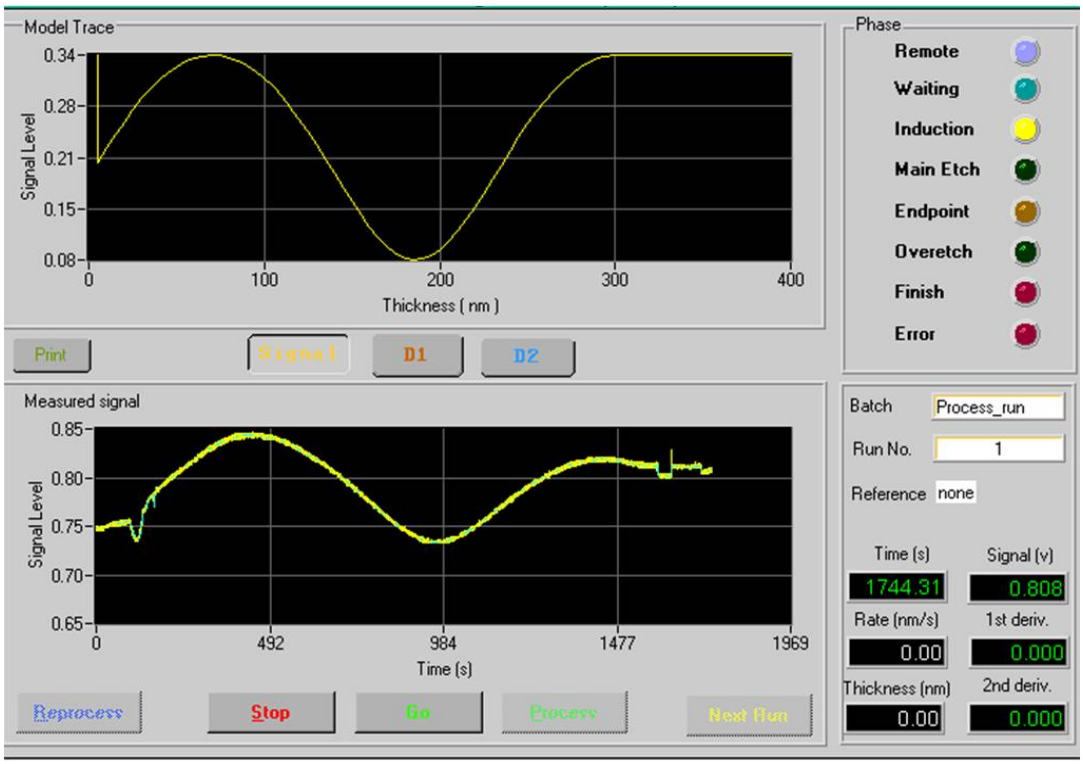

Figure 3.4: Top: Modelled trace of reflectivity against SiO_2 layer thickness. Bottom: *In-situ* reflectivity measurements whilst etching 300 nm of SiO_2.

Figure 3.4 is a plot of both the modelled trace (top) and the actual variation (bottom) in reflectivity of the incident laser beam during an etch process. The process modelled is for CHF_3 reactive ion etching through 300 nm of SiO_2 on top of a GaAs substrate. There is a clear similarity between the curves, with a few localised inconsistencies at the start and end of the measured curve. Those at the start correspond to optimisation of the laser alignment on the sample, and those at the end correspond to purging of the chamber prior to unloading. ICP etching is similar to RIE, but a magnetic field is also created within the etch chamber. This is used to force the reactive ions down towards the sample surface with significant energy, promoting a faster etching rate in the vertical direction. ICP etching is more versatile, with an additional degree of control compared to RIE as both the plasma density and the accelerating voltage are individually controlled.

3.3 Successful regrowth process

Figure 3.5 indicates the sample structure throughout each of the steps involved in the regrowth process. Figure 3.5a) shows the initial growth, whilst figures 3.5b) and c) indicate the deposition of silicon oxide and resist ready for pattern transfer into the sample (figures 3.5d)-f)). Figure 3.5g) shows the sample immediately prior to regrowth and figure 3.5h) indicates the structure following

successful regrowth. These steps are described in more detail in sections 3.3.1-3.3.3.

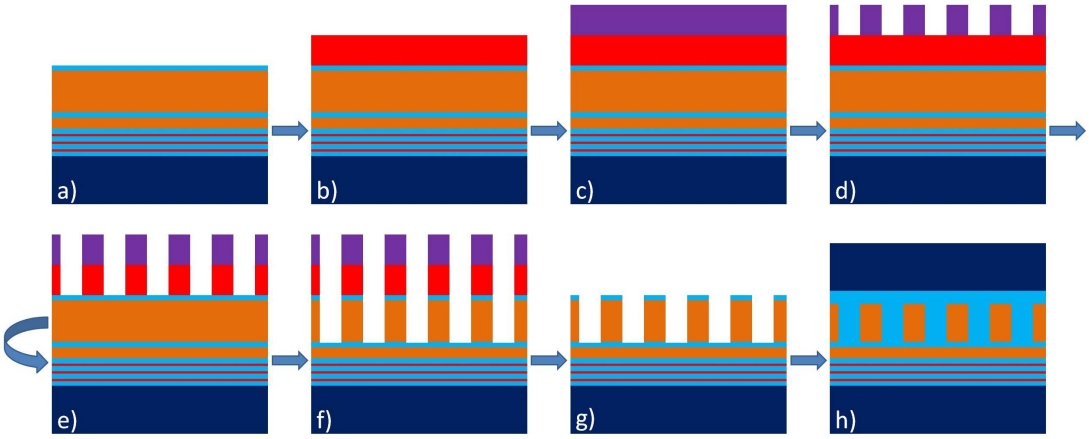

Figure 3.5: Flowchart indicating the sample structure after: a) initial growth b) oxide deposition c) resist deposition d) patterning e) oxide etching f) semiconductor etching g) HF acid clean h) successful regrowth.

3.3.1 Initial growth

Initial MOVPE growth occurred on a GaAs substrate, miscut 10° off towards the (110) direction. Initial growth included (figure 3.6): a lower cladding layer of 1.5 μm of n-$Al_{0.4}Ga_{0.6}As$; an active region of three, 8 nm $In_{0.2}Ga_{0.8}As$ quantum wells with 20 nm GaAs barriers between each; a 40 nm p-$In_{0.48}Ga_{0.52}P$ etch stop and a 20 nm p-GaAs buffer layer, ensuring etching of the photonic crystal didnt penetrate the active region; a 150 nm layer of p-$In_{0.48}Ga_{0.52}P$, to form part of the photonic crystal, and a 20 nm p-GaAs terminating layer.

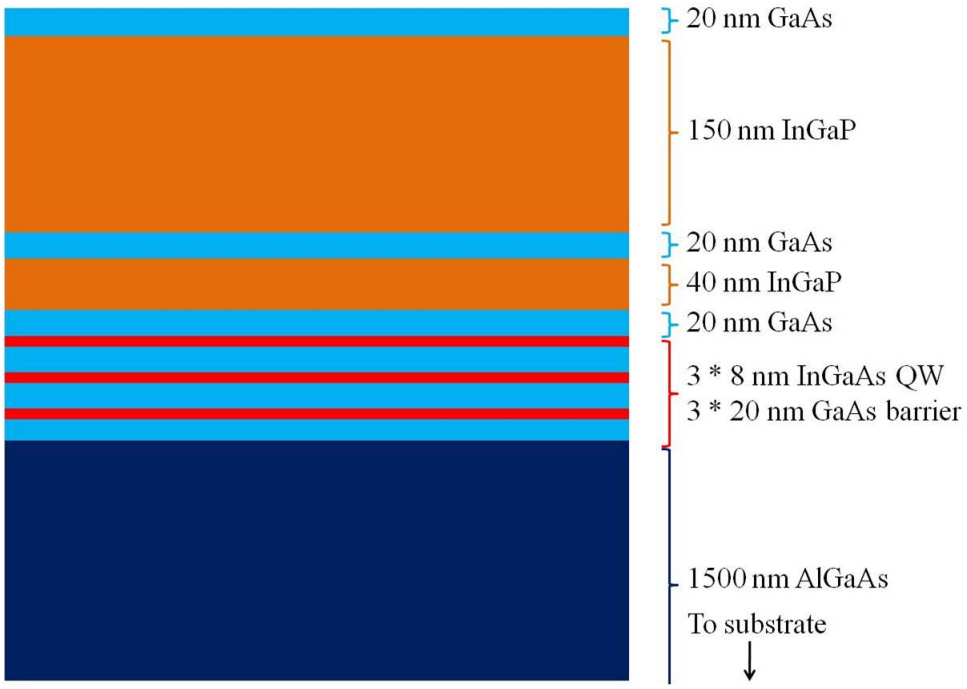

Figure 3.6: Schematic indicating the structure after the initial epitaxial growth.

3.3.2 Photonic crystal definition

Following initial growth, deposition of 300 nm of SiO_2 by PECVD occurs to create a hard mask for pattern transference into the 150 nm p-$In_{0.48}Ga_{0.52}P$ layer. ZEP-520 high-resolution, positive resist is spun onto the oxide before patterning photonic crystals using EBL. A square lattice with a circular atom shape was chosen for ease of fabrication. In addition, this is a well researched photonic crystal structure which provides easy comparison of the results in chapters 4 and 5 with void-incorporating PCSELs in the literature.

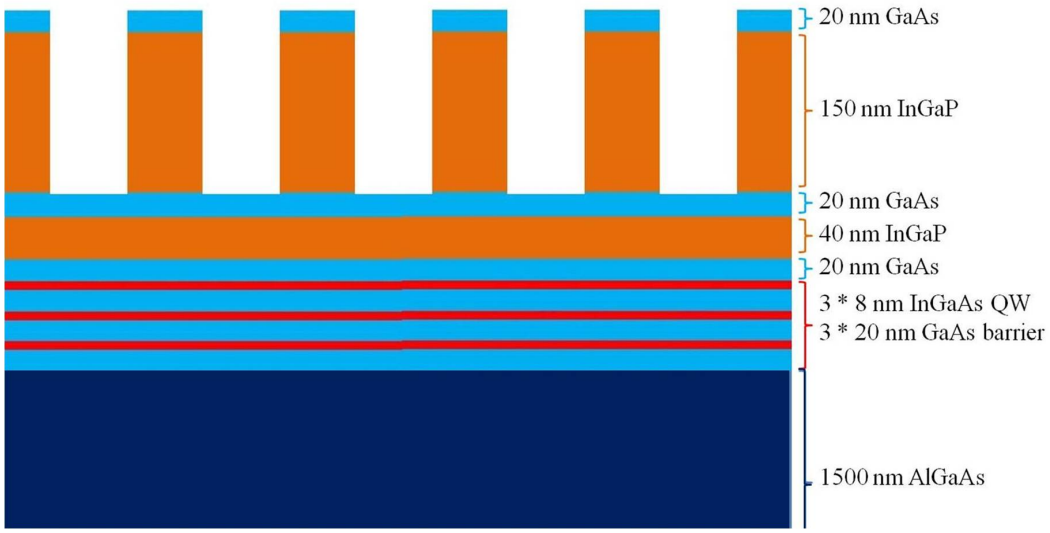

Figure 3.7: Schematic indicating the structure immediately prior to regrowth.

Reactive ion etching of the resist, using CHF_3 chemistry at room temperature, produces a hard mask with the desired photonic crystal pattern. Dry etching with an ICP mixture of argon and chlorine at 200 °C transfers the pattern defined in the hard mask into the 150 nm p-$In_{0.48}Ga_{0.52}P$ layer. At this stage the sample is given a clean in 1% buffered hydrofluoric acid solution to remove the oxide mask and any other contaminants that may be present. Figure 3.7 outlines the structure following the HF acid clean and immediately prior to regrowth.

3.3.3 Regrowth step

Regrowth was conducted in a Thomas Swan, 6 x 2" close-coupled shower head, MOVPE reactor (figure 3.3). The wafer is heated to 630 °C whilst under an arsenic overpressure to remove any oxidised material. Subsequently the wafer is cooled slightly, with growth occurring at a temperature of approximately 605 °C. Growth occurs at this temperature to achieve a balance between surface cleaning and the minimal interchange of arsenic and phosphorous. A high surface mobility is required due to the nature of the photonic crystal features. A photonic crystal with a small period, ($265nm \leq a \leq 297nm$) and a relatively thick layer (a/2) is defined as in [1, 13–15]. Infill of the photonic crystal is ensured by using a low V-III ratio in the regrowth process. The regrowth sequence consists of: 150 nm p-GaAs to infill the etched features (GaAs growth starting with a V-III ratio of 20); 1.5 μm p-$Al_{0.4}Ga_{0.6}As$ (with a V-III ratio of 120) which forms the upper cladding, and 200 nm p+GaAs. Successful regrowth can be seen in figure 3.8, which is a transmission electron microscope (TEM) image of the photonic crystal and quantum well regions of a device. The p-GaAs used to infill the photonic crystal in the regrowth results in a layer of approximately 80-100 nm of GaAs above it. This is visible in figure 3.8 and has a non-planar interface with the p-$Al_{0.4}Ga_{0.6}As$ above it. Infill of the photonic crystal features only requires part of the GaAs deposited, but

the regrowth partially transfers the pattern in the p-$In_{0.48}Ga_{0.52}P$ surface into this layer. This does not prevent the p-$Al_{0.4}Ga_{0.6}As$ from achieving a planar surface at the top of the device.

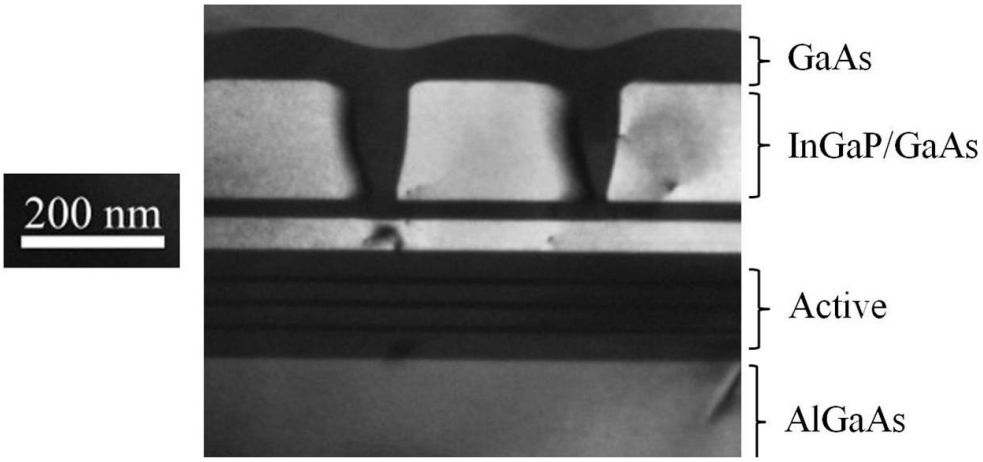

Figure 3.8: Transmission electron microscope image showing void free regrowth in the region of the photonic crystal.

3.3.4 Device processing

Figure 3.9 is a photograph of a partially processed device, formed over the centre of the patterned and regrown regions of the wafer by etching a 50 μm diameter mesa in the p+GaAs contact layer. A 50 μm annular gold contact is formed on top of this by photolithography, with deposition occurring in an evaporator and lift-off by acetone.

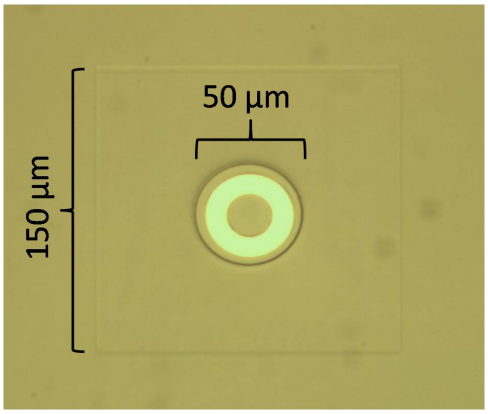

Figure 3.9: Photograph of a partially processed device - a 50 μm diameter mesa with annular gold contact located above the centre of the 150 μm square photonic crystal.

A current confinement layer of SiN is then deposited by PECVD across the whole wafer. A further photolithographic step is used to etch the SiN layer only in the region of the device top contacts, thereby allowing current injection. A 250 μm by 100 μm gold bond-pad is also deposited on top of the SiN layer. At the centre of the mesa a 25 μm aperture remained free of gold for light to escape. As reported in [1], the photonic crystal pattern in this design (150 μm by 150 μm) is significantly larger than the electrically pumped area (50 μm diameter mesa plus current spreading). This is also evident from figure 3.9 where the circular mesa occupies a small fraction of the square photonic crystal.

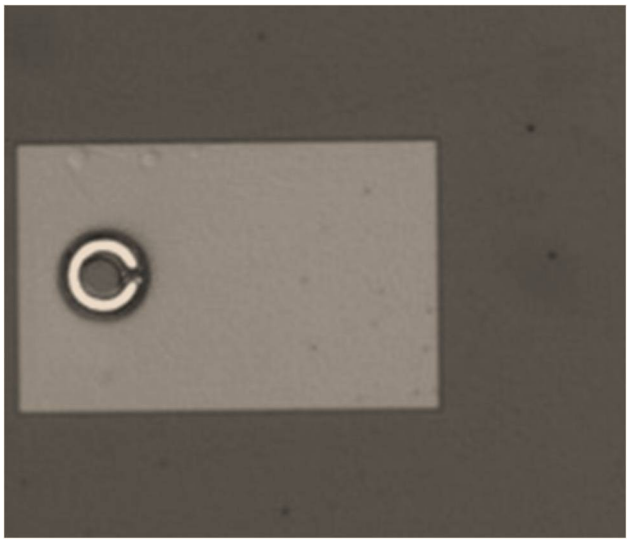

Figure 3.10: Photograph of a device after processing.

Figure 3.10 is a photograph of a processed device under a microscope. The mesa and aperture are visible on the left hand side of the device, with the bond-pad extending over a much larger region to the right. The bond-pad eases current injection by providing a significantly larger area than the mesa contact, thereby allowing the easy application of a probe needle.

3.4 Design discussions and modifications

Each of the processes outlined above required a certain amount of development and optimisation to achieve a successful regrown device. This section describes some of the design considerations and modifications undertaken in the processing of devices as described above, and reported in [1, 13–15]. The

various processes discussed in this next section include; the regrowth conditions; the photonic crystal patterning method, and the semiconductor etch recipe.

3.4.1 Regrowth development

A successful regrowth process was developed in three key steps. Figure 3.11 is a collection of TEM images showing the region of the regrown photonic crystal.

In figure 3.11a) the photonic crystal layer is 300 nm thick and inital growth occurred on a GaAs substrate miscut 3° off the (110) crystal direction. This dark-field TEM image clearly shows the presence of voids within the photonic crystal layer as bright white elliptical regions. Closer inspection of the voids reveals they are faceted and this sample is similar to those generated using the AROG method in [9]. Figure 3.11b) is a bright-field TEM image of the second development step, where initial growth occurred on a GaAs substrate miscut 10° off the (110) crystal direction. By increasing the V-III ratio the presence of voids in the photonic crystal layer is diminished as gallium diffusion into the features is promoted. In general, the voids are now located towards the top of the photonic crystal layer in a teardrop shape.

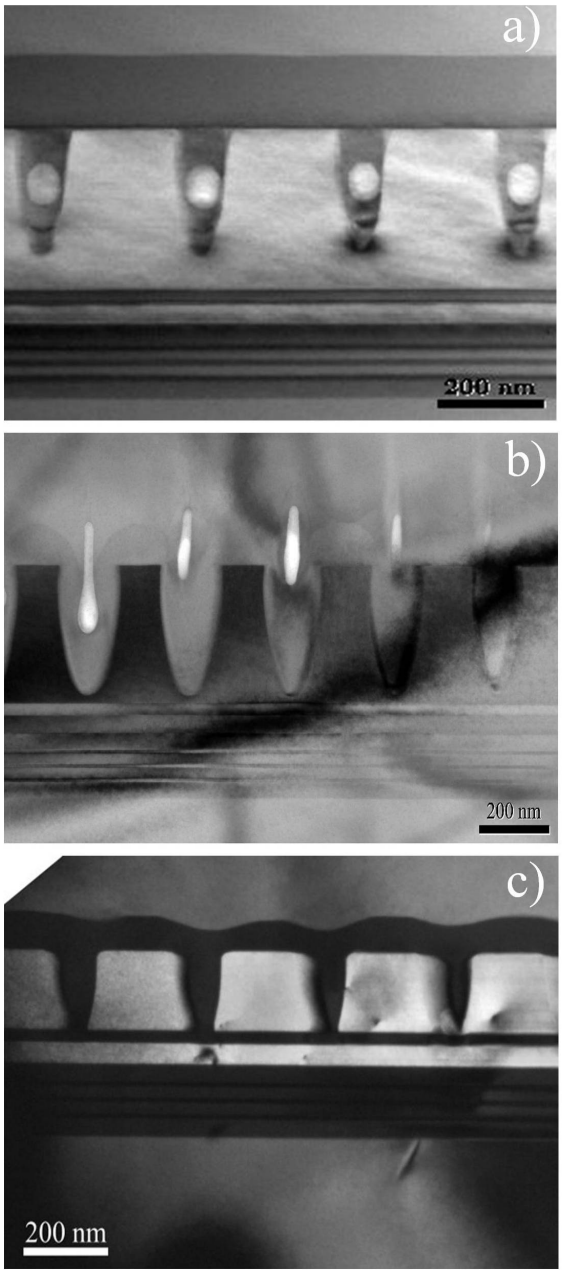

Figure 3.11: Transmission electron microscope images of three stages in regrowth development. a) Initial attempt with faceted voids. b) Increased V-III ratio with teardrop shaped voids. c) Successful void-free regrowth.

Figure 3.11c) is a dark-field TEM image showing the successful regrowth process described earlier in this chapter. In this case the initial growth also occurred on a GaAs substrate 10° off (110) and the regrowth process is the same as in figure 3.11b), but the thickness of the photonic crystal layer has been reduced from 300 nm to 150 nm. In comparison to the previous regrowths in figures 3.11a) and 3.11b), the lack of voids in figure 3.11c) indicates a successful regrowth process. However, the GaAs layer immediately above the photonic crystal pattern is clearly not planarised. Close inspection of figure 3.11b) indicates that the GaAs regrowth layer (faint grey layer) is also non-planar. This suggests that either the substrate mis-orientation or increased V-III ratio is responsible for the formation of this non-planar layer. From these TEM images it is not clear if this is a feature in both of the two dimensions of the photonic crystal, but determination of these features is an example of necessary future work in the ongoing development of this process.

3.4.2 Patterning alternatives

Whilst the literature suggests that EBL is the tried and tested method for successfully patterning photonic crystals [2–6, 18–20], alternative possibilities do exist [21–29]. The main limitation of EBL is the amount of time required to pattern complicated structures such as photonic crystals on very expensive

equipment. Additional problems include high set-up costs, maintenance difficulties, and stitch errors [30]. Other techniques include nano-imprint lithography [21–23], laser interference lithography [24, 25], focussed ion beam (FIB) milling [26, 27], and auto-cloning techniques [28, 29].

Nano-imprint technologies can be used to transfer patterns to large areas in a relatively short time, however, they require the fabrication of a robust initial mask that can be costly. FIB milling involves drilling the pattern directly into the desired surface using a focused beam of ions in a slow and costly process. Laser interference lithography (LIL) is a patterning method that can produce relatively large areas (approximately 1 cm^2) in a short time.

LIL utilises the interference pattern generated by two or more coherent lasers beams when recombined on the sample surface. This interference pattern, with relatively high and low intensity regions, can be used to transfer various patterns into the required material depending on the initial beam intensities and orientations. For control of the resultant interference pattern, a LIL set-up must be able to control the parameters that 3.4.1 indicates influence the electric field [31]. This describes the electric field vector (E) corresponding to a superposition of N laser beams, where A is the amplitude, p is the unit polarization vector, k is the wave number, n is the propagation direction unit vector, r is the position vector, f is the frequency and ϕ is the phase constant.

$$E = \sum_{m=1}^{N} E_m = \sum_{m=1}^{N} A_m p_m cos(kn_m r \pm 2\pi ft + \phi_m) \tag{3.4.1}$$

Collaborative research with the Centro de Estudios e Investigaciones Tecnicas (CEIT) on the use of LIL in photonic crystal patterning is discussed here. Figure 3.12 illustrates the fundamentals of the experimental set-up at CEIT used to generate patterns by LIL. A pulsed Nd:YAG laser is used as the source laser with an output wavelength of 355 nm - the third harmonic of the fundamental ($\lambda = 1064$ nm) of the laser. The third harmonic is utilised as the laser source can generate reasonably large powers at this wavelength and to enable the use of standard photoresists in sample patterning.

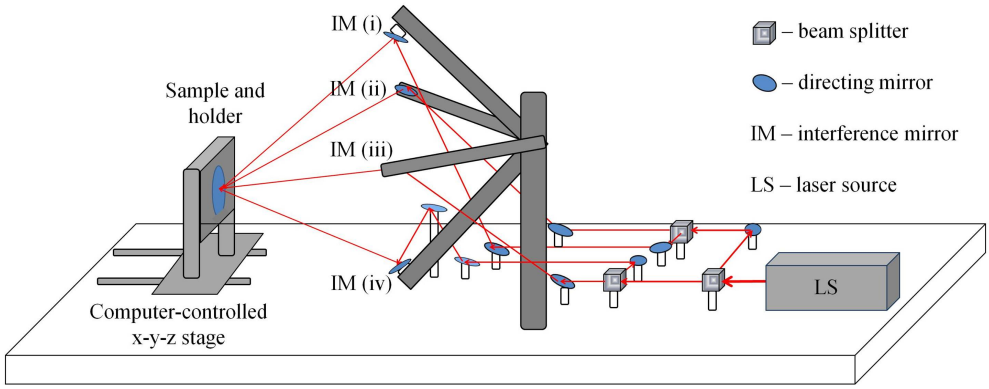

Figure 3.12: Schematic indicating the essential components of the laser interference lithography set-up at CEIT.

The initial laser beam can be split into two, three or four separate beams using beam-splitters (figure 3.12) before recombining from the respective number of mirrors. Careful selection of beam splitter locations and the optical path of each beam allows for equal amplitudes of the beams at the point of interference. This reduces the number of parameters and allows enhanced control of the final interference pattern. The interference mirrors are held in a plane at a specific distance from the sample mount which can be moved using a computer-controlled x-y-z stage. The angle of each mirror, and therefore the distance of the sample at the point of beam interference, can be manually adjusted to influence both the type of pattern and the size of the features produced within it.

The size of the interference pattern is determined by the overlapping beam waists of the interfering beams, which at CEIT corresponds to an area of approximately 1 cm^2. By blocking the path of the laser to any of the interference mirrors, the number of interfering beams can be varied. Adjustment of the position of the arms holding the interfering mirrors also allows for variations in the interference pattern. At CEIT these arms can be rotated around an axis such that the interfering mirrors remain the same distance from the sample. A description of the mechanics involved in controlling the arms of the interfering mirrors is outlined in [31].

Additional control of the interference pattern is achieved by utilising half-wave plates to rotate the polarization direction of the linearly polarized beams. Figure 3.13 shows a modelled pattern for a 3-beam configuration with interfering mirrors i, ii and iv from figure 3.12 in use. In figure 3.13 the simulated pattern is a triangular lattice photonic crystal (a = 300 nm) with elliptical unit cells. In the LIL process, deposition of a 600 nm thick layer of AZ-1505 photoresist is followed by spin coating and pre-baking. After which, the photoresist is exposed with a single laser pulse and a subsequent post-bake. Finally, the photoresist is developed in a 1:5 dissolution of AZ-315B developer and hard-baked. A silicon wafer coated with photoresist as a test sample yields a pattern of great similarity, as shown in figure 3.14.

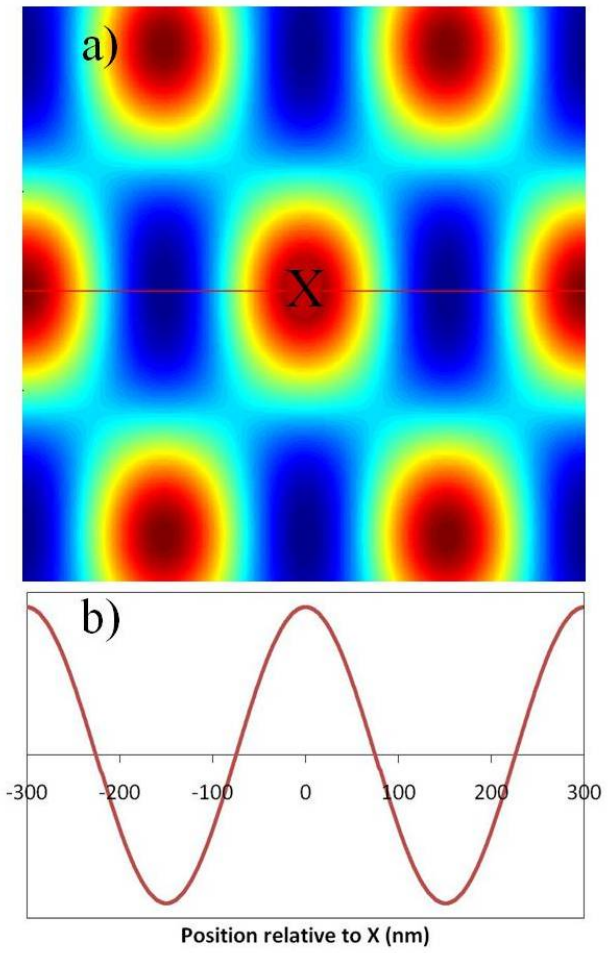

Figure 3.13: a) Modelled intensity distribution for a 3-beam interference pattern with red and blue indicating high and low intensity respectively. b) Intensity cross-section along the line in a).

Whilst tests such as that in figure 3.14 show a good surface pattern, transferance of the process onto a GaAs substrate (with the initial epitaxial growth described earlier) is not easily achieved, as the resist layer does not completely develop. This is due to surface reflections caused by the higher refractive index

semiconductor, which in turn causes disturbances in the interference pattern within the resist as reported in [25]. Efforts to reduce these disturbances with varying resist thicknesses and anti-reflection coatings have so far proved unsuccessful at patterning on GaAs.

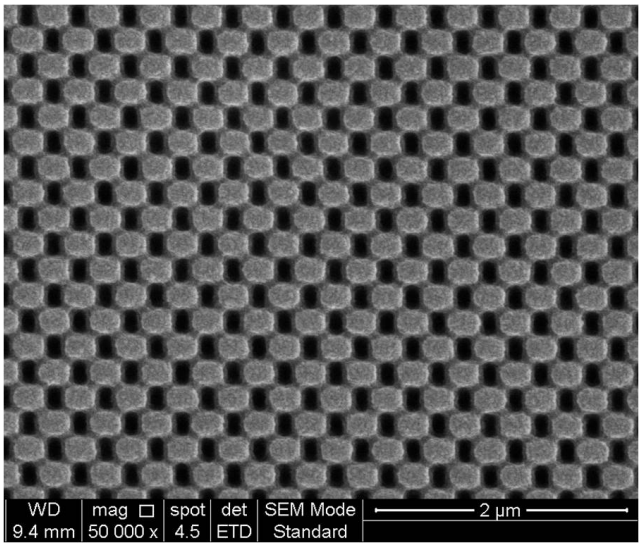

Figure 3.14: Scanning electron microscope image of a 3-beam interference pattern in resist on a silicon test wafer.

3.4.3 Etch optimisation

Once a surface pattern is achieved, the correct etch to transfer this into the relevant semiconductor layer is necessary. In the structure described above, this material is the 150 nm p-$In_{0.48}Ga_{0.52}P$ layer. Previous work at the University of Sheffield on buried DFB grating quantum cascade lasers with feature sizes of 1.68 μm showed that successful ICP etch recipes for InGaP are possible at

room temperature [32]. However, initial tests on the small features of a circular atom shape (diameter = 100 nm) in a photonic crystal with period a = 300 nm, and a relatively shallow depth of 150 nm, proved to be inconsistent. This inconsistency arises from the size of the features, and in comparison to [32] the additional dimension of the grating significantly reduces the area for etched material to escape.

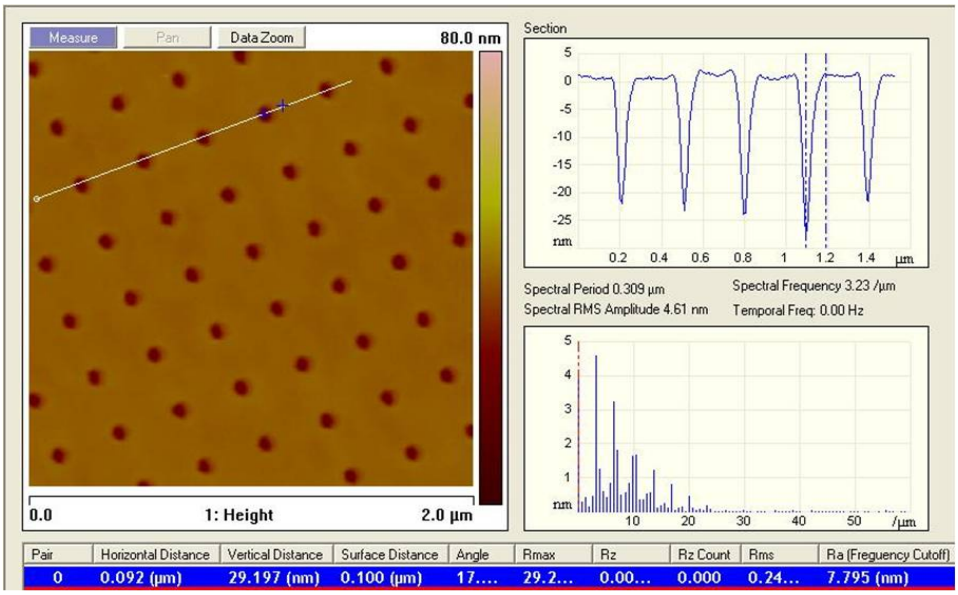

Figure 3.15: Etch profile as measured by atomic force microscopy.

Adapting the ICP etch recipe in [32], a relatively lengthy etch (10-15 nm/min) using argon and chlorine chemistry achieved the required depth, but with feature sidewalls sloping considerably. Figure 3.15 shows an atomic force microscope (AFM) image of the photonic crystal after a short (3 min-

utes) room temperature ICP etch. The cross-section measured along the white line indicates that the etch is shallow with the sidewalls quickly sloping into the middle of the features. Increasing the etch temperature to 200 °C makes the sidewalls significantly more vertical apart from at the very bottom of the features. The required 150 nm is clearly reached in figure 3.8, and the etch rate increased dramatically to approximately 150 nm/min at 200 °C.

3.5 Conclusions

This chapter considered the growth and fabrication of an all-semiconductor photonic crystal, in addition to discussing alternative solutions to processing techniques. The relevant fabrication technologies are briefly outlined before the successful fabrication recipe for generating an all-semiconductor photonic crystal is described.

A high V-III ratio and 10° substrate miscut was found to be necessary to achieve complete infill of the photonic crystal. The critical role of MOVPE in the regrowth process has been highlighted and the adjustment of the growth recipe has resulted in void removal from the photonic crystal. The device processing required for incorporating an all semiconductor photonic crystal into an electrically pumped PCSEL is also outlined.

The use of laser interference lithography as a large area alternative pat-

terning technique is introduced, however, problems with pattern transference from the resist have so far prevented the use of this. Development of the etch processes required for such high aspect ratio features is also discussed. A high temperature ICP etch using argon and chlorine chemistry is found to be successful in producing relatively vertical sidewalls.

3.6 Future work

Subsequent chapters show that the regrowth recipe and device processing outlined above is sufficient to realise a PCSEL. However, further work on the fabrication process is still required.

Continuation of LIL experiments using alternative anti-reflective coatings, or creating patterns in alternative materials as sacrificial masks, is essential to realise an efficient large area patterning technique for reducing costs.

Optimisation of the device processing, in particular the optical lithography and mesa etching steps would help increase PCSEL yield and the electrical performance of devices.

Variation of both the mesa size and the photonic crystal size is required to determine if there are any detrimental effects with regards to power scaling. In addition, if the dimensions of these two are similar, any boundary affects created by pumping the edge of the photonic crystal will be revealed.

References

[1] "Epitaxially regrown GaAs based photonic crystal surface emitting laser" D. M. Williams, K. M. Groom, B. J. Stevens, D. T. D. Childs, R. J. E. Taylor, S. Khamas, R. A. Hogg, N. Ikeda and Y. Sugimoto. Photon. Tech. Lett., **24**, No. 11, 966 (2012)

[2] "Multidirectionally distributed feedback photonic crystal lasers" M. Imada, A. Chutinan, S. Noda and M. Mochizuki. Phys. Rev. B, **65**, 195306 (2002)

[3] "Coherent two-dimensional lasing action in surface-emitting laser with triangular-lattice photonic crystal structure" M. Imada, S. Noda, A. Chutinan, T. Tokuda, M. Murata and G. Sasaki. Appl. Phys. Lett., **75**, No. 3, 316 (1999)

[4] "Polarisation mode control of two-dimensional photonic crystal laser by unit cell design" S. Noda, M. Yokoyama, M. Imada, A. Chutinan and M. Mochizuki. Science, **293**, 1123 (2001)

[5] "Alignment and stacking of semiconductor photonic bandgaps by wafer fusion" S. Noda, N. Yamamoto, M. Imada, H. Kobayashi and M. Okano. J. Lightwave Tech., **17**, No. 11, 1948 (1999)

[6] "Room-temperature triangular-lattice two-dimensional photonic band gap lasers operating at 1.54 μm" J-K. Hwang, H-Y. Ryu, D-S. Song, I-Y. Han, H-W. Song, H-K. Park, Y-H. Lee and D-H. Jang. Appl. Phys. Lett., **76**, No. 21, 2982 (2000)

[7] "GaN-based two-dimensional surface-emitting photonic crystal laser with AlN/GaN distributed Bragg reflector" T-C. Lu, S-W. Chen, L-F. Lin, T-T. Kao, C-C. Kao, P. Yu, H-C. Kuo, S-C. Wang and S. Fan. Appl. Phys. Lett., **92**, 011129 (2008)

[8] "Characteristics of GaN-based photonic crystal surface emitting lasers" T-C. Lu, S-W. Chen, T-T. Kao and T-W. Liu. Appl. Phys. Lett., **93**, 111111 (2008)

[9] "GaN photonic-crystal surface-emitting laser at blue-violet wavelengths" H. Matsubara, S. Yoshimoto, H. Saito, Y. Jianglin, Y. Tanaka and S. Noda. Science, **319**, 445 (2008)

[10] "GaN-based surface-emitting laser with two-dimensional photonic crystal acting as distributed-feedback grating and optical cladding" S. Kawashima, T. Kawashima, Y. Nagatomo, Y. Hori, H. Iwase, T. Uchida, K. Hoshino, A. Numata and M. Uchida. Appl. Phys. Lett., **97**, 251112 (2010)

[11] Image adapted from http://cnx.org/content/m25614/latest/?collection =col10719/latest, itself adapted from "Thin Film Processes II" K. F. Jensen and W. Kern. Academic Press, New York (1991).

[12] "CCS-MOCVD reactor gallium nitride" Thomas Swan Scientific Equipment Ltd. www.fabsurplus.com/sdi_catalog/download?id=33750

[13] "Optimisation of coupling between photonic crystal and active elements in an epitaxially regrown GaAs based photonic crystal surface emitting laser" D. M. Williams, K. M. Groom, B. J. Stevens, D. T. D. Childs, R. J. E. Taylor, S. Khamas, R. A. Hogg, N. Ikeda, and Y. Sugimoto. Jap. J. Appl. Phys., **51** 02BG05 (2012).

[14] "All-semiconductor photonic crystal surface emitting lasers based on epitaxial regrowth" R. J. E. Taylor, D. M. Williams, D. T. D. Childs, B. J. Stevens, L. R. Shepherd, S. Khamas, K. M. Groom, R. A. Hogg, N. Ikeda and Y. Sugimoto. IEEE J. Sel. Topics Quant. Electron., **19**, No. 4, (2013)

[15] "Band structure and waveguide modelling of epitaxially regrown photonic crystal surface emitting lasers" R. J. E. Taylor, D. M. Williams, J. R. Orchard, D. T. D. Childs, S. Khamas and R. A. Hogg. J. Phys. D: Appl. Phys., **46**, 264005 (2013)

[16] "10nm linewidth electron beam lithography on GaAs" H. G. Craighead, R. E. Howard, L. D. Jackel and P. M. Mankiewich. Appl. Phys. Lett., **42**, 38 (1983)

[17] "Electron beam lithography: resolution limits and applications" C. Vieu, F. Carcenac, A. Pepin, Y. Chen, M. Mejias, A. Lebib, L. Manin-Ferlazzo, L. Couraud and H. Launois. Appl. Surface Science, **164**, 111 (2000)

[18] "Fabrication of photonic bandgap crystals" C. C. Cheng and A. Scherer. J. Vac. Sci. Technol. B., **13**, 2696 (1995)

[19] "III-nitride blue and ultraviolet photonic crystal light emitting diodes" T. N. Oder, K. H. Kim, J. Y. Lin and H. X. Jiang. Appl. Phys. Lett., **84**, No. 4, 466 (2004)

[20] "Fabrication of low loss two-dimensional InP photonic crystals by inductively coupled plasma etching" F. Pommereau, L. Legouezigou, S. Hubert, S. Sainson, J-P. Chandouineau, S. Fabre, G-H. Duan, B. Lombardet, R. Ferrini and R. Houdre. J. Appl. Phys., **95**, No. 5, 2242 (2004)

[21] "Spontaneous emission control of colloidal nanocrystals using nanoimprinted photonic crystals" V. Reboud, N. Kehagias, C. M. Sotomayor Torres, M. Zelsmann, M. Striccoli, M. L. Curri, A. Agostiano, M. Tam-

borra, M. Fink, F. Reuther and G. Gruetzner. Appl. Phys. Lett., **90**, 011115 (2007)

[22] "Fabrication of polymer photonic crystals using nanoimprint lithography" H. Schift, S. Park, B. Jung, C-G. Choi, C-S. Kee, S-P. Han, K-B. Yoon and J. Gobrecht. Nanotechnology, **16**, 261 (2005)

[23] "Fabrication of semiconductor and polymer based photonic crystals using nanoimprint lithography" E. M. Arakcheeva, E. M. Tanklevskaya, S. I. Nesterov, M. V. Maksimov, S. A. Gurevich, J. Seekamp and C. M Sotomayor Torres. Tech. Physics, **50**, Iss. 8, 1043 (2005)

[24] "Fabrication of photonic crystals for the visible spectrum by holographic lithography" M. Campbell, D. N. Sharp, M. T. Harrison, R. G. Denning and A. J. Turberfield. Nature, **404**, 53 (2000)

[25] "Large-area two-dimensional silicon photonic crystals for infrared light fabricated with laser interference lithography" L. Prodan, T. G. Euser, H. A. G. M. van Wolferen, C. Bostan, R. M. de Ridder, R. Beigang, K-J. Boller and L. Kuipers. Nanotechnology, **15** 639 (2004)

[26] "Near-infrared Yablonovite-like photonic crystals by focused ion beam etching of macroporous silicon" A. Chelnokov, K. Wang, S. Rowson, P. Garoche and J-M. Lourtioz. Appl. Phys. Lett., **77**, No. 19, 2943 (2000)

[27] "a $SiO_x < Er >$ active photonic crystal resonator membrane fabricated by focused Ga^+ ion beam" D. S. L. Figueira, L. A. M. Barea, F. Vallini, P.F. Jarschel, R. Lang and N. C. Frateschi. Opt. Express, **20**, No. 17, 18774 (2012)

[28] "Photonic crystals for the visible range fabricated by autocloning technique and their application" T. Sato, K. Miura, N. Ishino, Y. Ohtera, T. Tamamura and S. Kawakami. Opt. and Q. Electron., **34**, 63 (2002)

[29] "Tailoring of the unit cell structure of autocloned photonic crystals" T. Kawashima, T. Sato, Y. Ohtera and S. Kawakami. IEEE J. Quant. Electron., **38**, No. 7, 899 (2002)

[30] "Limits of lithography" L. R. Harriott. Proceedings of the IEEE, **89**, No. 3, 366 (2001)

[31] 'Laser interference lithography for nanoscale structuring of materials: From laboratory to industry' A. Rodriguez, M. Echeverra, M. Ellman, N. Perez, Y. Verevkin, C. S. Peng, T. Berthou, Z. Wang, I. Ayerdi, J. Savall and S. M. Olaizola. Microelectronic Engineering, **86**, 937 (2009)

[32] "High performance InP-based quantum cascade distributed feedback lasers with deeply etched lateral gratings" K. Kennedy, A. B. Krysa, J.

S. Roberts, K. M. Groom, R. A. Hogg, D. G. Revin, L. R. Wilson and J. W. Cockburn. Appl. Phys. Lett., **89**, 201117 (2006)

4 Low Temperature Characterisation

4.1 Introduction

In this chapter device characteristics of a sample of 30 all-semiconductor PCSELs (including each of the different periods fabricated) at low temperatures are outlined. Data considered in this chapter comes from devices fabricated using processes outlined in chapter 3 and some results have already been published [1, 2]. The data is used to; confirm that laser oscillation occurs in these devices and, outline some of the unique characteristics that suggest the photonic crystal is responsible for the emission. First, the characterisation method of the electroluminescence spectra, threshold currents and far-field patterns for PCSELs operating at low temperature is described. Results, analysis and comparison with previous values reported in the literature follows.

4.2 Background

Historically, device research typically requires multiple steps in developing to the point of room-temperature continuous wave operation, however, PCSEL publications suggest they are an exception to this. Initial research on a two-dimensional thin-film distributed feedback laser in 1973 [3] failed to incite interest in researching a two-dimensional semiconductor PCSEL. However, the

literature indicates that there was a revival in interest in PCSEL research in 1998 and 1999 through the use of organic gain media [4, 5]. Initial fabrication of an electrically pumped semiconductor photonic crystal operating at room temperature was first demonstrated in 1999 [6]. Despite only operating under pulsed conditions, there appears to be no development or characteristics at low temperatures reported. Furthermore, room-temperature continuous wave operation of a PCSEL did not take long to follow [7]. This chapter investigates the operation of PCSELs at low temperature in an attempt to bridge the gap reported in the literature. The testing of devices at low temperature is a key step in identifying the unique properties of a new type of device, with the reduction of thermal effects allowing for clear characterisation.

For low temperature characterisation of any device a well-designed cryostat set-up is essential. The set-up used to record the data in this chapter was implemented previously for low temperature spectral and output power measurements [8]. Figure 4.1 is a schematic of the system highlighting the key optics and characterisation equipment required for the EL spectra and output power tests conducted in this chapter.

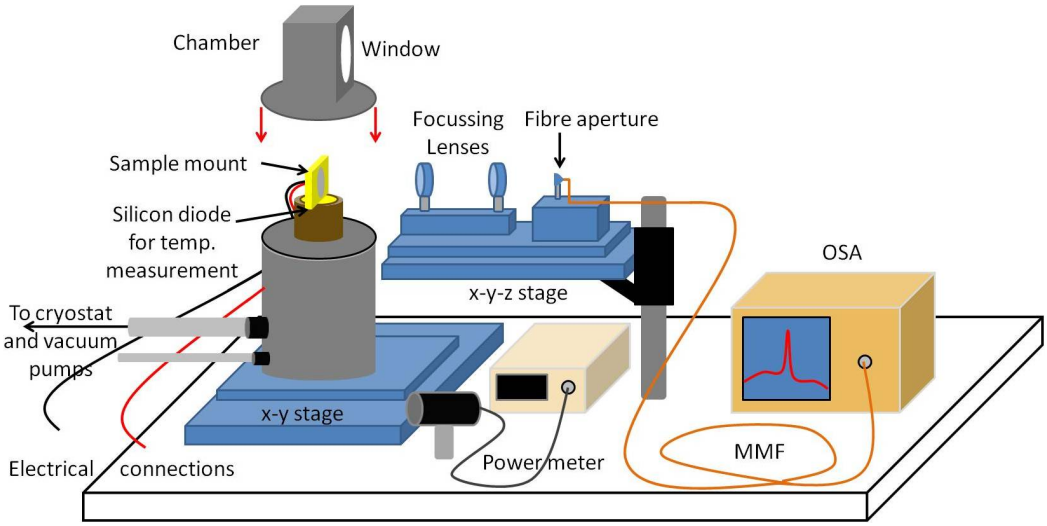

Figure 4.1: Experimental set-up schematic for low temperature spectral and output power measurements.

Figure 4.1 indicates the location of the sample mount, where the device under test (DUT) is bonded to a TO-5 header [9] to provide thermal and electrical connections. The chamber is pumped down to a vacuum on the order of 10^{-7} millibar before the cryostat is engaged [10]. The cryostat relies on a water-cooled compressor to pressurise helium, which is then allowed into the chamber through a small expansion hole. Helium expansion draws heat from the surrounding metal which is connected to the sample mount, and can reduce the temperature to as low as 10 K. Precise control of the temperature is achieved using the temperature dependence of the turn-on voltage of a silicon diode located just beneath the sample mount [11]. Suitable time was left for

the DUT to adjust to temperature changes between data measurements.

Emission from the DUT is able to escape the chamber through the window. The first lens (numerical aperture 0.5) collects as much light from the sample as possible and collimates it (this lens is aspheric to avoid aberrations). The second lens focuses this light down to the multimode fibre (MMF) which has a numerical aperture of 0.14. Losses due to reflections from the lenses are reduced by up to 8% using antireflective coatings for near infra red wavelengths. Alignment of the DUT, lenses and the MMF is controlled manually via x-y and x-y-z stages. Analysis of the emission from the DUT is conducted using an optical spectrum analyser (OSA) [12]. Output powers are recorded on the powermeter [13] by removing the focussing lenses and positioning the InGaAs powerhead sensor [14] as close to the chamber window as possible.

Also outlined in this chapter is characterisation of the far-field pattern at low temperatures. A goniometric radiometer is utilised and replaces the optical lenses in figure 4.1. Situated as close to the chamber window as possible, the goniometer collects the emission through a narrow slit (approximately 1 cm wide) orientated at various angles to the DUT.

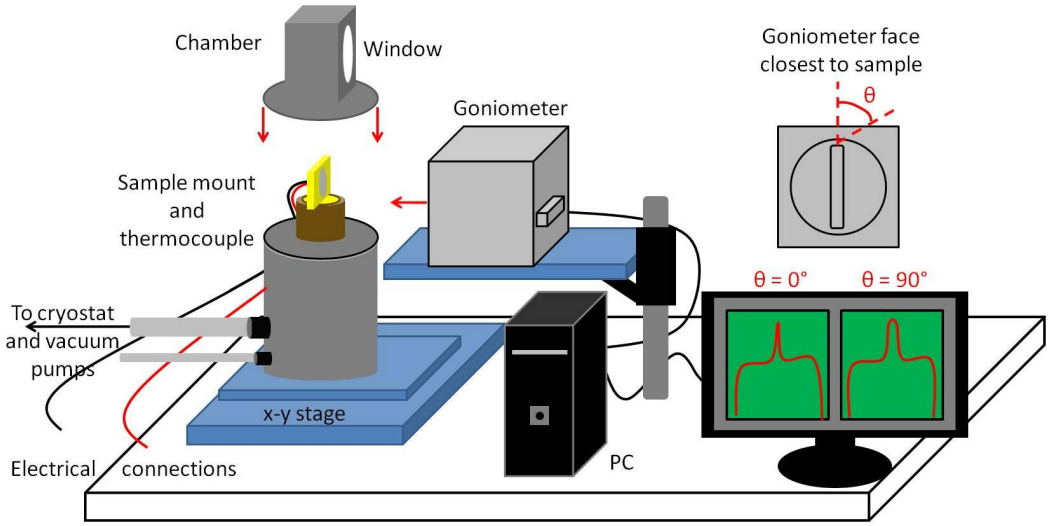

Figure 4.2: Experimental set-up schematic for low temperature far-field measurements.

Figure 4.2 indicates the definition of the angle θ on the goniometer face closest to the sample. A goniometric radiometer collects emission from various angles, and in this chapter cross-sections in the 0° and 90° orientations are considered [15]. These can be used to give a clear indication of the divergence of the laser beam for comparison with other devices in the literature. The goniometer is able to correct the far-field emission angles provided the distance to the sample is known (approximately 19 mm in this experiment).

Small beam divergences are important for communication and remote-sensing applications, as the laser beam can be efficiently coupled to waveguides and fibres without requiring lenses or other costly and bulky optical elements. As outlined in chapter 1, careful design of the photonic crystal in a

PCSEL can influence the beam characteristics [16]. Using photonic crystals, diffraction-limited beam divergences have been generated [17]. In PCSELs, far-field patterns of less than 1° have been achieved when considering the full width at half maximum (FWHM) of the emission intensity [18]. This gives PCSELs an edge over other types of semiconductor lasers. For instance, vertical cavity surface emitting lasers (VCSELs) typically have divergences of 10°-15° [20, 21], whereas edge emitting ridge lasers have divergences over 30° due to the narrow stripe widths [22–25].

4.3 Basic characteristics

4.3.1 VI, LI curves and EL spectra

Figure 4.3 plots the forward voltage-current (VI) characteristics for a 286 nm period PCSEL over a range of temperatures. The curves indicate the device is operating as a diode with a turn-on voltage of 1.1 - 1.5 V depending on the temperature. At most temperatures the curves are almost identical making it difficult to distinguish between them, however, at 255K and 295K the voltage is slightly reduced at all currents. Taking a fit to the VI curves in the linear regime (I = 100 - 300 mA) and calculating the gradient gives the resistance of the device in this current region. Calculating this for a range of devices of different photonic crystal periods produces the data *inset* in figure 4.3.

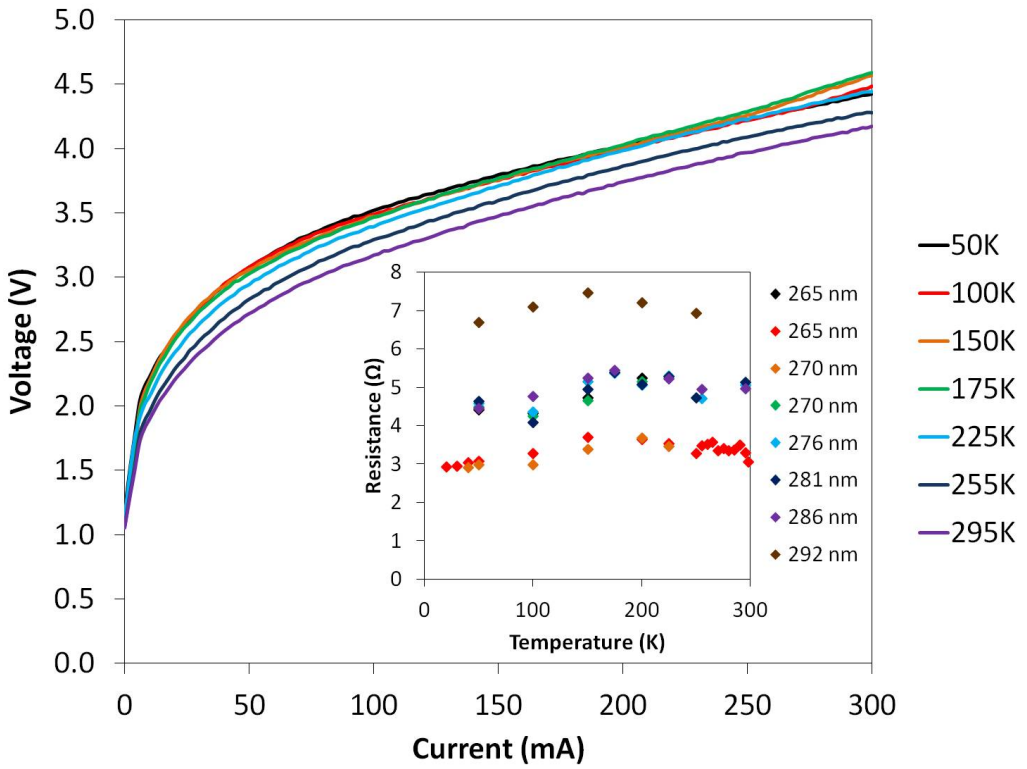

Figure 4.3: Forward drive voltage against current at various temperatures. *Inset:* Resistance versus temperature from the linear regime in the VI curves.

There is a clear range of resistances, with three distinct regions at approximately 3, 5 and 7 Ω. At first glance it appears there is a trend with resistance increasing as photonic crystal period is increased, however, there are exceptions to this trend. For example, the resistances of the 265 nm and 270 nm devices fall into both the 3 Ω and 5 Ω regions. Examination of the location of these devices on the processed wafer reveals that the variation in resistance occurs due to the device location rather than the photonic crystal period. De-

vices from regions close together fall into one of the three regions. For each device the resistance in this linear current region appears roughly constant at all temperatures.

The light output-injection current (LI) characteristics for a PCSEL with photonic crystal period 281 nm operating under pulsed conditions (up to 200 mA) over a range of temperatures is shown in figure 4.4. In this case, the device was electrically pumped with a pulse width of 5 μs and a duty cycle of 1% in order to reduce the effects of self-heating. Figure 4.4 indicates that there is significantly greater output power achieved at lower temperatures (output power response measured at $\lambda = 980$ nm). This occurs due to the increased efficiency of the electron-hole recombination in the quantum wells at lower temperatures, and hence a higher gain is reached.

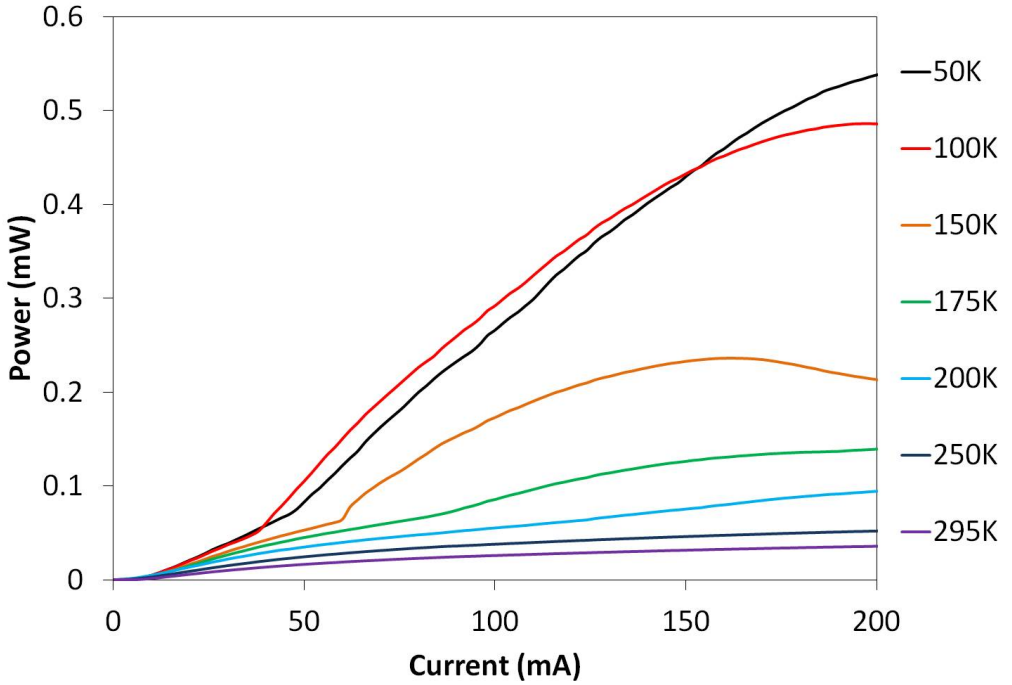

Figure 4.4: Light-output against current injection (LI) curves as a function of temperature. (PCSEL period, a = 281 nm).

At 50K, 100K and 150K there is an obvious kink in the LI curves suggesting that lasing occurs. Threshold currents of 31 mA, 27 mA and 51 mA are measured at 50K, 100K and 150K respectively. A closer inspection of the higher temperature LI curves reveals slight kinks exist, but that a much smaller slope efficiency reduces the appearance of these in figure 4.4. The threshold current has a local minima at 100K for the temperatures considered here. Further investigation into the temperature dependence of the threshold current follows in section 4.5. Despite these apparent thresholds in the LI curves it is

important to examine the electroluminescence spectra (figure 4.5) to determine if lasing is truly occuring. At currents of 198 mA and 164 mA (temperatures of 100K and 150K respectively) the LI curve reaches a local maximum suggesting thermal rollover.

The threshold current minimum at 100K occurs as there is increased gain at this temperature, and also because of the alignment of the gain peak and the wavelength that satisfies the Bragg condition of the photonic crystal within the device. When there is good alignment the threshold current is reduced, whilst poor alignment results in increased threshold. An example of the possible detuning between the two peaks is clearly evident in figure 4.5 where there is poor alignment. Detuning of the lasing and gain peaks is considered in more detail in section 4.3.3.

Figure 4.5 shows the electroluminescence spectra at 100 K for a PCSEL (photonic crystal period a = 265 nm) operating at a range of currents under pulsed drive conditions. The relatively low output power of these devices and the collection losses caused by the use of the MMF results in noisy spectra. Note the use of a logarithmic scale on the y-axis to accentuate the key features in the spectra.

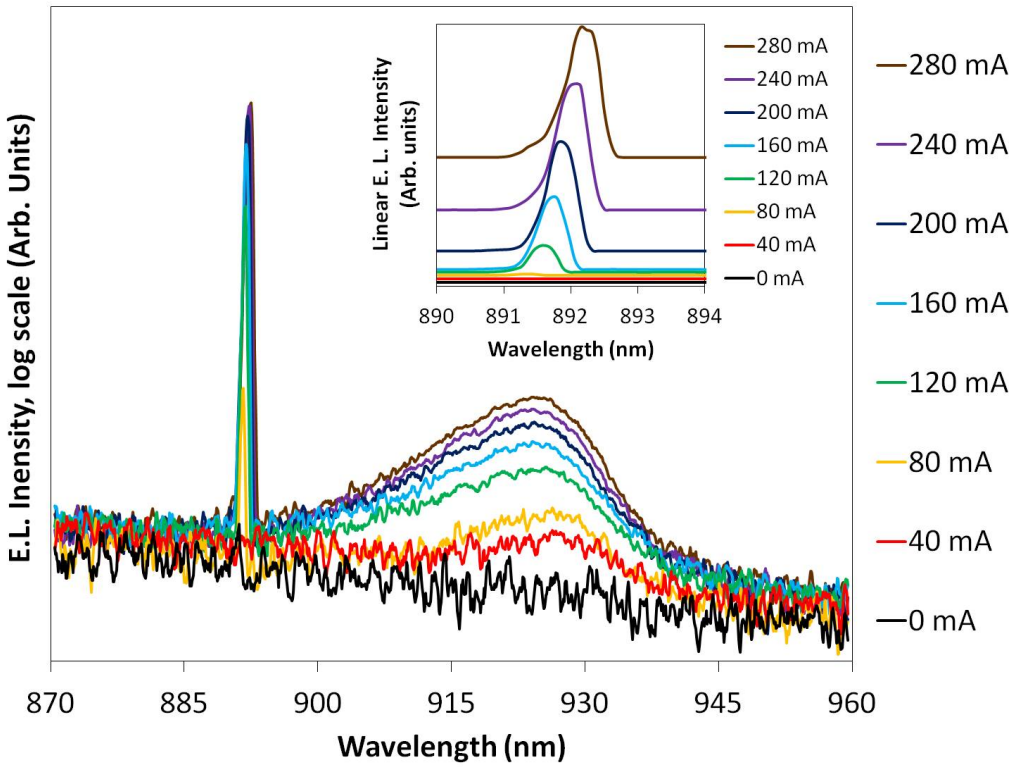

Figure 4.5: Logarithmic electroluminescence spectra as a function of current for a device with period a = 265 nm at 100K. *Inset*: Linear spectra for the same device at wavelengths close to the lasing peak (for clarity spectra have been shifted by an arbitrary amount up the y-axis).

Whilst there is a significant amount of background noise at both high and low wavelengths in these spectra, the broad peak due to spontaneous emission from the quantum wells, and the sharp, narrow lasing peak due to the two dimensional feedback effect of the photonic crystal are both evident. High resolution measurements of the peak wavelengths are recorded using the 0.2 nm resolution bandwidth of the optical spectrum analyser (see figure 4.1 for

experimental set-up). In figure 4.5 the peak of the spontaneous emission at 280 mA is $\lambda = 924.1$ nm and from the *inset* of figure 4.5 the lasing peak at the same current is $\lambda = 892.2$ nm. The detuning of 31.9 nm between these peaks is quite large and indicates that the photonic crystal design is far from optimal for this device. This is the smallest of the periods fabricated, and the smaller detunings achieved from other devices with larger periods can be observed in figure 4.9.

The inset to figure 4.5 shows the EL spectra zoomed in around the region of the lasing peak on a linear scale (for the same device). The spectra have been shifted along the y-axis to clarify the features between each current value. Below threshold no peak is visible, whilst above threshold the lasing peak quickly increases in size. There is also a small shift in lasing wavelength as the current increases.

4.3.2 Lasing peak shift and linewidths

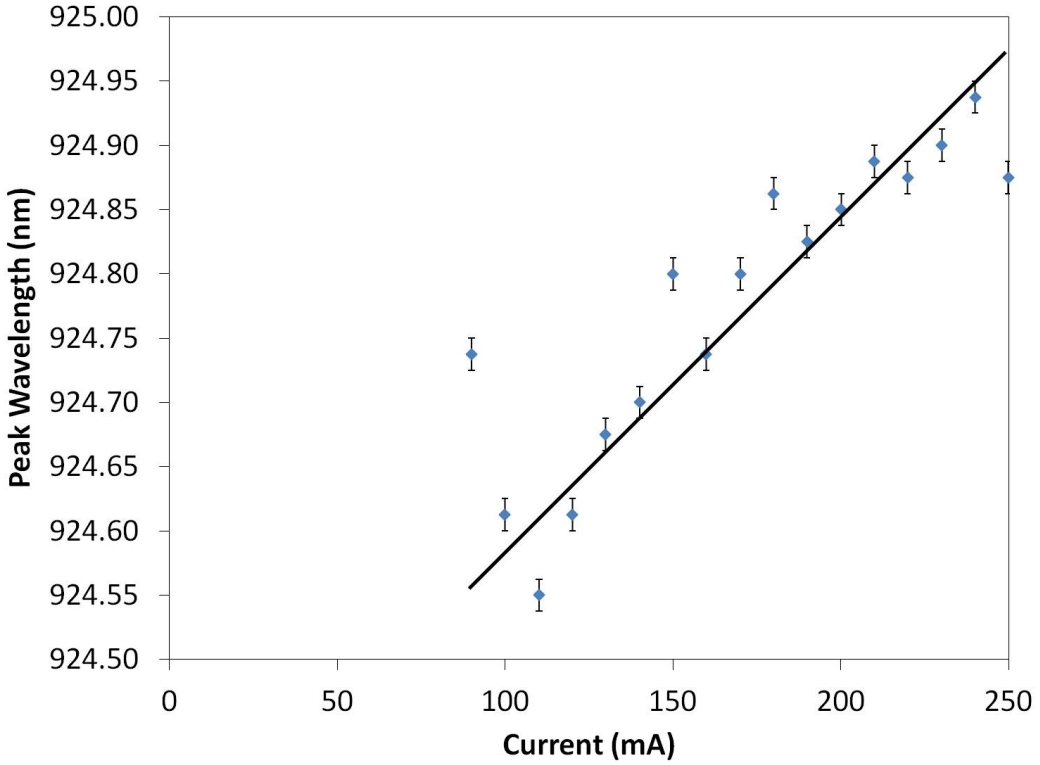

Figure 4.6: Shift of photonic crystal lasing peak wavelength as a function of current for a different device of period a = 276 nm at 150K. Above threshold linear trend indicated by black line.

Figure 4.6 plots the photonic crystal laser peak wavelength as a function of current, for a device with a threshold current of 100 mA operating under pulsed conditions at 150K. There is a steady, but shallow, linear increase in peak wavelength as the current is increased above threshold. Over the current range considered here the photonic crystal peak shifts by a maximum of 0.39

nm, and this is likely due to the injected carriers altering the refractive index of the waveguide as self-heating would give a dependence proportional to I^2 [26]. The peak observed at 90 mA appears not to follow the trend (black line) as this corresponds to a sub-threshold peak.

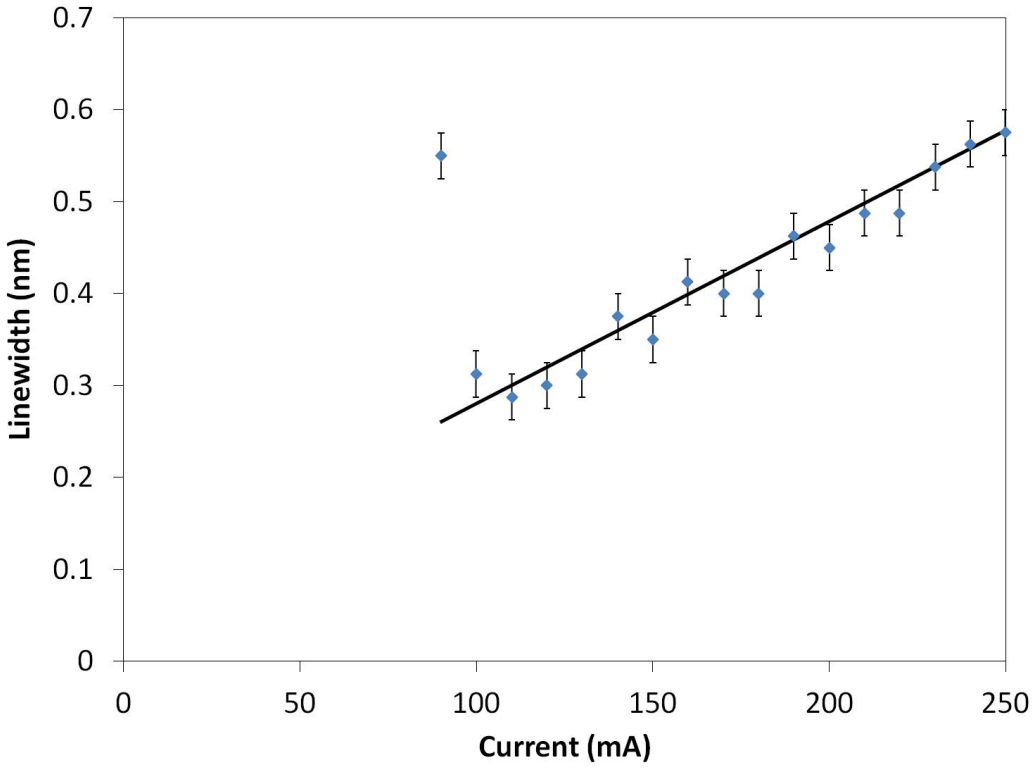

Figure 4.7: Spectral linewidths as a function of current for the same device of period a = 276 nm at 150K. Above threshold linear trend indicated by black line.

The linear increase in spectral linewidth with current is plotted in figure 4.7. The black line clearly indicates the linear correlation for currents above threshold, with linewidth increasing from 0.29 nm to 0.58 nm over this current

range. The cold cavity linewidth is usually taken as the linewidth well below threshold where the number of carriers is close to zero (see figure 4.8), but due to the low signal to noise ratio in the EL spectra (figure 4.5) this is difficult to measure.

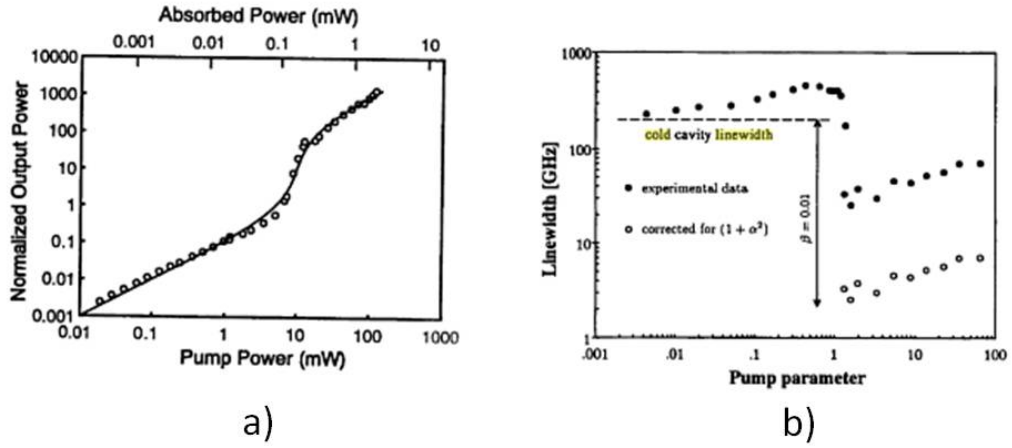

Figure 4.8: a) Normalised output power as a function of pump power (bottom axis) and absorbed power (top axis). b) Linewidth dependence on pump parameter. *Adapted from* [27].

Figure 4.8a) plots the output power response as a function of input power (and absorbed power) for a defect cavity surface emitting laser in [27]. Figure 4.8b) plots the linewidth as a function of absorbed pump power (pump parameter) and indicates the cold cavity linewidth. This is extrapolated up to threshold pump parameters where the linewidth clearly reduces. A similar drop in linewidth is observed in figure 4.7 from the one sub-threshold linewidth plotted. The sub-threshold linewidth at the transparency point can be used

as a first approximation to the cold linewidth of the device, with 90 mA or $0.9I_{th}$ in figure 4.7 being considered close to transparency in a similar fashion to [28]. Figure 4.7 yields a cold cavity linewidth $\Delta\lambda = 0.55$ nm similar to that for band A in [28] ($\Delta\lambda = 0.57$ nm).

4.3.3 Detuning as a function of temperature

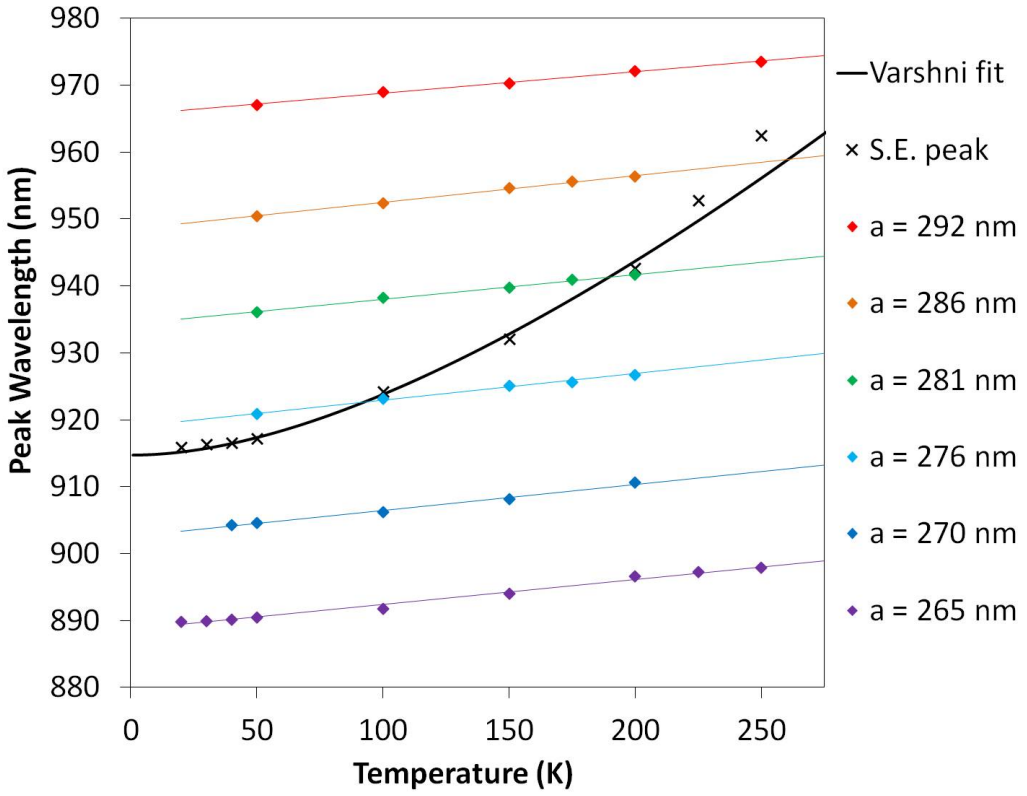

Figure 4.9: Lasing peak wavelength at 300 mA against temperature for a range of PCSELs with various periods, a. Peak of spontaneous emission from a typical device with a Varshni fit curve (black line) also plotted.

Figure 4.9 plots the lasing peak wavelength against temperature for a group of devices containing photonic crystals of varying periods (at a fixed injection current of 300 mA). Here, the high resolution of the OSA means errors in the wavelength are small so they are not visible under the plotted points. A low yield from device processing results in working devices of only six of the periods fabricated, hence there are no results for photonic crystals with period a = 297 nm.

Also plotted in figure 4.9 is the peak in spontaneous emission for a typical device, with a Varshni curve [29] fitted. This curve is an empirical fit based on 4.3.1, with fit parameters E_0 = 1.359 eV, $\alpha = 4.8{*}10^{-4}$ eV/K, β = 260 K.

$$E_g(T) = E_0 - \frac{\alpha T^2}{T + \beta} \tag{4.3.1}$$

These parameters give a purely empirical fit to the spontaneous emission peak wavelengths in figure 4.9, however, for InGaAs quantum wells in other structures in the literature, similar values are used (E_0 = 1.312 eV, α = 4.8 * 10^{-4} eV/K and β = 140 K) [30]. Whilst the Varshni curve with these parameters is a good fit at low temperatures, the fit is less accurate at high temperatures. This is due to the failing of the Varshni equation to take into account electron-phonon interactions, which become more influential at higher temperatures [31].

Previous work has shown that the semiconductor band-gap has a quadratic variation at low temperatures, and that at higher temperatures this becomes more linear [31,32]. In comparison, linear best fit lines for each of the different photonic crystal periods indicate a clear strong correlation between lasing peak wavelength and temperature. Examination of the best fit gradients indicates that the photonic crystal peak detunes between 0.03 and 0.04 nm/K depending on the device. The small temperature dependence of the wavelength is generated by the small variation in the period as the semiconductors forming the photonic crystal shrink or expand.

The linear correlation between peak wavelength and temperature for all photonic crystal periods in figure 4.9 allows for simple wavelength selectivity of a PCSEL by either changing the operating temperature, or the period, of the device. The detuning with temperature achieved by these PCSELs is small compared to DFBs (approximately 0.1 nm/K [33,34]), and even has a slightly smaller value than VCSELs (approximately 0.05-0.07 nm/K [35,36]), making them of use for stable wavelength emission applications in environments with fluctuating temperatures.

4.4 Low temperature far-field patterns and divergences

As mentioned earlier, previous PCSELs have been able to produce far-field patterns with divergences significantly lower than for other types of semiconductor lasers. Just one of the unique capabilities of PCSELs, this is an attribute created by the presence of the photonic crystal within the device. To confirm that the lasing peak seen in the EL spectra is created by the photonic crystal, this next section examines the far-field pattern and beam divergences.

Figure 4.10 is a plot of the cross-section of the far-field pattern in the $\theta = 0^{\circ}$ orientation (defined in figure 4.2) for various injection currents at 150K. The curves plotted here are normalised against the intensity of the high current cross-sections. In the cross-sections, the emission angle is taken as the angle to the normal of the plane of the device.

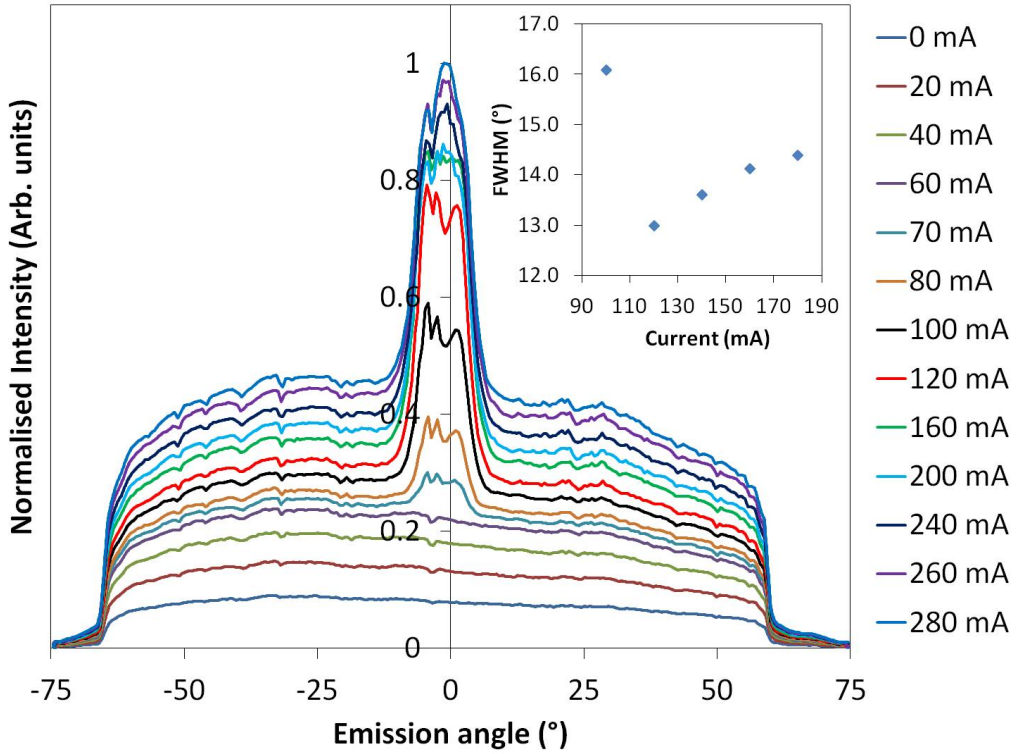

Figure 4.10: Far-field cross-section in the $\theta = 0°$ orientation as a function of current for a 276 nm period PCSEL at 150K. *Inset*: Full width half maxima (FWHM) for certain currents.

Below threshold, spontaneous emission is detected over a large range of emission angles (greater than 100°). The detection of spontaneous emission over a wide angle also occurs above threshold, and at 70 mA the emergence of the lasing peak occurs from the centre of the pattern. A high intensity peak at small emission angles in the cross-section like this is an indication of a collimated laser beam.

Compared with expected divergences from the literature [18], the full width half maximum (FWHM) for the far-field cross-sections (see figure 4.10 *inset*) yield a relatively high value for a PCSEL. However, this is still much lower than for single-mode edge emitting lasers [22–25] and comparable with VCSELs [20,21]. Error bars for the FWHM are small due to the high number of sample points in the cross-section so they are not visible beneath the data points.

The combination of the contribution from spontaneous emission and the relatively low output power is the cause for these high divergences. Points measured to give the FWHM are closer to the shoulders of the central peak than the half maxima. Examining the FWHM for the far-field at 80 mA gives evidence for this, as it yields a value of over 100° due to the relatively low intensity of the central peak. (Note this is not plotted in the *inset* to figure 4.10 so that the trend at higher currents is visible). In addition, the FWHM value for 100 mA is also distorted by this affect, and this is why this point appears not to follow the trend of the higher currents. At the currents plotted a simple linear increase with current is observed, and this current dependence is studied in more detail below.

Figure 4.11 plots the two perpendicular cross-sections of the far-field pattern of a 276 nm period PCSEL at 280 mA and 150K. In each case the background spontaneous emission is emitted over a large angle (greater than 100°).

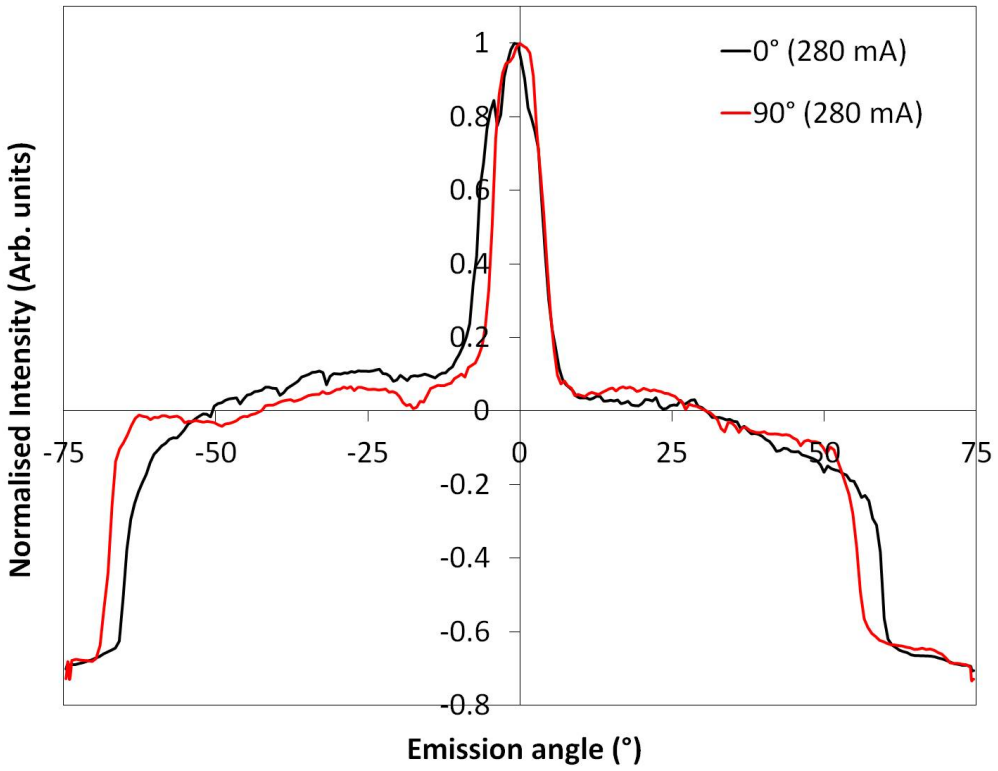

Figure 4.11: Normalised far-field cross-section in the $\theta = 0°$ orientation (black) and $\theta = 90°$ (red) for a 276 nm period PCSEL at 150K.

In figure 4.11 the data has had the spontaneous emission subtracted before renormalisation. This background is still plotted (as negative values) for completeness, but the normalisation results in the measurement of the full-width half maximum of the lasing peak alone. This gives a better indication of the true divergence of the laser beam of the PCSEL (figure 4.13).

The far-field profile in the 90° orientation (figure 4.12) yields some interesting results. In this case the spontaneous emission is measured over a wide

range of angles as before, however, the lasing peak is much narrower at low currents. Low current FWHM measurements reveal divergences as low as 2.9° are achieved. As injection current is increased above 140 mA, the far-field reveals a second peak appearing on the shoulder of the first. The new peak increases much more rapidly than the first, relative to the background, until they are of similar heights. At currents higher than this they increase at approximately the same rate. These two peaks cannot be individually resolved in figure 4.12 but suggest one possible reason for the larger divergences measured in the 0° orientation.

With two lasing peaks measured in the far-field, but only one in the electroluminescence spectra, the PCSEL may be lasing from multiple areas of the device. (Satisfaction of the Bragg condition ensures that lasing can only occur at one wavelength and large scale coherence has previously been reported for PCSELs [19]).

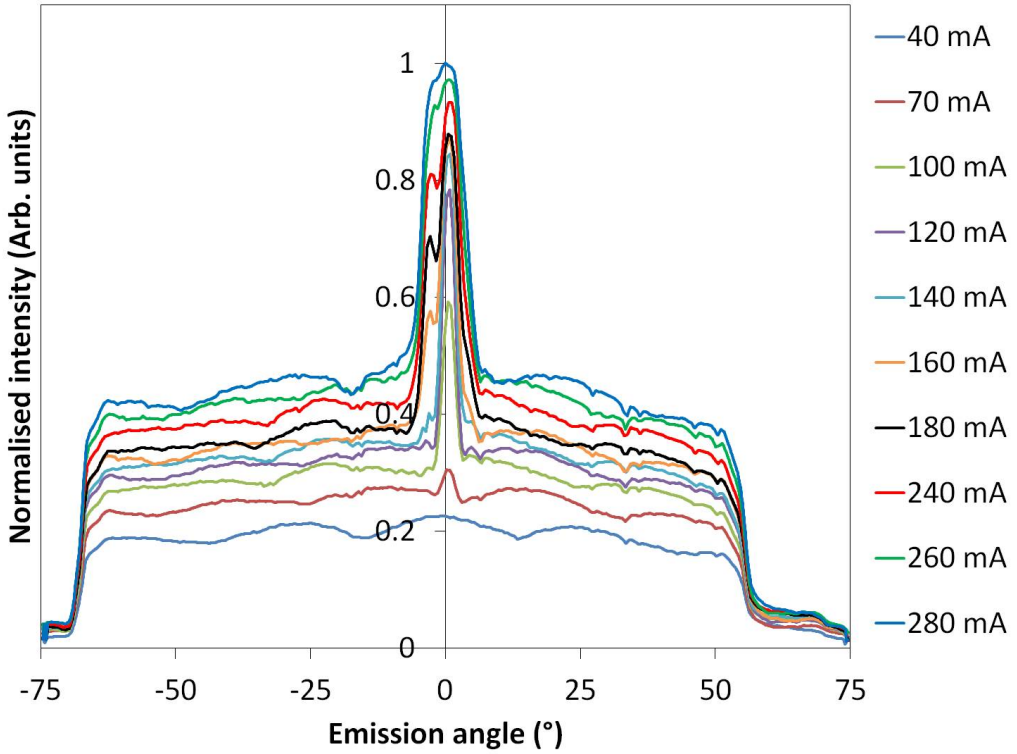

Figure 4.12: Far-field cross-sections in the $\theta = 90°$ orientation as a function of current for a 276 nm period PCSEL at 150K.

Near-field patterns could confirm if the device is lasing from multiple areas of the device, however, measurement of these at low temperatures is not possible with this set-up. The need for the pressurised chamber to achieve low temperature prevents close-proximity measurements with the device.

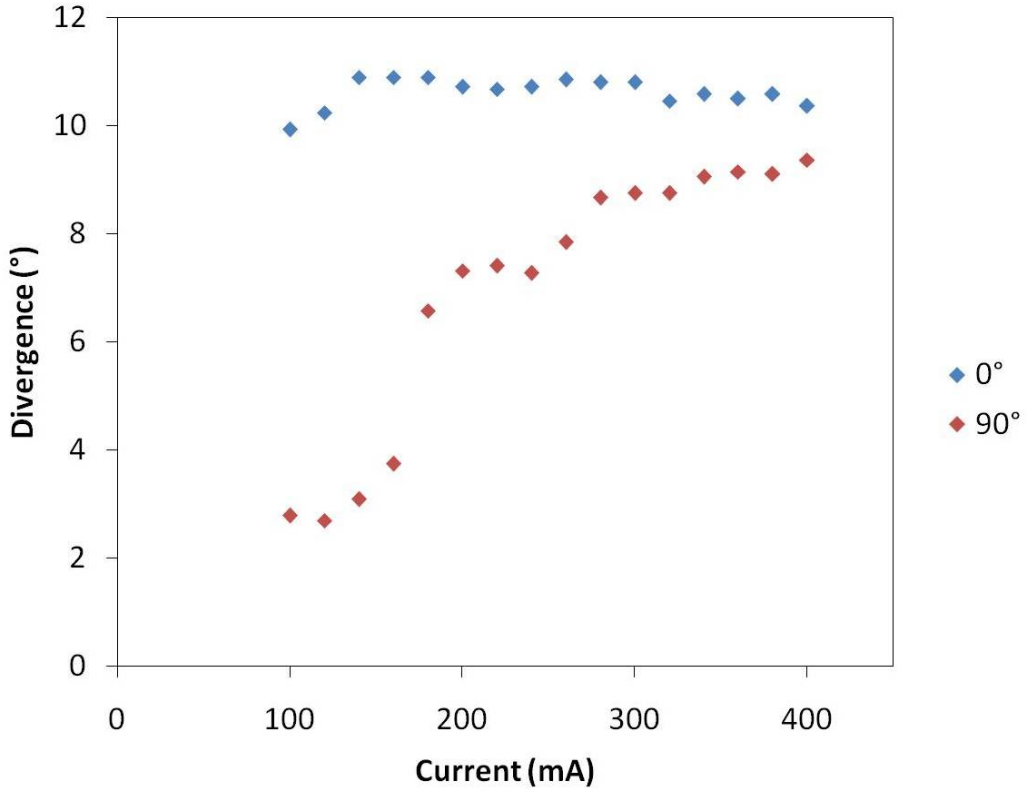

Figure 4.13: Divergence as a function of current for the $\theta = 0°$ and $\theta = 90°$ orientations of the far-field cross-sections.

FWHM or divergence measurements from plotting all currents in a similar fashion to figure 4.11 are shown in figure 4.13. The divergence of the lasing peak in the 0° orientation is reasonably consistent, varying from 9.9° to 11.1° in the current range 100 to 400 mA. As indicated above, the divergence of the 90° orientation is much more current dependent, ranging from 2.9° to 9.5° over this current injection regime.

Two possible explanations for the difference in the divergence of the two

orientations and their dependence on current exist. The first is attributed to the nature of the regrowth. Infill of the photonic crystal requires growth conditions that result in the interface of the layer immediately above the photonic crystal being non-planar. Examination of the TEM image in figure 3.11c) indicates this. If this layer is not symmetrical in the orthogonal direction, the photonic crystal coupling in one of these directions may be stronger than the other. Further TEM measurements are required to determine if this is the case.

The second explanation involves spatial hole burning, where spectral holes in the gain profile may occur across the device due to varying levels of gain saturation. Some regions of a device may be gain saturated for the wavelength satisfying the Bragg condition, whilst other regions may still reach sufficient gain at this wavelength to achieve lasing. Increasing the current could then result in laser action from multiple regions of the device, all of which can achieve sufficient gain at the wavelength satisfying the Bragg condition so that only a single lasing wavelength is observed. This would explain the rise of a second peak in the far-field without the appearance of a second lasing peak in the spectra, however, further experiments are required to confirm if this is the case.

4.5 Threshold current temperature dependence

Consideration of the threshold current temperature dependence also helps indicate the photonic crystal feedback is responsible for laser oscillation. The threshold dependence on photonic crystal period over a range of temperatures and for several devices, is shown in figure 4.14. At 50K low period devices have reduced threshold current densities, and high period devices have increased threshold current densities, with a local minima for a period of 276 nm. At 100K, the low period device has an increased threshold current density, whilst the higher period devices have decreased theirs. Intermediate periods have similar thresholds as at 50K, and still provide a local minima. At 150K intermediate periods have almost doubled threshold values compared with 100K, but still provide a local minima. At 200K the local minima now lies closer to the higher period devices.

Examination of figure 4.14 suggests intermediate period devices are optimal for reduced threshold current density. However, if figure 4.9 is also considered, the detuning between the gain peak and lasing peak is the most likely cause of this reduced threshold.

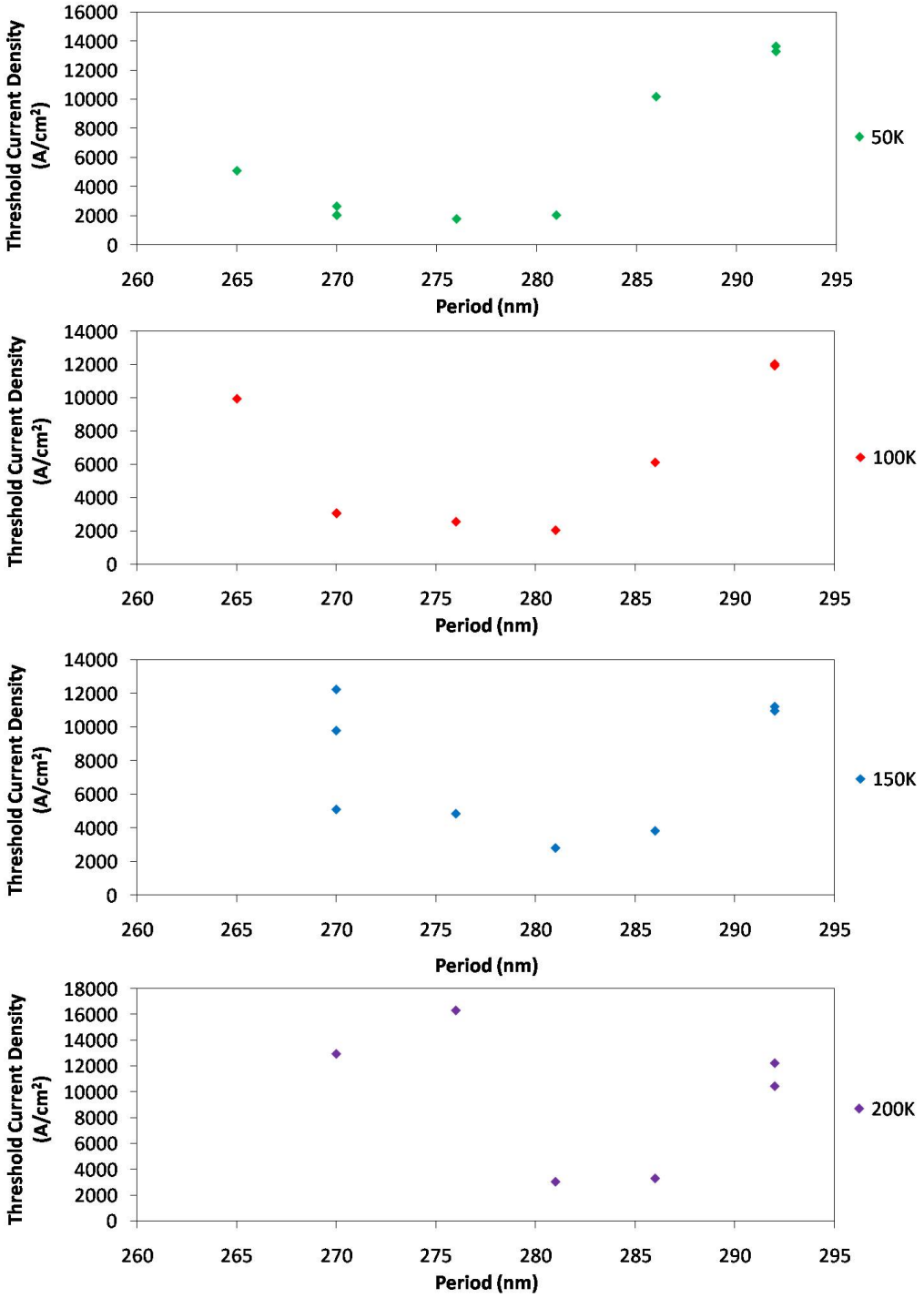

Figure 4.14: Threshold current dependence on period for various devices at 50K, 100K, 150K and 200K.

At low temperatures, a period of a = 276 nm has the smallest detuning and also threshold current density. At 100K this is still true for detuning, however, the threshold is now lowest for a = 281 nm. This can be accounted for by considering inconsistencies in gain peak from one device to the next, and that only spontaneous emission peak one device is plotted in figure 4.9. By 200K the detuning is closest for a = 281 nm, and the threshold minima also occurs at this period.

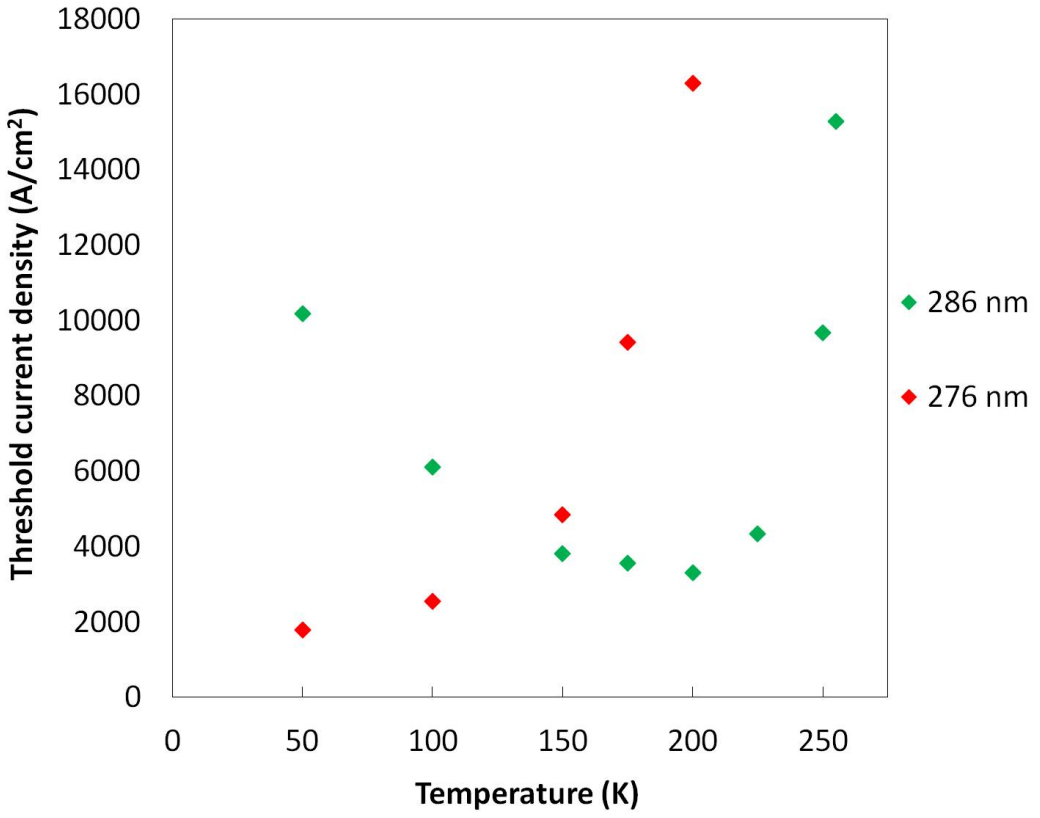

Figure 4.15: Threshold current density as a function of temperature for two PCSELs, periods a = 276, and a = 286 nm.

Figure 4.15 plots threshold current density against temperature for two different period devices. The curves in figure 4.15 are governed by the detuning of the gain and lasing peak. Examination of peak wavelengths in figure 4.9 indicates the detuning for similar period devices to those in figure 4.15. When alignment is good the threshold current is low - for instance, at 200K for the 286 nm period device in figure 4.15. At the same temperature the 276 nm period device has poor alignment and a significantly higher threshold. For all temperatures in figure 4.15 a high threshold occurs when there is high detuning. Similarly a low threshold coincides with a low detuning in figure 4.9. These curves would take a different form if another mechanism were responsible for laser action. For example, if Fabry-Perot feedback were responsible the lasing peak would detune at the same rate as the gain peak. As such, they provide clear evidence that the photonic crystal is producing laser action.

4.6 Conclusions

Low temperature operation of a selection of epitaxially regrown PCSEL devices is discussed, with characterisation of basic operating and emission properties. Laser oscillation is demonstrated and evidence presented that the photonic crystal is responsible. Simple wavelength selectivity of a PCSEL is outlined by changing the operating temperature and manipulating the period. Ther-

mal detuning of gain and lasing peaks is discussed as the key contribution in reducing the threshold current density. Far-field patterns and divergences are presented and indicate values similar to void incorporating PCSELs are possible with an all-semiconductor device. Further work is required to ensure this is true at all currents. Additional work is required to determine the cause of the far-field pattern asymmetry in the two orthogonal directions presented.

References

[1] "Epitaxially regrown GaAs based photonic crystal surface emitting laser" D. M. Williams, K. M. Groom, B. J. Stevens, D. T. D. Childs, R. J. E. Taylor, S. Khamas, R. A. Hogg, N. Ikeda and Y. Sugimoto. Photon. Tech. Lett., **24**, No. 11, 966 (2012)

[2] "All-semiconductor photonic crystal surface emitting lasers based on epitaxial regrowth" R. J. E. Taylor, D. M. Williams, D. T. D. Childs, B. J. Stevens, L. R. Shepherd, S. Khamas, K. M. Groom, R. A. Hogg, N. Ikeda and Y. Sugimoto. IEEE J. Sel. Topics Quant. Electron., **19**, No. 4, (2013)

[3] "Two dimensional distributed feedback lasers and their applications" S. Wang and S. Sheem. Appl. Phys. Lett., **22**, 460 (1973)

[4] "Organic lasers based on lithographically defined photonic-bandgap resonators" M. Berggren, A. Dodabalapur, R. E. Slusher, Z. Bao, A. Timko and O. Nalamasu. Electron. Lett., **34**, No. 1, 90 (1998)

[5] "Laser action from two-dimensional distributed feedback in photonic crystals" M. Meier, A. Mekis, A. Dodabalapur, A. Timko, R. E. Slusher, J. D. Joannopoulos and O. Nalamasu. Appl. Phys. Lett., **74**, No. 1, 7 (1999)

[6] "Coherent two-dimensional lasing action in surface-emitting laser with triangular-lattice photonic crystal structure" M. Imada, S. Noda, A. Chutinan, T. Tokuda, M. Murata and G. Sasaki. Appl. Phys. Lett., **75**, No. 3, 316 (1999)

[7] "Room temperature continuous wave operation of a surface emitting two dimensional photonic crystal laser" D. Ohnishi, T. Okano, M. Imada and S. Noda. Optics Express, **12**, No. 8, 1562 (2004)

[8] Cryostat set-up implemented by David Childs, research associate in the Electronic and Electrical Engineering department at the University of Sheffield.

[9] Basic product information on a TO-5 header of the type used can be found at http://www.siliconfareast.com/to5.htm

[10] Oerlikon leybold vacuum PT 50 pump used. Product information can be found at https://leyboldproducts.oerlikon.com/products /produktkatalog_03.aspx?cid=50_30_0_10

[11] Lakeshore 331 temperature controller used. Product information and technical specifications can be found at http://www.src.wisc.edu/users/scienta_info/Scienta_R4000 /Instruction%20Manuals/Lakeshore%20331.pdf

[12] Hewlett-Packard 70951A optical spectrum analyzer. λ = 600 - 1700 nm range, -85 dBm sensitivity, 60 dB dynamic range.

[13] Hewlett-Packard 8153A lightwave multimeter used. Technical specifications available online at http://www.testwall.com/datasheets/HP-8153A.pdf

[14] Hewlett-Packard 81525A optical head module used. Technical specifications available online at http://www.equipland.com/commerce/catalog /product.jsp?product_id=1008&czuid=1097575701745

[15] Photon Inc. goniometric radiometer LD8900R used. Technical specifications available online at http://www.ophiropt.com/laser-measurement-instruments/beam-profilers/products/goniometer/ld8900-8900r

[16] "Lasers producing tailored beams" E. Miyai, K. Sakai, T. Okano, W. Kunishi, D. Ohnishi and S. Noda. Nature, **441**, 946 (2006)

[17] "A nearly diffraction limited surface emitting conjugated polymer laser utilising a two-dimensional photonic band structure" S. Riechel, C. Kallinger, U. Lemmer, J. Feldmann, A. Gombert, V. Wittwer and U. Scherf. Appl. Phys. Lett., **77**, No. 15, 2310 (2000)

[18] "GaN photonic-crystal surface-emitting laser at blue-violet wavelengths" H. Matsubara, S. Yoshimoto, H. Saito, Y. Jianglin, Y. Tanaka and S. Noda. Science, **319**, 445 (2008)

[19] "Multidirectionally distributed feedback photonic crystal lasers" M. Imada, A. Chutinan, S. Noda and M. Mochizuki. Phys. Rev. B, **65**, 195306 (2002)

[20] "High-power single-mode antiresonant reflecting optical waveguide-type vertical cavity surface-emitting lasers" D. Zhou and L. J. Mawst. IEEE J. Quant. Electron., **38**, No. 12, 1599 (2002)

[21] "Single fundamental-mode output power exceeding 6 mW from VCSELs with a shallow surface relief" A. Haglund, J. S. Gustavsson, J. Vukusic, P. Modh and A. Larsson. Photon. Tech. Lett., **16**, No. 2, 368 (2004)

[22] "High-index-contrast ridge waveguide devices for integrated photonic and optoelectronic applications" ProQuest (2007) D. Liang

[23] Topics in applied physics volume 39: "Semiconductor devices for optical communications" Springer-Verlag 2nd Edition (1982) H. Kressel

[24] "High-power 810-nm GaAsPAlGaAs diode lasers with narrow beam divergence" J. Sebastian, G. Beister, F. Bugge, F. Buhrandt, G. Erbert, H.

G. Hansel, R. Hulsewede, A. Knauer, W. Pittroff, R. Staske, M. Schroder, H. Wenszel, M. Weyers and G. Trankle. J. Sel. Top. Quant. Electron., **7**, No. 2, 334 (2001)

[25] "Waveguide design optimization for long wavelength semiconductor lasers with low threshold current and small beam divergence" A. Al-Muhanna, A. Alharbi, A. Salhi. J. Mod. Phys., **2**, 225 (2011)

[26] "High speed VCSELs for optical interconnects" p65, Springer (2011) A. Mutig

[27] "Quantum control and measurement" Elsevier (1993) H. Ezawa and Y. Murayama. (eBook)

[28] "Lasing band-edge identification for a surface-emitting photonic crystal laser" K. Sakai, E. Miyai, T. Sakaguchi, D. Ohnishi, T. Okano and S. Noda. J. Sel. Areas Commun., **23**, No. 7 (2005)

[29] "Temperature dependence of the energy gap in semiconductors" Y. P. Varshni. Physica, **34**, 149 (1967)

[30] "Photoreflectance and photoluminescence spectroscopy of the lattice-matched InGaAs/InAlAs single quantum well" Y. C. Wang, S. L. Tyan and Y. D. Juang. J. Appl. Phys., **92**, No. 2, 920 (2002)

[31] "Temperature dependence of semiconductor band gaps" K. P. O'Donnell and X. Chen. Appl. Phys. Lett., **58**, No. 25, 2924 (1991)

[32] "Parameter sets due to fittings of the temperature dependencies of fundamental bandgaps in semiconductors" R. Passler. Phys. Stat. Sol. B, **216**, 975 (1999)

[33] "Fabrication and characterization of complex-coupled MQW-DFB laser with an InGaAs absorptive grating" D. K. Oh, M. G. Kim, H. S. Kim, N. Hwang, H. T. Lee and K. E. Pyun. Korean Phys. Society, **34**, 92 (1999)

[34] "Single-mode operation over a wide temperature range in 1.3 μm InGaAsP/InP distributed feedback lasers" H. Lu, C. Blaauw and T. Makino. J. Lightwave Technol., **14**, No. 5, 851 (1996)

[35] "Temperature and wavelength dependence of gain and threshold current detuning with cavity resonance in vertical cavity surface emitting lasers" IET Optoelectron., **1**, No. 5, 206 (2007)

[36] "Designing strategy to enhance mode selectivity of higher-output oxide confined vertical cavity surface emitting lasers" R. P. Sarzala. Appl. Phys. A, **81**, 275 (2005)

5 Room Temperature Characterisation

5.1 Introduction

In this chapter basic room temperature characteristics, including polarisation and far-field patterns, as well as more advanced characteristics of PCSELs are outlined. These advanced characteristics include measurement of the photonic band structure and external feedback effects. Comparison of the experimental band structure with theoretical models is discussed, and from the band structure, the in-plane and out-of-plane coupling coefficients are calculated. In addition, variation of output-coupler reflectivity is used to characterise the effects on the threshold current and output power of a PCSEL operating under external feedback. All measurements in this chapter are made whilst operating under pulsed conditions unless stated otherwise.

5.2 Background

As lasing occurs at the band-edge in a PCSEL, the design of the photonic band structure is key. Band structure engineering is possible through the careful design of the photonic crystal lattice, atom shape and period, giving PCSELs high versatility. As outlined in sections 1.3.1 and 1.3.2, there has been extensive research into modelling the band structure of photonic crystals

through various photonic crystal designs [1–7]. Whilst chapter 4 included results that indicated the emitted light was influenced by the photonic crystal, it is the measurement of the band structure that is able to directly confirm the photonic crystal is responsible. Based on the angularly-resolved photoluminescence method of Astratov *et al.* [8], the coupling of light to the band edges of a photonic crystal can be determined. Sakai *et al.* also used this method to measure the band structure for a void incorporating PCSEL and calculate the coupling coefficients κ_1 and κ_3 [9]. These give a quantitative description of the feedback strength in the photonic crystal plane (κ_3), and the coupling out of the photonic crystal plane (κ_1). The ability to quantitatively define and describe the effects of the photonic crystal is crucial for development of devices such as PCSELs. These characteristics for an all-semiconductor PCSEL operating at room temperature conditions are outlined below. Integration of these devices into more complex applications will also inevitably require the use of optical fibres, mirrors and lenses, all of which are likely to generate external feedback into the PCSEL. Therefore, examination of the effects of feedback on PCSEL characteristics such as output power, EL spectra and threshold current is also required.

5.3 Basic characteristics

5.3.1 Spectra and LI

Figure 5.1a) plots the electroluminescence (EL) spectra below threshold (100 mA or 0.6 I_{th}) and above threshold (250 mA or 1.4 I_{th}) for the lowest threshold device at room temperature. Below threshold two small peaks are clearly evident in the spectra as a result of enhanced emission at the photonic band edges. Above threshold a single lasing peak appears as lasing occurs from only one of the band edges, specifically, the band with the highest quality factor as this is the region with the lowest loss [9]. The low output power of the device is evident from the relative intensity of the noise in the EL spectra. Analysis of the raw output-power against injection current (LI) characteristics indicates that the majority of the power is due to spontaneous emission. The narrow lasing peak has only a small integrated intensity compared to the much broader spontaneous emission peak. Figure 5.1b) plots the spectral LI characteristics. Here the power is measured as the integrated intensity between two wavelengths either side of the photonic crystal peak (956.21 nm $< \lambda <$ 964.61 nm). This reveals the true LI characteristics of the PCSEL allowing measurement of the threshold current (175 mA).

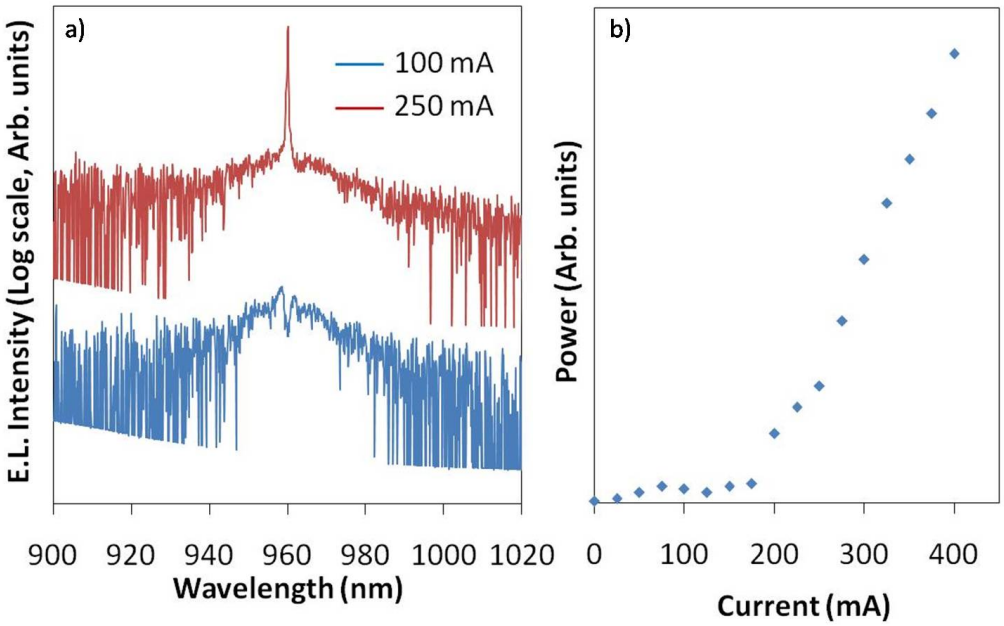

Figure 5.1: Basic room temperature characteristics of a PCSEL: a) Electroluminescence spectra above (1.4 Ith) and below (0.6 Ith) threshold. b) Integrated spectral output-power as a function of current.

As outlined in section 5.4 devices are mounted on gold tiles for band structure measurements. Figure 5.2 plots the EL spectra as a function of current for a typical device (period = 276 nm) before mounting on the tile. The inset to figure 5.2 plots the EL spectra as a function of current for the same device after mounting onto a tile (in the region of the photonic crystal peak). The appearance of the peak has been shifted to higher currents (ΔI = 140 mA) due to this extra processing step. The spectral linewidth of the lasing peak for the same device is plotted as a function of current in figure 5.3.

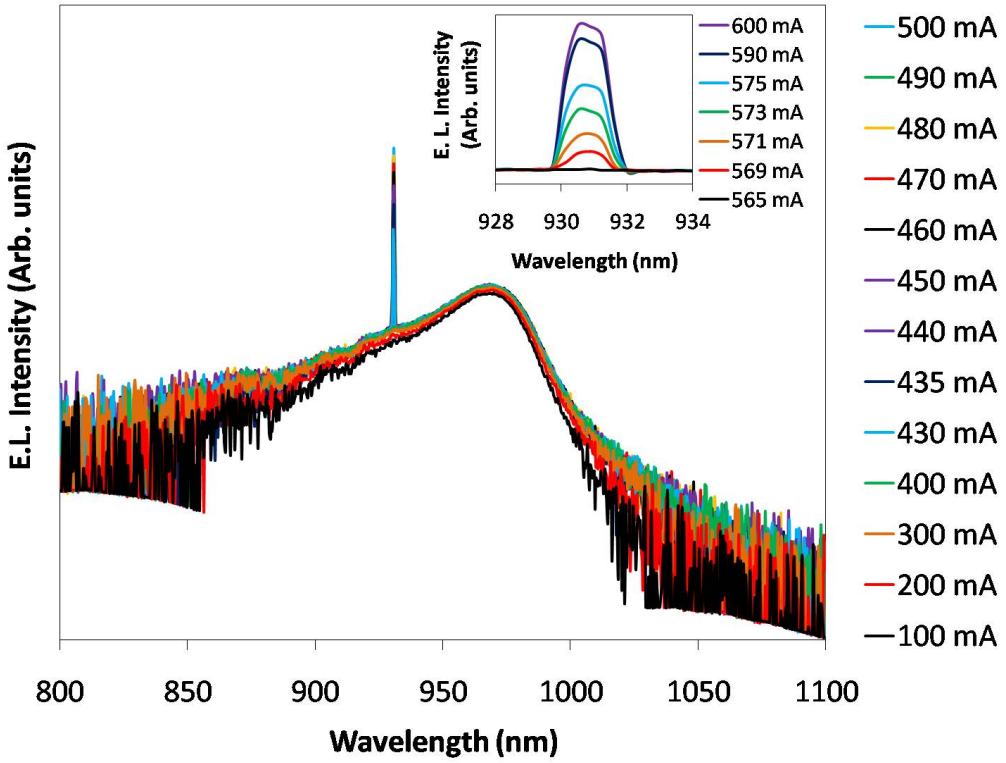

Figure 5.2: Electroluminescence spectra as a function of current. *Inset:* Electroluminescence spectra close to the lasing peak as a function of current after additional device processing.

Figure 5.3 plots the spectral linewidth above threshold as a function of current. A clear linear trend (black line) is observed as the linewidth increases from 0.23 nm to 0.41 nm in the 60 mA current region plotted (just above threshold). A broadening of the lasing peak is observed at higher currents and comparison with the low temperature linewidth in figure 4.7 over the equivalent current range ($I = I_{th} + 60$ mA) yields similar results (0.29 nm to 0.41 nm).

Linewidth broadening is therefore not attributed to thermal effects, but rather that higher currents are allowing the device to access additional states in the photonic band structure. This results in lasing from either: higher wavevector states at the low group velocity band edges; or from multiple band edges at the Γ point. The quality or q-factor of this PCSEL is calculated using 5.3.1, and is plotted in figure 5.3 *inset*, as a function of current. Typical Q-factors for sub-threshold void-incorporating PCSELs are band dependent, for example, $Q_a = 1700$, $Q_b = 1000$, $Q_{c,d} = 500$ in [9], where bands a, b, c and d correspond to those labelled in figure 5.9. Using 5.3.1 an approximate above threshold Q-factor of the lasing peak is calculated as 4800 for [9].

$$Q = \frac{\lambda}{\Delta\lambda} \tag{5.3.1}$$

The data in figure 5.3 *inset* is produced from the linewidth values in figure 5.3 and the lasing peak wavelength. The Q-factor clearly decreases with current as the linewidth broadens. Q-factor values for this all-semiconductor PCSEL (just above threshold) are only slightly reduced in comparison to those calculated for void incorporating devices. From low temperature EL spectra, sub-threshold linewidths of 0.55 nm were obtained (figure 4.7), yielding Q-factors of 1700 similar to the reported value of Q_a. For similar devices operating at room temperature, a range of cold linewidths of 1.7-2.3 nm were

achieved (defined in section 4.3). This gives Q-factors of 430-580 for the doubly degenerate high energy bands. These are similar to the degenerate high energy bands of a void incorporating PCSEL ($Q_{c,d}$ = 500) at 0.9 I_{th}. The high uncertainty in Q-factor arises from the low linewidth values being used in 5.3.1.

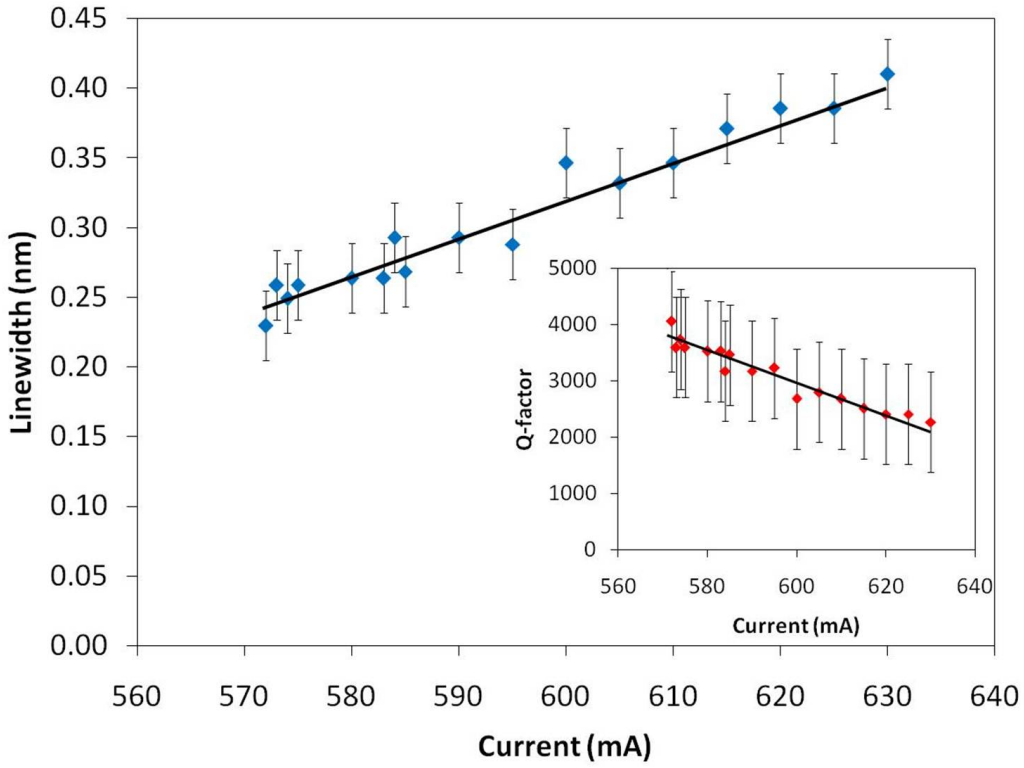

Figure 5.3: Spectral linewidths as a function of current. *Inset:* Q-factor as a function of current. Black lines indicating the general linear trends.

5.3.2 Polarisation

The polarisation of a PCSEL is determined by the electric and magnetic field vectors of the light propagating through the photonic crystal. The design of the photonic crystal allows for tunability of the polarisation of the emission. Modelled in figure 1.10a) and b), the magnetic field vectors indicate that emission from TE bands 2 and 3 should have linear polarisation, whilst TE bands 4 and 5 should have a more complex polarisation.

Figure 5.4 plots the variation in power (at a fixed current) as a function of linear polariser angle relative to the (100) crystal direction (rotating in a clockwise direction). Power is transmitted when the polariser is aligned with the Γ-X direction, with parallel magnetic field vectors to the (100) direction, and is reduced to zero when rotated to 90°. The power in figure 5.4 is normalised so that minima in the raw output power are equal to zero and maxima are equal to one. This is an attempt to remove the effect of background spontaneous emission, however, this is more accurate using the spectral polarisation data (see figure 5.5 *inset*). The fluctuation in spectral peak intensity follows a very similar trend to that in figure 5.4 indicating that this normalisation is sufficiently accurate.

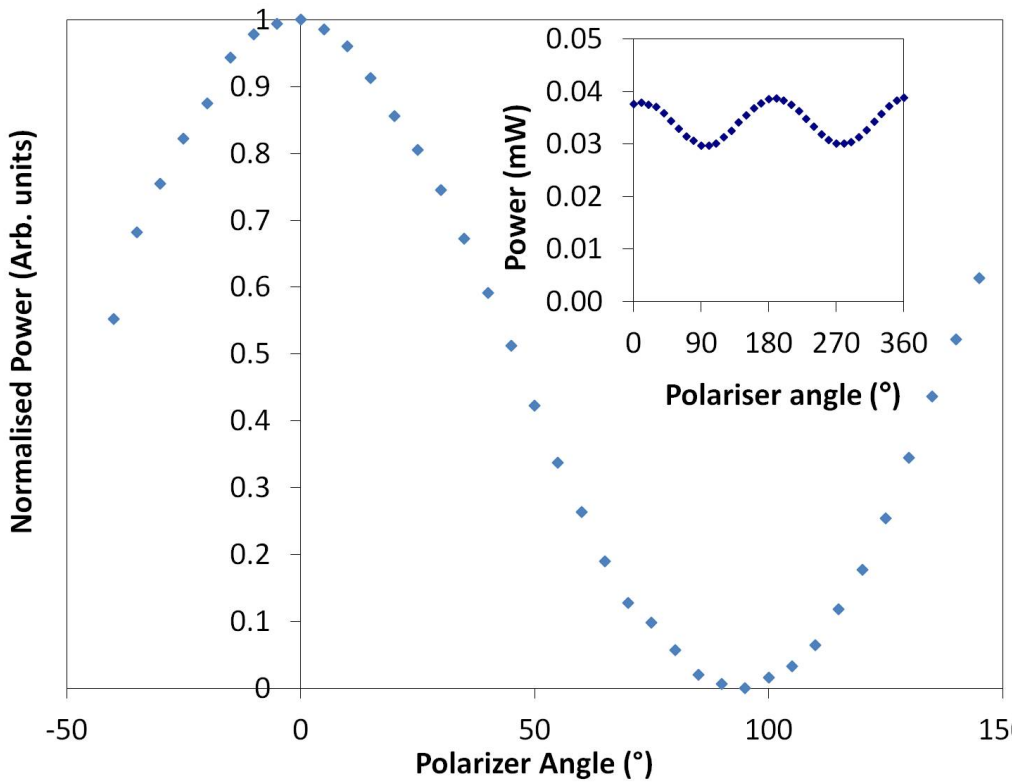

Figure 5.4: Normalised output power as a function of polariser angle. *Inset:* Raw output power as a function of polariser angle.

Figure 5.4 *inset* indicates the raw power variation as a function of polariser angle, clearly indicating that not all the emission is linearly polarised. The random polarisation of the spontaneous emission is responsible for the measured output power when the lasing peak is completely polarised. From these power measurements, an extinction ratio of 23.5% (ratio of lowest trough to highest peak) is determined. Typical room temperature measurements produced polarisation extinction ratios slightly less than this, varying from 16%

to 23.5% from one device to another. Some variation is expected due to the nature of the random polarisation of spontaneous emission.

The intensity variation of the EL spectra (near the lasing peak) as a function of polariser angle is plotted in figure 5.5. At the polariser angles where low power is measured in figure 5.4, the lasing peak in figure 5.5 is clearly reduced in intensity. Spectra for a selection of angles have been plotted to illustrate the variation in intensity. To aid the eye, polariser angles with similar powers (from figure 5.4) are also plotted using similar colours. Figure 5.5 *inset* plots the EL intensity of the lasing peak against polariser angle, clearly indicating the angles (90-95° and 270-275°) where the photonic crystal peak is reduced to zero intensity. Note that peak intensities have been included for spectra not plotted in figure 5.5 to avoid overcrowding of the graph. Figure 5.5 *inset* indicates the peak intensity at 0° is lower than at 180° and 360°. The peak intensity at 0° is close to that at 30° so the EL spectra of 0° is hidden behind that of 30°. This discrepancy is due to slight misalignment of the polariser when adjusting by hand so that it is not parallel to the surface of the device. Similar levels of intensity are observed for the spontaneous emission at wavelengths close to the lasing peak for all polariser angles. At angles of high polarisation there is a large amount of noise but the lasing peak is just visible using a logarithmic scale.

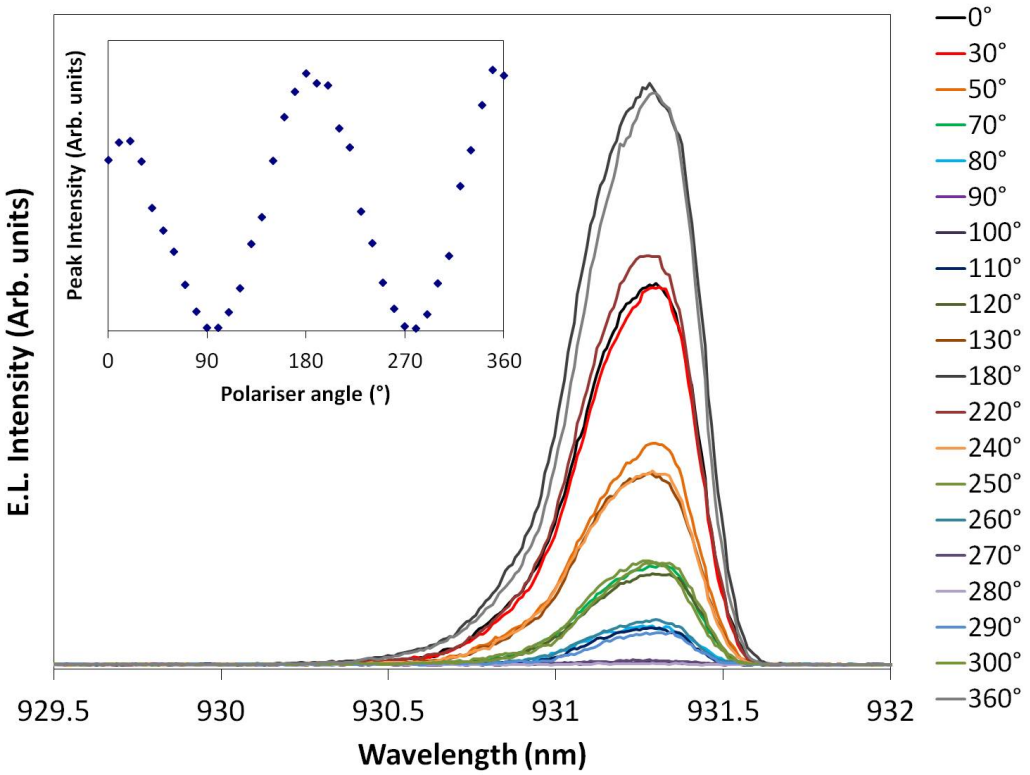

Figure 5.5: Electroluminescence spectra at wavelengths close to the lasing peak for varying degrees of polarisation. *Inset:* Variation in peak intensity with polariser angle.

5.3.3 Far-field pattern

As discussed in chapter 4, low divergence angles possible in a PCSEL far-field pattern are part of what makes them attractive for high brightness applications. Figure 5.6 plots a typical device room temperature far-field pattern as a function of current. At room temperature the device is not mounted in the cryostat chamber and the goniometer is able to take measurements from closer

to the sample. Measurements plotted in this chapter are taken from a distance of 5 mm from the sample surface.

Figure 5.6 plots the far-field pattern cross-section in the $\theta = 0°$ orientation (defined in figure 4.2), with a single central peak observed at all currents. Figure 5.6 *inset* plots the far-field peak at 380 mA, which has been normalised once the spontaneous emission is removed.

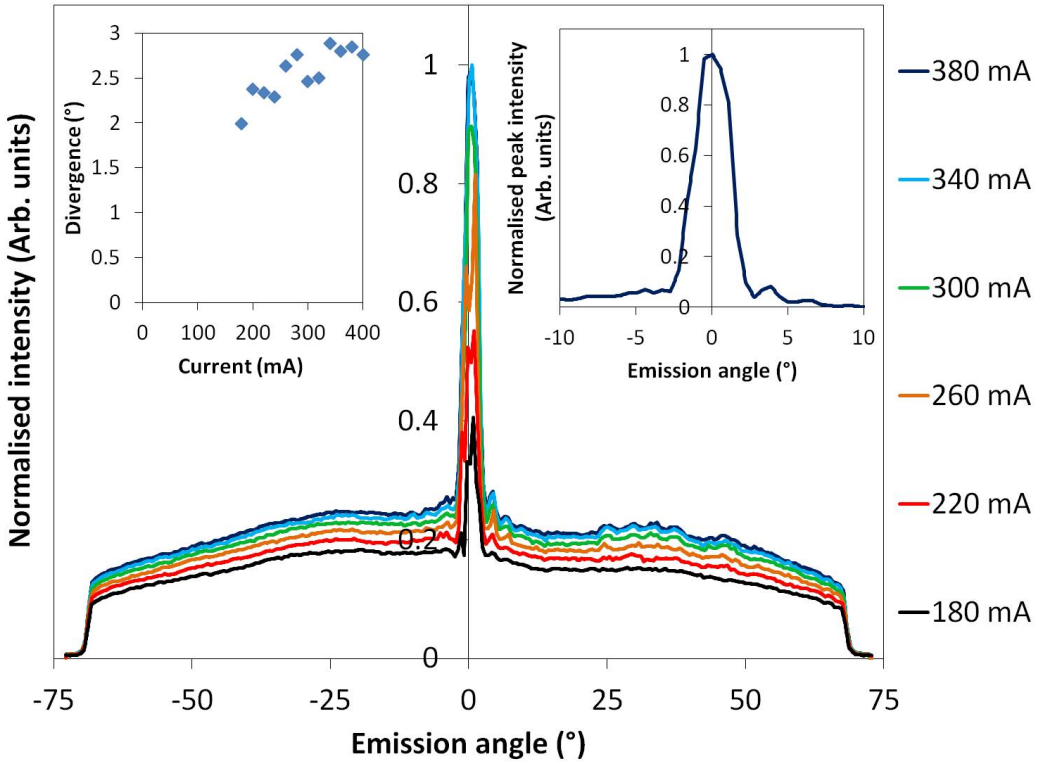

Figure 5.6: Far-field cross-section in the $\theta = 0°$ orientation as a function of current. *Inset:* Far-field at 380 mA with background spontaneous emission removed and divergence as a function of current.

Taking the full width half maximum (FWHM) of this peak at each current gives the divergence of the lasing peak, also shown in figure 5.6 *inset*. The scatter of divergences at the currents considered here makes it difficult to determine if there is any real dependence on current.

Figure 5.7 plots the far-field cross-section in the 90° orientation. In this case two peaks are observed but are not fully resolved at all currents. The FWHM dependence on current is plotted *inset* in figure 5.6 and figure 5.7 for the $\theta = 0°$ and $\theta = 90°$ orientations respectively. For $\theta = 90°$ the divergence is harder to calculate as the two peaks are not resolved at the half maxima value. Figure 5.7 *inset* indicates that at low currents the two peaks can be resolved, and that both have similar divergences. These divergence values are also similar to that in the $\theta = 0°$ orientation, however, there is a slightly larger scatter. In both orientations there is no obvious dependence on current (at low currents). At higher currents the $\theta = 90°$ divergence jumps up to over 10° when the peaks are no longer resolvable. This behaviour is similar to that observed in figure 4.13. In figure 4.13 one orientation started with low divergence, and then increased as a second peak was observed at higher currents. However, in figure 5.7 the two peaks appear simultaneously and continue to increase at the same rate, making the jump from low to high divergences more distinct.

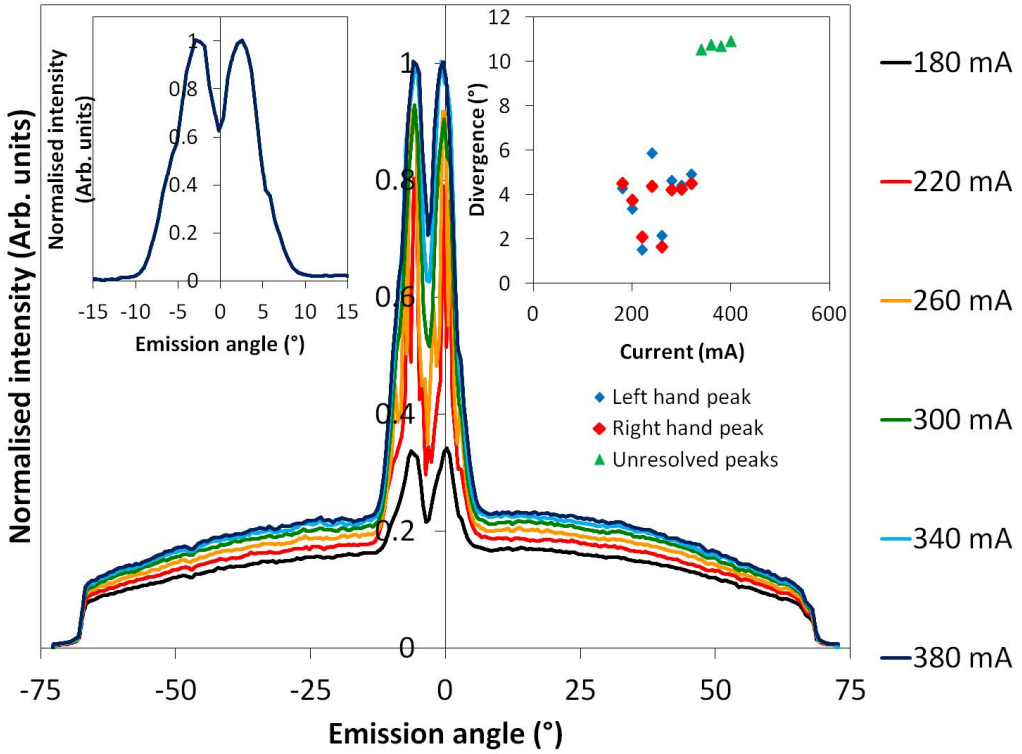

Figure 5.7: Far-field cross-section in the $\theta = 90°$ orientation as a function of current. *Inset:* Far-field at 380 mA with background spontaneous emission removed and divergence as a function of current.

The cross-sections of the far-field pattern are taken in orthogonal directions but both are parallel to one of the symmetric Γ-X photonic crystal directions. The asymmetric nature of the far-field pattern is therefore likely to be an attribute caused by fabrication of the photonic crystal within the device. From figure 3.11c) it was clear that the infill of the photonic crystal required growth conditions that caused difficulty in achieving planarisation of the upper GaAs-

AlGaAs interface. The modulation in this layer is likely to be asymmetric in the two orthogonal directions (which lie parallel to the Γ-X directions) due to the inequivalence of the different (110) crystal directions, and this would likely result in an asymmetric far-field pattern.

5.4 Band structure characterisation

Figure 5.8 is a schematic of the set-up used to measure the EL spectra of a PCSEL from the various angles necessary to construct the band structure. The device under test (DUT) is mounted on a gold tile which can be fixed to a θ-ϕ rotating stage, and fine control of these two angles is achieved through a computer controlled motor. From the initial starting point in figure 5.8, rotation occurs in the θ direction to measure the band structure in the Γ-X direction. Rotation of the DUT in the ϕ direction by 45°, followed by similar θ rotations, allows measurement in the Γ-M direction. Alternative lattices require measurement at different ϕ angles depending on the symmetrical crystal vectors. The optical fibre (MMF) is fixed to an x-y-z stage for alignment with the DUT and the optical spectrum analyser (OSA) records the EL spectra at each angle.

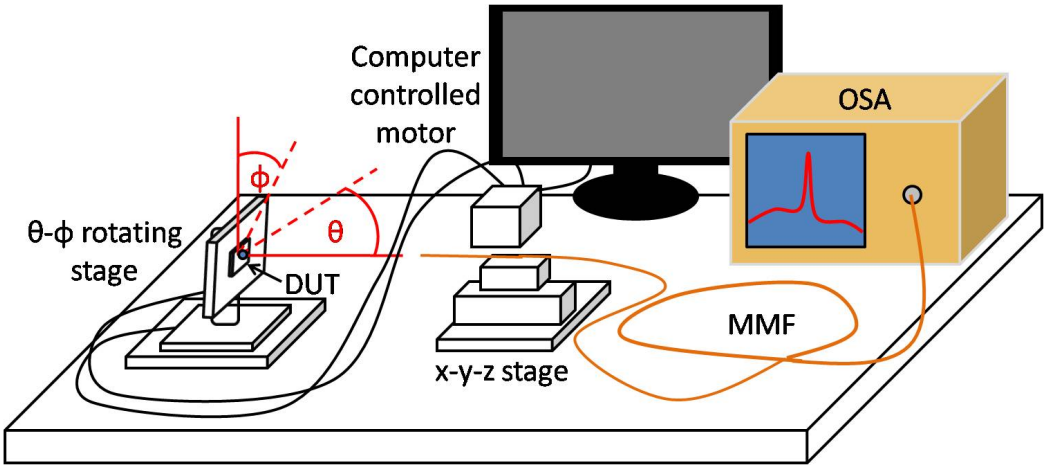

Figure 5.8: Schematic indicating the experimental set-up used to measure the photonic band structure.

A contour plot of the sub-threshold spectra yields the variation of the emission with frequency and angle, highlighting the shape of the band structure (figure 5.9). Comparison with a plane wave expansion model of a square lattice photonic crystal (overlaid in black in figure 5.9), indicates there is a strong correlation between the two, and hence, that emission is controlled by the photonic crystal within the device. The coupling coefficients κ_1 and κ_3 (see section 1.2.2) are found from the angular frequencies of the photonic crystal peaks at the Γ point using 5.4.1-5.4.3 [10].

$$\omega_a = \frac{c}{n_{ave}}(\beta_0 - \kappa_3)\left(1 - \frac{8{\kappa_1}^2}{{\beta_0}^2 - {\kappa_3}^2}\right) \tag{5.4.1}$$

$$\omega_b = \frac{c}{n_{ave}}(\beta_0 - \kappa_3) \tag{5.4.2}$$

$$\omega_{c,d} = \frac{c}{n_{ave}}(\beta_0 + \kappa_3)\left(1 - \frac{4{\kappa_1}^2}{{\beta_0}^2 - {\kappa_3}^2}\right) \tag{5.4.3}$$

where c is the speed of light, n_{ave} is the average refractive index of the waveguide and $\beta_0 = 2\pi/\mathrm{a}$ (a is the period of the photonic crystal).

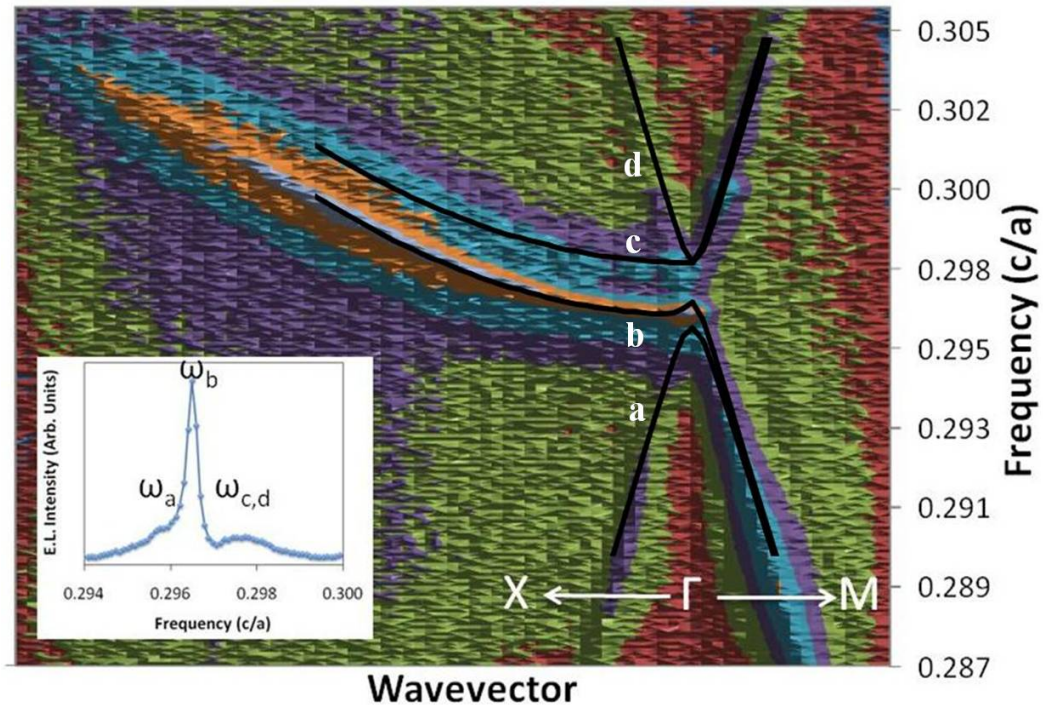

Figure 5.9: Contour plot of sub-threshold, angularly-resolved spectra in the Γ-X and Γ-M directions, with part of the modelled band structure overlaid to indicate TE bands a, b, c, d. *Inset:* Integrated electroluminescence spectra for $\Gamma \pm 3°$.

Waveguide modelling yields a value for the average refractive index as n_{ave} = 3.36. Using 5.4.1-5.4.3 and the frequencies of the peaks *inset* in figure 5.9, coupling values of $\kappa_1 = 3920 \pm 140$ cm^{-1} and $\kappa_3 = 560 \pm 20$ cm^{-1} are determined. Previously reported coupling values are higher than achieved here, with $\kappa_1 = 4300$ cm^{-1} and $\kappa_3 = 740$ cm^{-1} for a void incorporating PCSEL [10]. This is to be expected due to the higher refractive index contrast between voids (assumed to be air) and semiconductor, but the coupling is still sufficient for our devices to achieve lasing. The value of κ_3 is just under half that predicted by the waveguide modelling in section 2.5, which assumed an averaged refractive index of the photonic crystal layer from test patterns and vertical etch profiles.

The grating profile in one-dimensional structures such as DFB lasers is known to affect the coupling coefficient [11], and this is expected to be no different for a photonic crystal, but the analysis is much more complicated. Figure 5.10a) is a contour plot of the coupling coefficient for a 2nd order, one-dimensional trapezoidal grating such as in figure 5.10b) with waveguide parameters outlined in [11]. Variations in coupling are shown depending on the width of the base (W_G/Λ) and top (W_T/Λ) of the grating profile shown in figure 5.10b). Whilst the coupling values shown on figure 5.10a) correspond to a specific waveguide considered in [11], the shape of the contour plot reveals

information on the dependance of the relative strength of the coupling on the grating profile. Two regions of high coupling are observed for gratings with ($W_G/\Lambda = 0.25$, $W_T/\Lambda = 0.75$) and ($W_G/\Lambda = 0.75$, $W_T/\Lambda = 0.25$). A region of low coupling occurs for grating profiles with values of W_G/Λ and W_T/Λ that are similar. Assuming the cross-section TEM images of the photonic crystal layer in figure 3.11 can approximate a one-dimensional grating, the corresponding coupling within these devices is marked by a red cross on figure 5.10a). The location of the cross indicates that the coupling coefficient should be near maximal value for a grating profile such as in the TEM of figure 3.11c).

Two-dimensional photonic crystal modelling methods such as the plane wave expansion method (PWEM) typically assume that the crystal has a constant dielectric medium in the z-direction in order to simplify analysis. This prevents consideration of the grating profile. However, the coupling equations above (5.4.1-5.4.3), can be used in conjunction with the theoretical band structures to model the coupling coefficients for various crystal structures. By varying the crystal structure, and plotting the theoretical band structure as a function of the fill factor, the effect of grating profile on coupling coefficient can be approximated. Figure 5.11 plots the coupling coefficient κ_3, for a type II square lattice photonic crystal, modelled with circular atom shapes of varying radii [12].

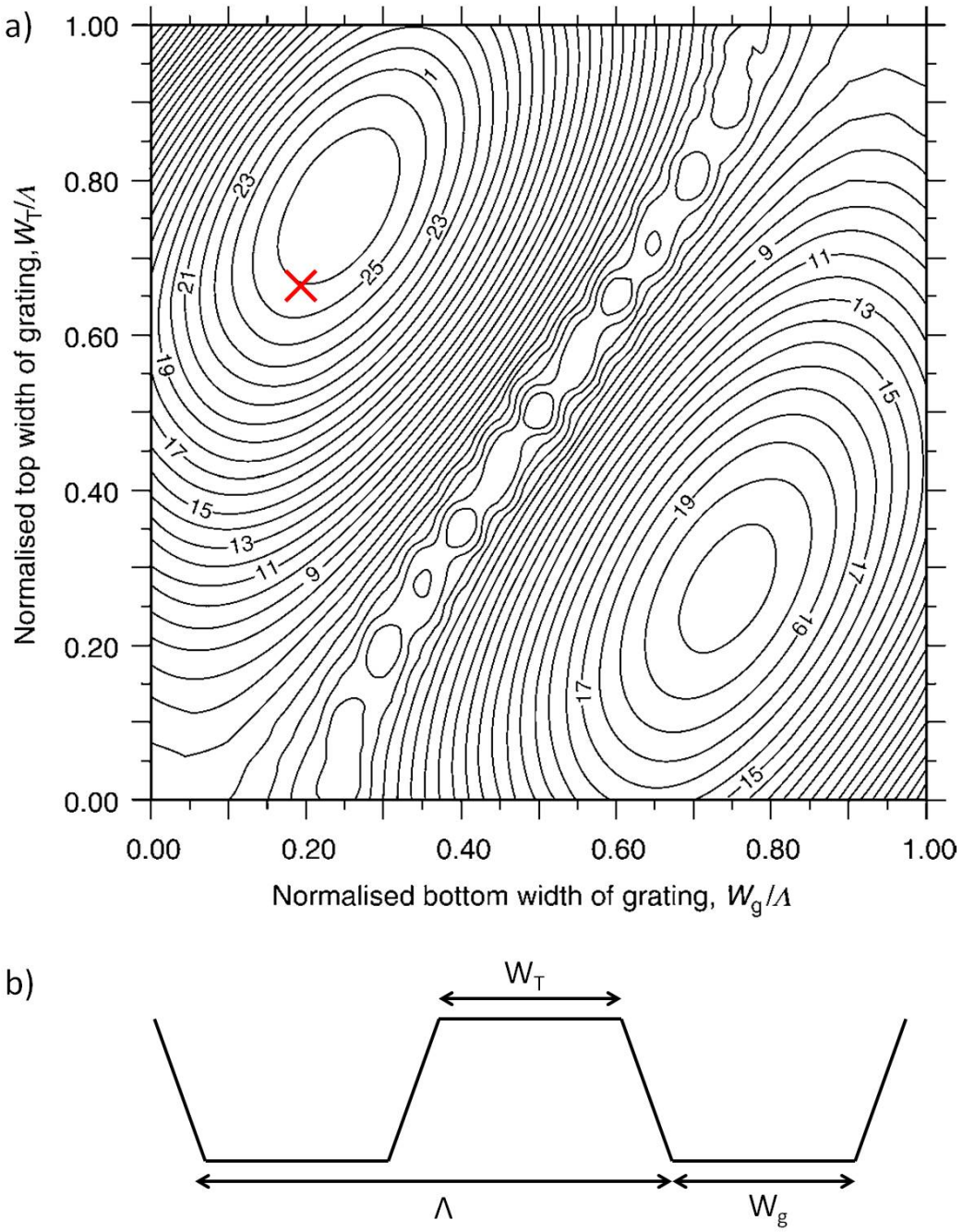

Figure 5.10: a) Contour plot of the coupling in a 2nd order DFB grating with variation in width of the base and top of the trapezoidal profile. Red cross indicates location of our PCSEL from TEM image cross-sections. b) Grating profile of the DFB considered. *Reproduced from* [11].

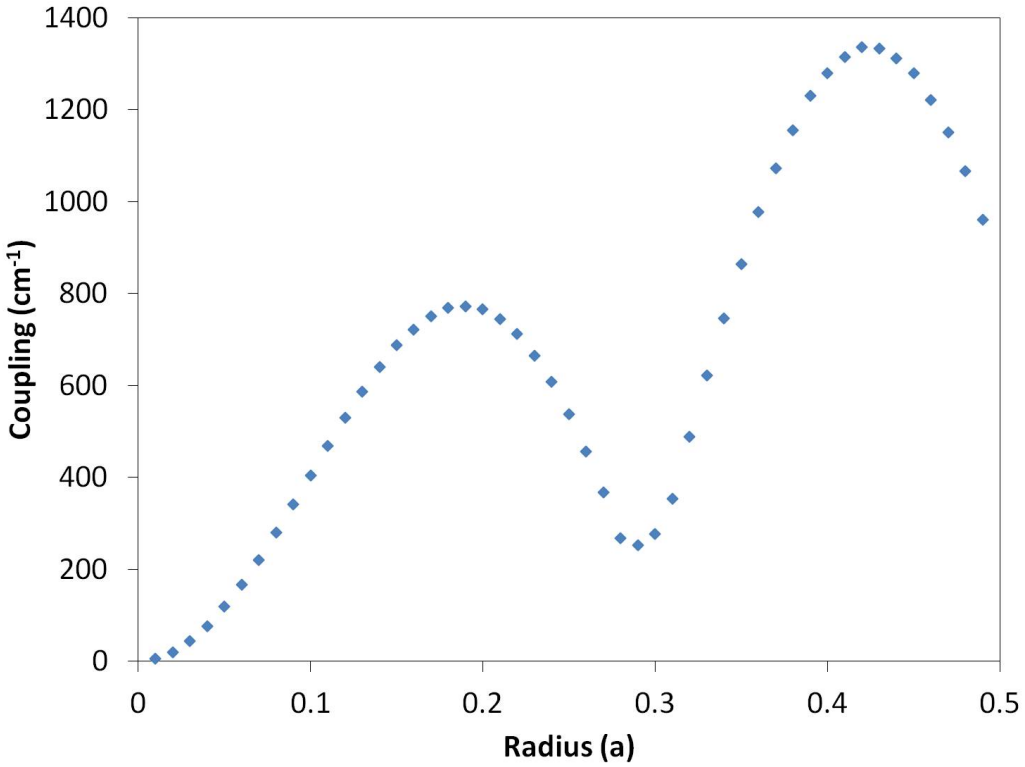

Figure 5.11: Modelled coupling coefficient (κ_3) as a function of atom shape radius. *Courtesy of R. J. E. Taylor of the University of Sheffield.*

In this case, equations 5.4.1 - 5.4.3 have been adapted to use the modelled band frequencies (at the Γ point) to calculate the in-plane coupling coefficient κ_3 (this method can also be used to model κ_1) [14]. The in-plane coupling (κ_3) has two local maxima at radii of 0.19a and 0.42a and this type of dual-peak behaviour has also been modelled elsewhere [6, 13]. From the top of the feature sizes in the TEM image in figure 3.11c) the circular atom shapes have a radius of 0.17a, putting them close to the top of the smaller of the two

peaks in κ_3 with a coupling of approximately 750 cm^{-1}. However, the bottom of the features have a much smaller radius (0.1a), which gives a coupling of approximately 400 cm^{-1}. The band structure measurement of $\kappa_3 = 560$ cm^{-1} is attributed to a result of the shape of the grating features and the disparity of the modelled coupling values for each size feature.

5.5 External feedback characterisation

External feedback can be problematic for integration of lasers in certain applications, however, some devices such as vertical external cavity surface emitting lasers (VECSELs) require external feedback to operate. VECSELs are designed to use an output coupler to create sufficient feedback for lasing and characterisation of the feedback levels involves varying the reflectivity of the output coupler. The effect of variation in feedback levels on threshold current, output power and single pass gain in a VECSEL have previously been investigated [15, 16]. Figure 5.12 plots the LI characteristics of a 100 μm diameter electrically-pumped VECSEL for varying reflectivities. Low threshold currents are achieved at high reflectivity, whilst higher slope efficiencies are measured at intermediate reflectivities. Figure 5.12 *inset* shows the variation in maximum power at different reflectivities whilst under pulsed and continuous wave operation.

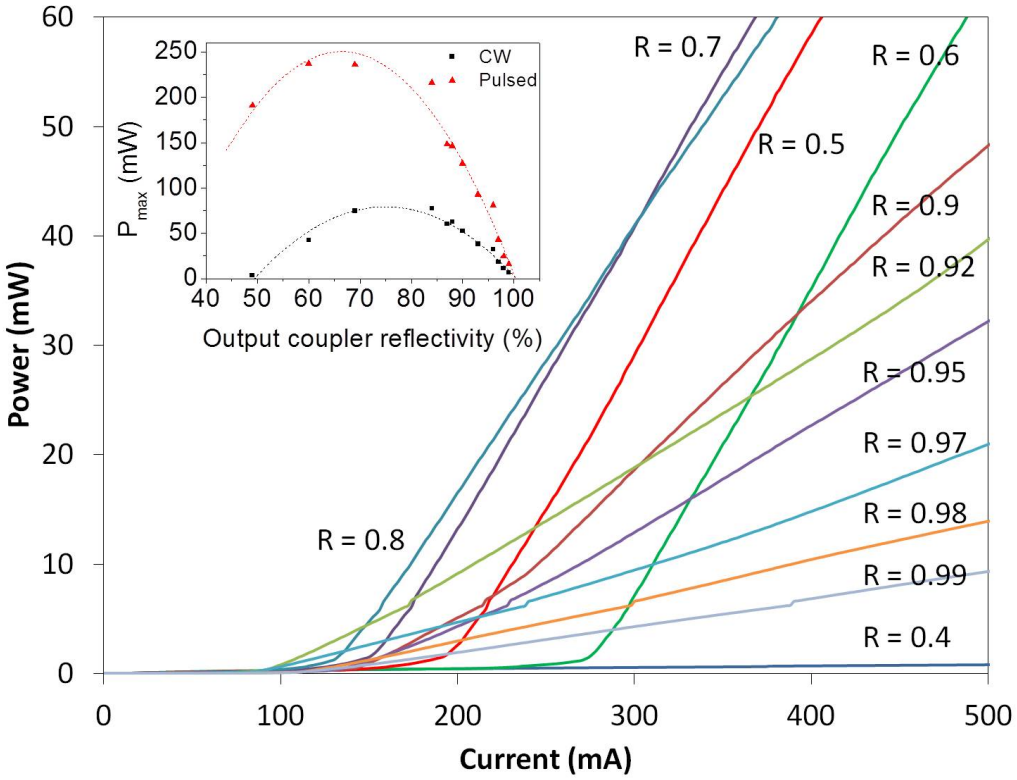

Figure 5.12: LI curves for various output coupler reflectivities in a VECSEL. *Inset:* Maximum output power as a function of reflectivity [15].

Characterisation of such devices is important to ensure the optimum output coupler reflectivity is chosen for the relevant application. VECSELs manipulate distributed Bragg reflectors (DBRs) to generate a cavity in the vertical direction and typically have a very high reflectivity on the lower DBR (>99.99%). This ensures external feedback significantly contributes to the round trip gain within the cavity. PCSELs do not always contain DBRs, making use of the photonic crystal to achieve both lasing and diffraction into the

vertical direction. In such PCSELs, half the emission is lost out the bottom of the device, and any external feedback effect on the emission is immediately reduced by at least half.

Figure 5.13 illustrates the set-up used to characterise the effects of external feedback for the VECSELs in [15, 16] and for the PCSELs discussed below. A collimating lens guides emission to the plane mirror (or output coupler), which is held in a mount that can be tilted in two directions to ensure emission is fed back through the device aperture. Output power or EL spectra are measured by interchanging the alignment of the powerhead or the decollimating lens and multimode fibre (MMF) above the output coupler.

Output coupler reflectivities are determined by the thickness of dielectric layers deposited on the surface, and the transmission response of the dielectric is spectrally dependent. Manufacturer information for each output coupler is used to determine the effective reflectivity at the emission wavelength determined by the Bragg condition for each device [17]. The output coupler will have varying reflectivity for the spontaneous emission due to the broad peak in the EL spectra. The narrow lasing peak has a small uncertainty in wavelength and therefore the effective reflectivity can be considered constant at this wavelength.

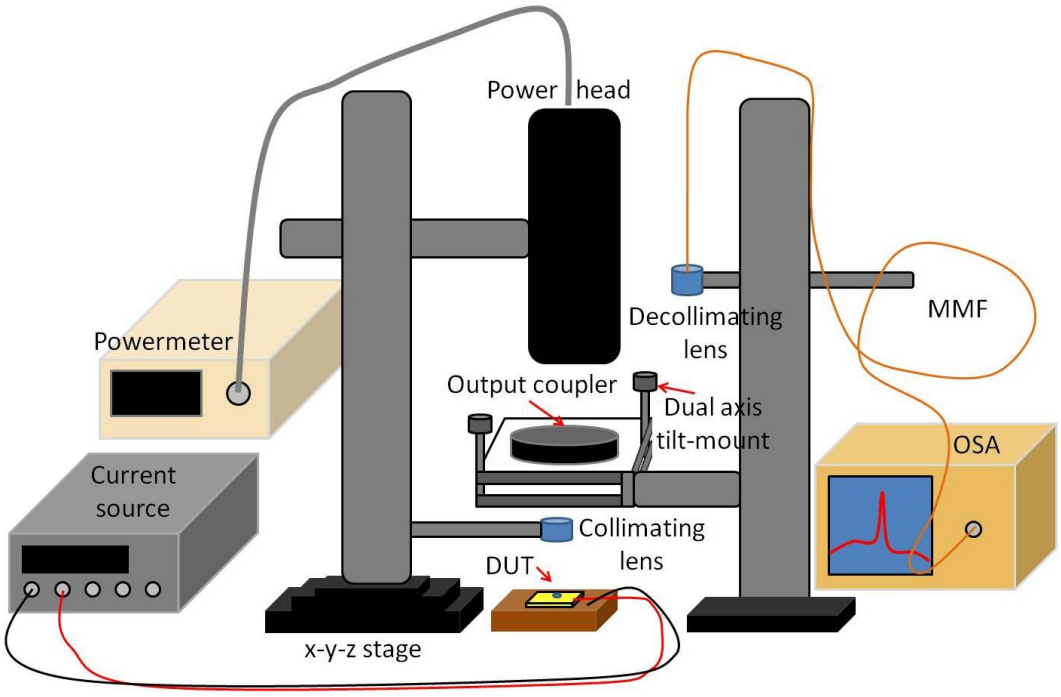

Figure 5.13: Schematic of the external feedback test set-up.

For external feedback to contribute to the laser oscillation, the reflected light must satisfy the Bragg condition in order to enhance the coupling of the photonic crystal. Light at other wavelengths will not couple to the photonic crystal and therefore will not significantly contribute to the feedback within the device. As seen from the polarisation characteristics, the power from the photonic crystal is relatively low (approximately 20% of the total output power) and this is also evident from the narrow spectral peak - a relatively small part of the EL spectra in figure 5.2. The strength of the external feedback is governed by the intensity of the initial output power, the various losses in

the external cavity and the coupling of reflected light back into the photonic crystal. The out-of-plane coupling of the photonic crystal, κ_1, determines the effects of external feedback as light is coupled back into the photonic crystal.

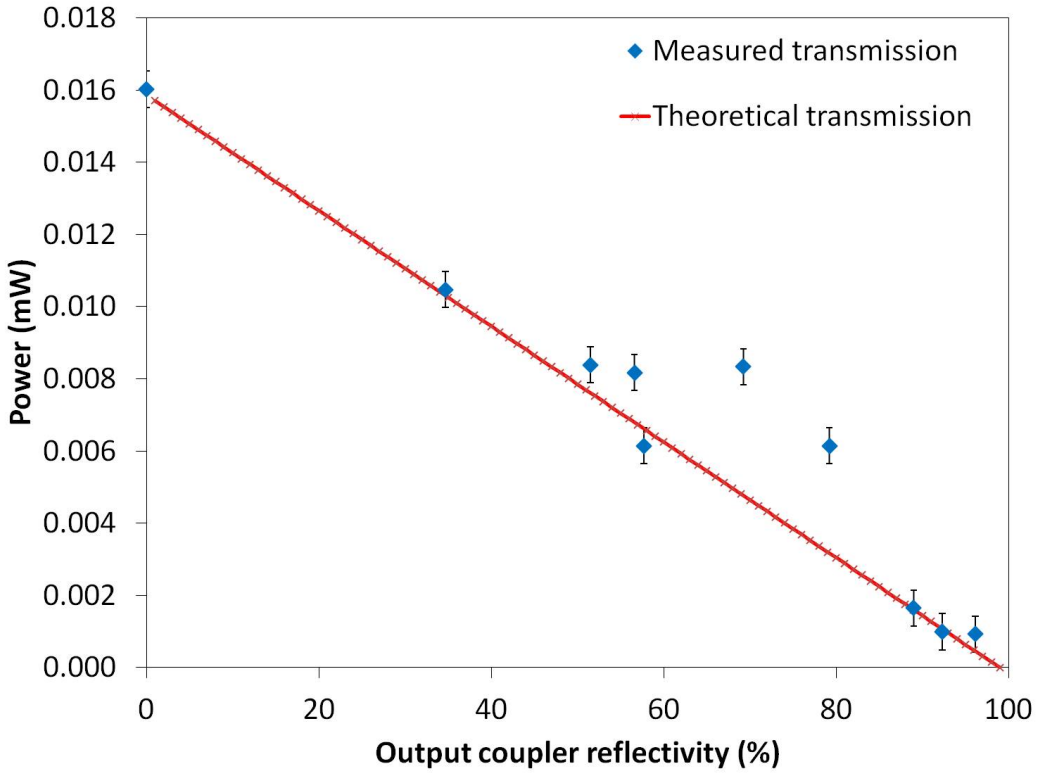

Figure 5.14: Measured and theoretical output powers as a function of output coupler reflectivity.

Figure 5.14 indicates the variation in output power (measured at a fixed current) with output coupler reflectivity, and a simple linear reduction is observed across the reflectivities considered. Only output powers measured at 69.2% and 79.2% show significant deviation from the theoretical transmission.

These slight fluctuations in the measured output power are accounted for by considering the broad spectral spontaneous emission peak, and the variation of spectral response between output couplers. Also, the loss in each output coupler is not identical. The overall reduction in power is explained by the output couplers acting as attenuators. Hence, if they are not creating an external feedback affect on the PCSEL, there is reduced transmission (T) through the output coupler as the reflectivity (R) is increased. Taking the power measured without an output coupler as the maximum power (P_{max}) that can be transmitted, theoretical output power (P_{theory}) values are calculated as a fraction of this maximum power using 5.5.1.

$$P_{theory} = P_{max}T = P_{max}(1 - R - \alpha) \tag{5.5.1}$$

where $\alpha = 0.01$ is assumed to be an arbitrary fixed loss in each of the output couplers. Theoretical values of the power transmitted through the output coupler are also plotted in figure 5.14, and these have close correlation to the measured powers. External feedback appears to have had little or no affect on the output power of the device. However, inspection of the spectra was required to determine threshold accurately in section 5.3.1 due to the relatively low power of the lasing peak, and this should also be considered here.

Figure 5.15 plots the EL spectra close to the lasing peak as a function of

reflectivity, with relative intensities normalised against the spectral peak when no output coupler is present. Measured at a different time to the output powers in figure 5.14, but using the same alignment process, an increase in the spectral peak is clearly observed at reflectivities of 56.6%-69.2%. High reflectivity measurements reveal little useful information about the spectral response due to the low amount of transmission. At other reflectivities, however, the peak intensity appears to drop in a similar fashion as the output powers in figure 5.14. The slight increase of output power and the more obvious increase in spectral peak intensity at certain reflectivities suggests that external feedback is increasing the in-plane feedback of the photonic crystal, but that alignment is critical.

Figure 5.15 *inset* plots the variation in normalised peak intensity against reflectivity, indicating the clear increase in peak intensity for reflectivities close to 60% (reflectivities determined at the wavelength satisfying the Bragg condition). The lasing peak appears to have doubled in size for certain feedback conditions. The lack of response to feedback at other reflectivities is likely due to poor alignment so that the return trip light is not fed directly back into the device.

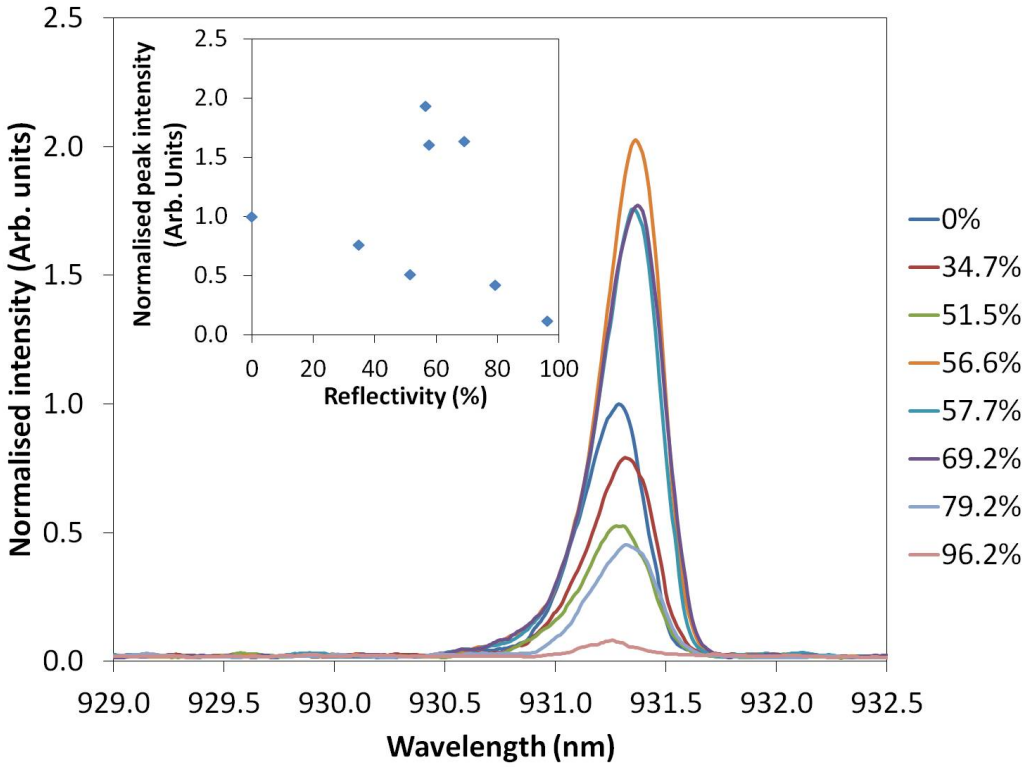

Figure 5.15: Normalised EL spectra close to the lasing peak as a function of reflectivity. *Inset:* Normalised spectral peak intensity as a function of output coupler reflectivity.

Feedback affects on the threshold current are also difficult to determine due to the low power of the devices at room temperature. Figure 5.16 indicates that there is no clear correlation of output coupler reflectivity on threshold current as measured from the raw output power LI curves.

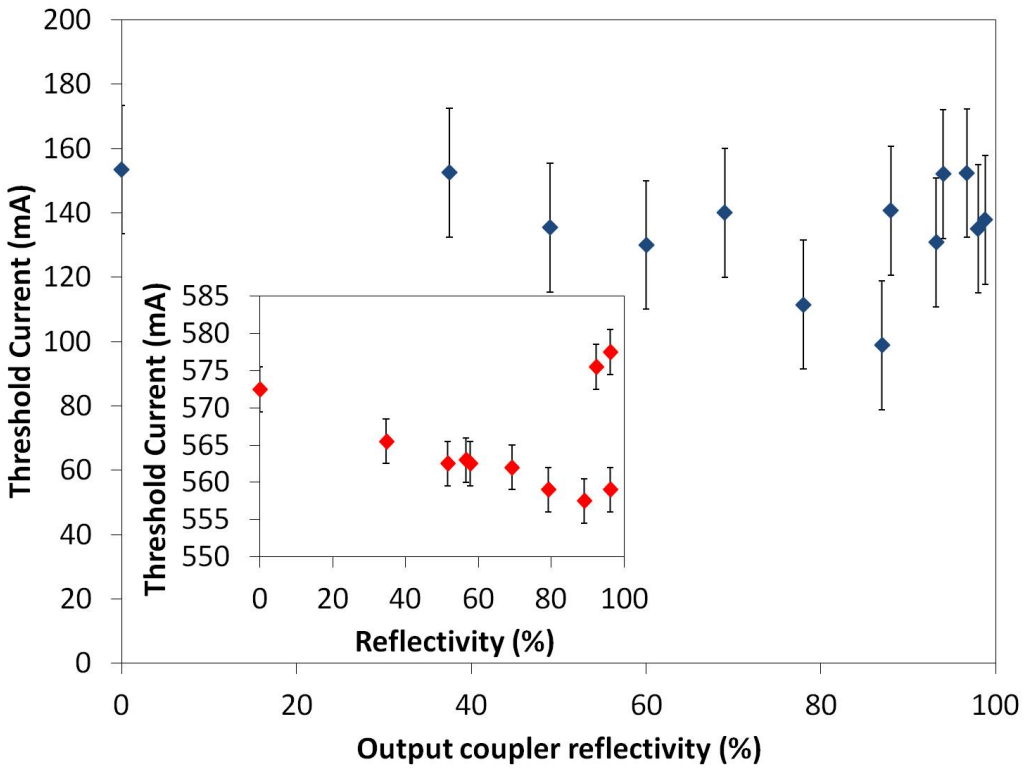

Figure 5.16: Threshold current as a function of output coupler reflectivity *Inset:* Spectral threshold current against reflectivity for a different device.

At 87.0% reflectivity there is a 35.6% reduction in threshold current, but at higher reflectivities thresholds are similar to without feedback. However, the low LI slope efficiency for the device in figure 5.16 results in significant extrapolation to measure the threshold current, as evident by comparison with the value of the spectral LI threshold currents of another device (figure 5.16 *inset*). Such a large reduction in the value of the threshold current is due to the high uncertainty from extrapolating the LI curve. This is also indicated by the

large scatter of points on the graph. The spectral threshold current, however, shows a shallow, linear reduction in value as the reflectivity is increased up until 92.3%. Above this, the low transmission through the output coupler results in threshold values of similar or higher values as achieved without feedback. At a reflectivity of 89.0% a 2.6% reduction in threshold current is achieved. Whilst there appears to be a correlation between threshold current and feedback from the spectral LI curves, the reduction is low, indicating the feedback affect is weak.

5.6 Conclusions and future work

Basic room temperature characteristics have been illustrated, including EL spectra, LI, and threshold currents. In addition, linear polarisation of the emission, with an extinction ratio of approximately 20%, and far-field patterns with divergences as low as 2° are demonstrated. All of these indicate the unique properties of a PCSEL can be achieved using epitaxial regrowth to create an all-semiconductor photonic crystal within the device. Polarisation occurs along one of the Γ-X directions as predicted from the modelling of magnetic field vectors in chapter 1. Divergences have no conclusive dependence on current, but further work is required to confirm if the source of the second peak in the $\theta = 90°$ orientation is due to asymmetric growth to or not.

The sub-threshold angularly-resolved EL spectra showed the photonic crystal is directly influencing the emission according to the modelled photonic band structure. Coupling coefficients of $\kappa_1 = 3920 \pm 140$ cm^{-1} and $\kappa_3 = 560 \pm 20$ cm^{-1} are measured directly from the peaks in the band structure. κ_3 is lower than expected from the waveguide modelling discussed in chapter 2, but is shown to be between the expected values for a two dimensional grating with different fill factors at the top and bottom of the grating layer. Further measurements of above threshold band structures should confirm whether the observed linewidth broadening is occuring from higher wavevector states, or whether additional bands are lasing at the Γ point.

External feedback provides no clear increase in raw power, but a significant increase in spectral intensity at certain output coupler reflectivities is observed. A small decrease in spectral threshold is also observed as feedback is increased. Such effects suggest two things; first, that κ_1 is sufficient to couple the reflected light back into the photonic crystal and thereby reduce the threshold gain and current; and second, that κ_3 is also increased by the feedback as there is a small increase in output power at certain reflectivities from the additional in-plane coupling.

However, if external feedback truly produces a significant effect on the emission of a PCSEL, the low power of devices tested here makes it difficult

to clearly observe the increase. Future work to include a DBR underneath the active region of the device would increase the power significantly. This would create a reduction of the initial 50% loss from the active out the bottom of the device, and introduce a vertical cavity around the photonic crystal that will enhance any feedback effects and thereby increase the output power. The resulting higher power devices will make it easier to ascertain the effect of introducing external feedback. Increasing device and aperture sizes would also aid in alignment to make the process of external feedback easier.

References

[1] "Band optimization of two-dimensional photonic crystal surface-emitting laser" W. Zhou, B. Jiang, W. Chen, A. Liu, Y. Wang, C. Ma, M. Xing and W. Zheng. J. Optics, **13**, 015104 (2011)

[2] "Large absolute and polarization-independent photonic band gaps for various lattice structures and rod shapes" N. Susa. J. Appl. Phys., **91**, No. 6, 3501 (2002)

[3] "Polarization mode control of two-dimensional photonic crystal laser by unit cell structure design" S. Noda, M. Yokoyama, M. Imada, A. Chutinan and M. Mochizuki. Science, **293**, 1123 (2001)

[4] "Photonic band-gap structures" E. Yablonovitch. J. Opt. Soc. Am. B, **10**, No. 2, 283 (1993)

[5] "Multidirectionally distributed feedback photonic crystal lasers" M. Imada, A. Chutinan, S. Noda and M. Mochizuki. Phys. Rev. B, **65**, 195306 (2002)

[6] "Finite-difference time-domain simulation of two-dimensional photonic crystal surface-emitting laser" M. Yokoyama and S. Noda. Opt. Express, **13**, No. 8, 2869 (2005)

[7] "Theory of light propagation in strongly modulated photonic crystals: Refractionlike behavior in the vicinity of the photonic band gap" M. Notomi. Phys. Rev. B, **62**, No. 16, 10697 (2000)

[8] "Experimental technique to determine the band structure of two-dimensional photonic lattices" V. N. Astratov, M. S. Skolnick, S. Brand, T. F. Krauss, O. Z. Karimov, R. M. Stevenson, D. M. Whittaker, I. Culshaw and R. M. De La Rue. IEE Proc. Optoelectron., **145**, No. 6, 398 (1998)

[9] "Lasing band edge identification for a surface-emitting photonic crystal laser" K. Sakai, E. Miyai, T. Sakaguchi, D. Ohnishi, T. Okano and S. Noda. J. Sel. Areas Commun., **23**, No. 7, 1335 (2005)

[10] "Coupled-wave model for square-lattice two-dimensional photonic crystal with transverse-electric-like mode" K. Sakai, E. Miyai and S. Noda. Appl. Phys. Lett., **89**, 021101 (2006)

[11] "Distributed feedback laser diodes and optical tunable filters" Wiley (2003) H. Ghafouri-Shiraz p.75

[12] "All-semiconductor photonic crystal surface emitting lasers based on epitaxial regrowth" R. J. E. Taylor, D. M. Williams, D. T. D. Childs, B. J.

Stevens, L. R. Shepherd, S. Khamas, K. M. Groom, R. A. Hogg, N. Ikeda and Y. Sugimoto. IEEE J. Sel. Topics Quant. Electron., **19**, No. 4, (2013)

[13] "Characterization of a distributed feedback laser with air/semiconductor gratings embedded by the wafer fusion technique" M. Imada, S. Noda, H. Kobayashi, and G. Sasaki. IEEE J. Sel. Top. Quantum Electron., **35**, No. 9, 1277 (1999)

[14] "Band structure and waveguide modelling of epitaxially regrown photonic crystal surface emitting lasers" R. J. E. Taylor, D. M. Williams, J. R. Orchard, D. T. D. Childs, S. Khamas and R. A. Hogg. J. Phys. D: Appl. Phys., **46**, 264005 (2013)

[15] "Design rules and characterisation of electrically pumped vertical external cavity surface emitting lasers" J. R. Orchard, D. T. D. Childs, L. C. Lin, B. J. Stevens, D. M. Williams, R. A. Hogg. Jap. J. Appl. Phys., **50** (4) 04DG0S (2011)

[16] "Trade-offs in the realisation of electrically pumped vertical external cavity surface emitting lasers" J. R. Orchard, D. T. D. Childs, L. C. Lin, B. J. Stevens, D. M. Williams, R. A. Hogg. J. Sel. Top. Quant. Electron., **17** (6) 1745 (2011)

[17] Various Layertec optical plane mirrors used. Specifications for some can be found at http://www.layertec.de/en/shop/articles?kanr=KA-001&senr=SE-011&tynr=TY-001

6 Summary and Future Work

In this thesis the successful design, fabrication and characterisation of an epitaxially regrown photonic crystal surface emitting laser has been described. Starting from the gaps in the knowledge outlined in section 1.4, a photonic crystal with the small refractive index contrast between two semiconductor materials was not known to be sufficient to create a partial band gap and achieve lasing.

Through optimisation of the waveguide design in chapter 2, the coupling between the active region and the photonic crystal is shown to be above the threshold limit for lasing to occur (as suggested in [1]). Surprisingly from the extent of research on PCSELs with voids in the literature, it was also shown that a void incorporating photonic crystal would have a significantly smaller mode overlap in such a structure.

Epitaxial regrowth of GaAs through MOVPE has been developed to prevent voids from forming within a photonic crystal layer and create a buried two-dimensional InGaP-GaAs grating. Attempts to generate large area patterns in a cheap and quick method for PCSELs (laser interference lithography) have so far proved unsuccessful.

The results outlined in chapters 4 and 5 have shown that an all-semiconductor photonic crystal can provide sufficient feedback for lasing to occur, and quan-

tified the strength of the photonic crystal coupling. Chapter 4 showed the detuning of the emission wavelength with temperature and demonstrated that low threshold PCSELs were obtained when the gain peak coincided with the wavelength that satisfied the Bragg condition. Laser oscillation is shown to be due to the photonic crystal through measurement of the band structure in chapter 5, and characteristics such as coupling strengths and beam divergences were shown to be comparable with other void based PCSELs.

The use of all-semiconductor photonic crystals and the epitaxial regrowth process described are shown to be suitable for generating 2D PCSELs. This regrowth process could also form the stepping stone to generating an easy fabrication technique for 3D photonic crystals designed for optical wavelengths.

6.1 Alternative materials in the photonic crystal

The work in this thesis has focussed on a photonic crystal consisting of InGaP and GaAs within an AlGaAs-GaAs waveguide for operation at $\lambda = 980$ nm. Waveguide modelling used these to determine if the coupling is sufficiently high to achieve lasing. Further investigation using alternative semiconductor alloys may yield a waveguide with a higher coupling strength. This possibility has not been considered in this thesis due to the current limitations of the epitaxial regrowth process relying on the specific semiconductors used.

For generating alternative emission wavelengths such as $\lambda = 850$ nm or $\lambda = 1.5$ μm, other semiconductor alloys are required. Whilst the period of the photonic crystal can be easily adjusted to achieve these wavelengths, other problems prevent emission. For example, any GaAs layers within a device targeting $\lambda = 850$ nm will absorb the light. Redesign of the waveguide is clearly required for alternative wavelengths, however, further waveguide modelling could inform on the optimum semiconductor materials to achieve high coupling between the active and photonic crystal in these structures.

Chapter 2 showed that a void incorporating photonic crystal layer had a lower coupling than an all-semiconductor one, however, further modelling may yield a solution that benefits the voids rather than all-semiconductor. For example, a ballast layer of similar refractive index could be inserted beneath the active region and this would form two regions of low refractive index within the waveguide that are symmetrical around the active. This could prevent the mode distortion by the low refractive index of any waveguide layer containing voids. The effects of varying the aluminium composition of the upper AlGaAs cladding layer should also be investigated thoroughly to ensure the waveguide is optimal. In order to ensure the mode has decent overlaps with the quantum wells and photonic crystal this may require the addition of ballast layers as well.

6.2 Device improvement

The low efficiency of the devices reported in this thesis is not ideal, with significant further work required to optimise device processing. Further tests on contact materials and annealing processes should improve the electrical characteristics such as VI curves. Combining this with improvements in device isolation through mesa etch optimisation should help limit non-radiative recombination losses within the device. More work on the photonic crystal etch process to improve the verticality of the sidewall profile is required and this could help decrease the scattering loss by the grating in directions other than the normal.

The devices reported in this thesis have a relatively low output power as at least half of the laser emission is lost out the bottom. The detected output power being the component that is diffracted in the vertical direction out of the device. It is equally as likely that this light is diffracted out the bottom of the photonic crystal. By introducing a high reflectivity mirror at the start of the initial growth, for example a distributed Bragg reflector (DBR), any light escaping in this fashion should be reintroduced to the photonic crystal or reflected straight up and out of the device.

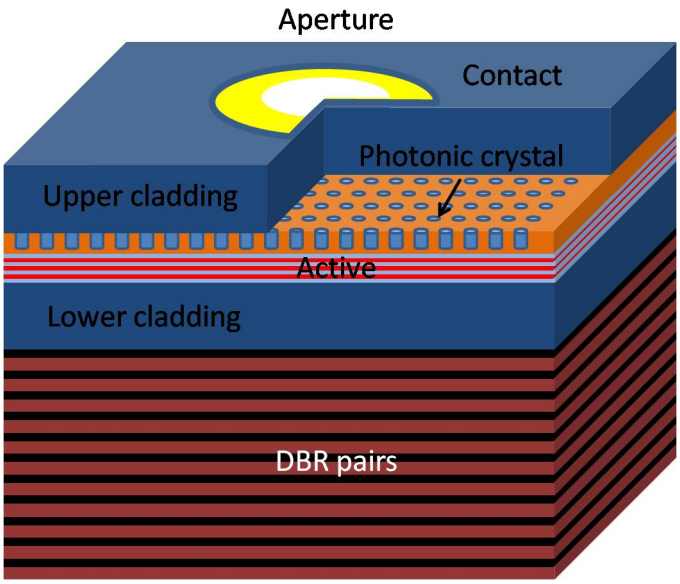

Figure 6.1: Schematic of a possible PCSEL structure with distributed Bragg reflector (DBR) pairs beneath the active region.

Figure 6.1 is a schematic showing the introduction of a set of DBR pairs underneath the structure reported in this thesis. Whilst this will reduce emission loss from the lower side of the device, it will also introduce the possibility of new external feedback effects as the structure starts to resemble a VECSEL with a photonic crystal layer included. Other devices which incorporate DBR mirrors, for example VECSELs, typically use AlGaAs/GaAs DBR pairs to target $\lambda = 980$ nm [2, 3].

6.3 Additional characterisation possibilities

Further characterisation of these all-semiconductor PCSELs should include investigations to determine if the perturbations in the surface of the regrown GaAs layer are the cause of the asymmetry in the far field patterns. This will require taking TEM images from along different semiconductor crystal directions and should also include additional fabrication runs with the photonic crystal patterned misaligned with the semiconductor crystal directions.

Measurements of band structures above threshold should confirm whether linewidth broadening is occuring from higher wavevector states being accessed, or whether additional bands are lasing at the Γ point. If this broadening is due to additional bands lasing then characterisation of the emission polarisation should confirm which.

One of the most significant characteristics of PCSELs is their potential to scale the output power with the device area as lasing occurs from the band edges. Whilst this has been reported for void based PCSELs it should be confirmed that this is also a feature of all-semiconductor PCSELs. This will require additional fabrication runs to create devices of varying diameter sizes.

References

[1] "Room temperature continuous wave operation of a surface emitting two dimensional photonic crystal laser" D. Ohnishi, T. Okano, M. Imada and S. Noda. Optics Express, **12**, No. 8, 1562 (2004)

[2] "Trade-offs in the realisation of electrically pumped vertical external cavity surface emitting lasers" J. R. Orchard, D. T. D. Childs, L. C. Lin, B. J. Stevens, D. M. Williams, R. A. Hogg. J. Sel. Top. Quant. Electron., **17** (6) 1745 (2011)

[3] "Design rules and characterisation of electrically pumped vertical external cavity surface emitting lasers" J. R. Orchard, D. T. D. Childs, L. C. Lin, B. J. Stevens, D. M. Williams, R. A. Hogg. Jap. J. Appl. Phys., **50** (4) 04DG0S (2011)